CIRCULATION INSIDE THE NARROWS OF ST. JOHN'S HARBOR

MING GUO

Circulation Inside the Narrows of St. John's Harbor

by

© Ming Guo
B.Sc. (1999) Ocean University of Qingdao

A thesis submitted to the
School of Graduate Studies
in partial fulfillment of the
requirements for the degree of
Master of Science.

Department of Physics and Physical Oceanography
Memorial University of Newfoundland

April 22, 2005

ST. JOHN'S NEWFOUNDLAND

Contents

Abstract

St. John's harbor is located on the Northeast coast of the Avalon Peninsula on the Island of Newfoundland. During the summer and fall of 1999 and 2000, two continuous observational program were carried out in order to determine the circulation in the Narrows of the harbor and the influence of external forcing from Avalon Channel. Observational current data in both years show that the axial current in the Narrows has a two-layer vertical structure. A strong seasonal bottom outflow was found in the center of the Narrows in both years, and it keeps strongest in August and September. Empirical Orthogonal Function (EOF) analysis applied to the axial subtidal currents in 2000 shows that mode 1 contains over 40% of the total variance and mode 2 contains 27% of the total variance. Coherence analysis result indicates that mode 1 represents the influence from local wind stress and mode 2 represents the effect from external force outside the harobor. Comparison between observation current and wind speed shows that wind force has a direct influence on the surface current and a counter influence on the current in the lower layer. The result of a two-layer barotropical model driven by wind forcing shows a high correlation with EOF mode 1. The counter effect of wind force on the lower layer also occurs in the model, and can be explained as the conservation of the volume in the harbor.

Acknowledgements

I would like to thank Dr. Brad deYoung for guiding me through a stimulating and rewarding degree program, providing me with a challenging research project, and instilling in me a valuable sense of intellectual independence. Dr. deYoung and the School of Graduate Studies also provided me with financial support without which this degree would not have been possible. A number of people in the Department of Physics and Physical Oceanography in Memorial University made helpful contributions: Dr. Entcho Demirov and Daniel Bourgault provided assistance during the setup of the physical model. Also, thanks to Chris Stevenson for the continuous computer support and assistance.

I would like to thank my wife, Zhiying, for accompanying me through this process, supporting me and helping me. My family, mother and father, have always helped me in whatever I am doing, and kept me going in the right direction.

List of Tables

List of Figures

Chapter 1

Introduction

1.1 Research Location: St. John's Harbor

St. John's harbor is located on the Northeast coast of the Avalon Peninsula on the Island of Newfoundland (Figure 1.1). The harbor's mouth opens to the east, has a large sill and narrow entry to a shallow protected bay that has a somewhat deeper basin in the northeastern half of the harbor. The mean depth of the harbor is about 12-15 m, the sill depth is 13 m and the width of the harbor mouth is approximately 180 m. The deepest point of the harbor is about 33 m and the deepest in the Narrows is about 28 m. The length of the harbor is approximately 1200 m and the channel of the narrow is about 800 m long. The mean width of the Narrows is about 280 m. The harbor has a surface area of approximately 1.2 million square meters (deYoung *et al.*, 2000). To the north of the harbor lies Conception Bay (deYoung and Sanderson, 1995), and Avalon Channel (Anderson and Petrie, 1983) sits outside of the harbor. Outside the mouth of the harbor, the water depth of the ocean increases from about 30 m to more than 100 m sharply (Figure 1.2). Figure 1.1 and 1.2 show the position of the harbor, and the bottom topography of the study area.

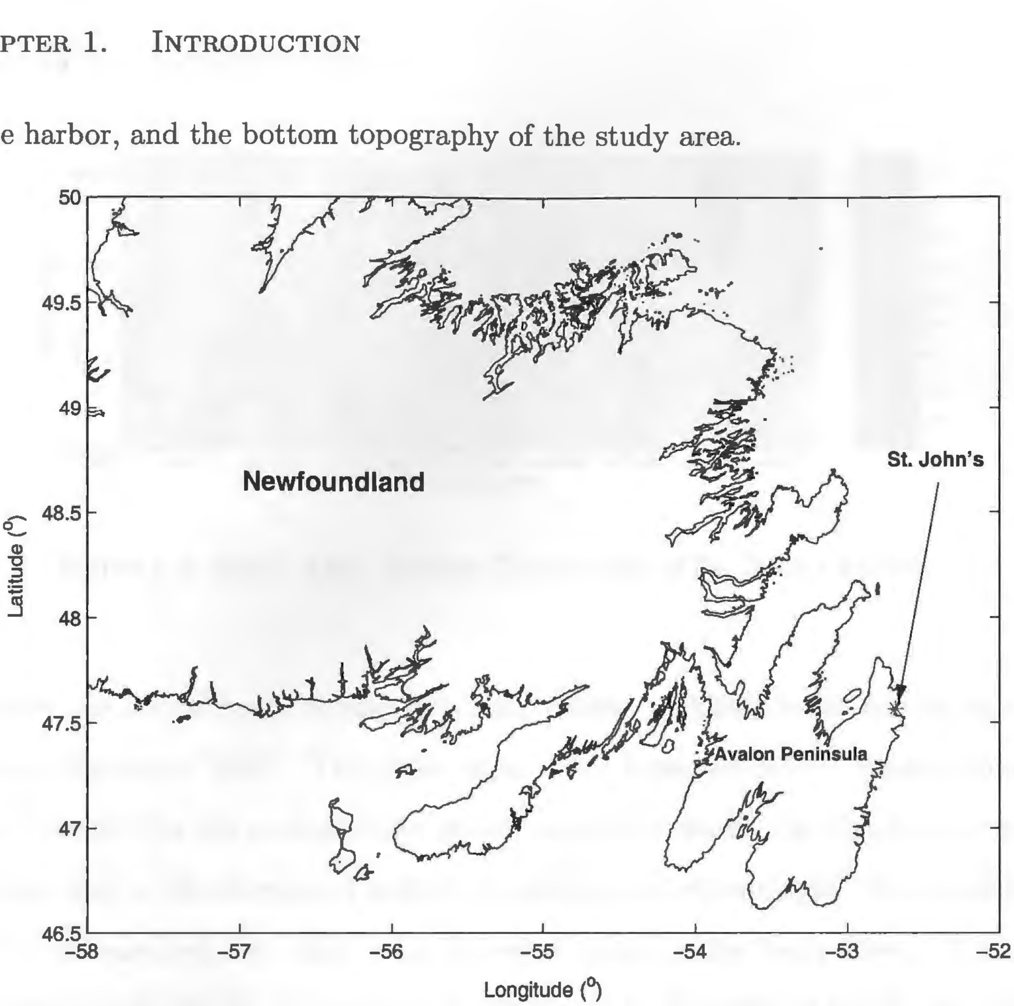

Figure 1.1: Position of St. John's harbor

1.2 Current in Connecting Channel

Estuarine channels are interesting to oceanographers, not only because of their importance as sea-routes but also because these channels connect the ecosystem of the bay that the channel connected to the oceans. One advantage to study of these systems is that comprehensive scale observation of these areas are comparatively easy. A general circulation system in an estuary channels can be modelled as a two-layer

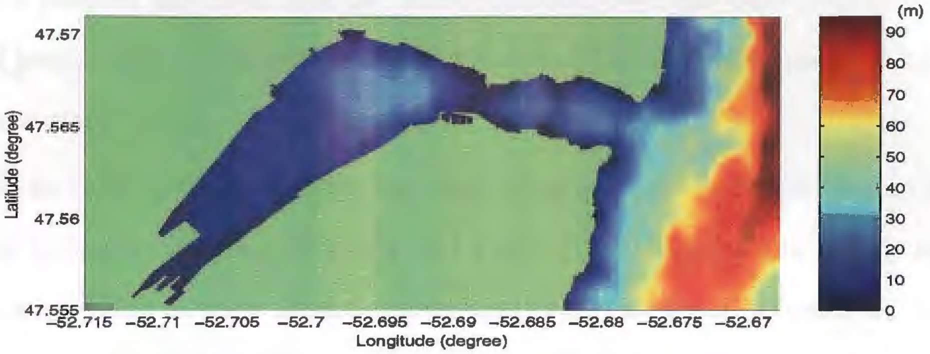

Figure 1.2: Study Area: Bottom Topography of St. John's harbor.

flow with the surface water flowing out of the estuary and deep water flowing into the estuary (Matsuura, 1997). The upper layer water flows out from a estuary channel due to run-off. As the surface water flows toward the mouth, the volume of outflow increases due to the increase of salinity by mixing and entrainment. To compensate for this increase volume, there is an inflow of water in the lower layer. Also, the circulation of an estuary channel can be influenced by a variety of forces over a wide range of timescales, from tides to wind and current outside the channel.

Generally, tides play an important role in the coastal ocean area. As the tide propagates, entering water with a decreasing depth, the tidal amplitude, both in elevation and current grows, and also the interference between different tidal components becomes more significant which leads to the generation of shallow water tidal constituents. Tides often grow in importance in a harbor channel and can play an important role in mixing water, breaking down the stratification, and generating mean flow. Since the external Rossby radius is much larger than typical channel width, the barotropic tidal propagation in a narrow channel can often be treated as a plane wave (Stigebrandt,1999), which means most energy of the tides focus on the component of the along channel direction. For St. John's harbor, even the baroclinic tide, with an internal length scale of roughly 1-5 km for the first internal wave, can also be treated as a plane wave.

Also, as tides propagate along an ocean channel, energy is lost due to the friction and turbulent mixing. deYoung and Pond (1988) studied the energy loss from the barotropic tide in three British Columbia fjords, and found internal tides were an important sink for tidal energy, while in fjords with shallow (15-20 m) sills friction appeared to be the dominate sink for energy. Stigebrandt (1999) identified three processes by which energy may be lost from oscillatory barotropic tide flow in constricted straits; (1) friction against the bottom boundary, by which momentum of the mean flow is lost to turbulent dissipation in the bottom boundary layer (which may occupy the whole water column in some circumstances), (2) baroclinic wave drag, where the generation of a freely propagating internal wave, at the same frequency as the oscillation of the barotropic flow, extracts energy from the borotropic flow, (3) barotropic form drag, where changes in the cross-sectional area of the constriction may lead to eddy shedding from the mean flow, and/or separation of the tidal flow from the bottom boundary. His study also showed that roughly 16% of the total incident tidal energy is lost from the barotropic tide. Inall (2004) studied Loch Etive fjord, Scotland, and the ratio between loss to bottom friction, barotropic form drag and baroclinic wave drag is estimated to be 1:4:1(1:4:3.3) at springs(neaps).

Tides can also influence the water mixing and exchange process in a channel. Geyer and Cannon (1982) found that observations of the gravitational circulation over the sill at the entrance to Puget Sound (Washington, U.S.A) indicated a fortnightly modulation of the two-layer flow with a corresponding variation in stratification. Gravitational circulation and stratification reach a maximum during neap tides and minimum during spring tides. The modulation appears to be regulated by turbulence generating by tidal flow over the sill, which varies as a function of tidal amplitude. Farmer and Freeland (1983) pointed out that the exchange process of the deep water in the sill area of a channel was generally unsteady and the rate of the exchange can be modulated by many factors, such as the tides, fresh water run-off and the mixing process. deYoung and Pond's (1988) study of Indian Arm, British Columbia coast, shows that once high density water is available at the entrance to the system, the timing of the exchange of deep water is controlled by the spring/neap tidal cycle. During neap tides, when reduced energy for mixing is available, the water reaching the sill attains a maximum in density, while spring tides reduce the density of the water reaching the sill because of the increased energy available for mixing.

As mentioned above, estuary channels respond to a variety of forcing mechanisms over a wide range of timescales. Even though the short-period semi diurnal or diurnal tidal motions are often the most energetic mechanisms operating in estuaries, the long-period subtidal motions are extremely important because they ultimately control the long-term transport and distribution of suspended and dissolved matters in the estuaries. Carmack (1998), working in Markenzie Canyon in Beaufort Sea, showed that period and episodic events dominated the flow field and suggested that temporal variability be considered in three frequency bands: high frequency(> 0.7 cpd (circle per day)) tidal and inertial motions; intermediate frequency ($0.07 - 0.7$ cpd) mesoscale and baroclinic eddy motions; and low-frequency (< 0.07 cpd)(subtidal frequency) upwelling and topographic wave motions. Approximately 65% of the kinetic energy was found in the low-frequency band and that such fluctuations were especially well developed during the late summer and autumn periods of strong winds and minimum ice cover. Low-frequency current variability was significantly correlated to the cumulative effect of easterly wind forcing. Among aspects of the subtidal motion, the density-induced gravitational circlation was the first to attract extensive research [Pritchard 1952,1956; Hansen and Rattray 1965].

Many factors can influence the sub-tidal current in an ocean channel, such as wind and current outside the mouth of the channel. The significance of wind forcing on the subtidal variability in estuaries was recognized some two decades ago when a series of studies conducted by different investigators in several estuaries showed the importance of wind-induced motion to estuarine processes at subtidal frequencies. Wersberg and Sturges (1976) and Weisberg (1976) found the subtidal circulation in the Providence River and west passage of Narragansett Bay to be dominated by wind-induced fluctuations. In a number of studies related to the Chesapeake Bay and some of its tributary estuaries, Wang and Elliott (1978) and Wang (1979) showed that the dominant subtidal sea level fluctuations in the Chesapeake Bay are the result of upbay propagation of coastal sea level fluctuations generated by alongshore winds. They also found the existence of largely barotropic volume exchange in the lower bay as part of the response of the coupled bay-shelf system to atmospheric forcing. The importance of atmospheric forcing on low-frequency estuarine variability has also been demonstrated by Smith (1977,1978) in Corpus Christi Bay, Tesas, and Kjerfve (1978) in North Inlet, South Carolina. Buckley and Pond's (1976) study showed that with continuous up-fjord wind, the surface current was reversed initially, but it reversed again after a certain time as if the wind stopped. Their explanation was that at the second reversing, a balance between wind stress and pressure gradient was achieved. Svenden and Thompson (1978) made observations of currents in Norwegian showed that the first response to wind occurs at the surface but the second response was at a somewhat greater depth (60 m) below the pycnocline (10 m), and the response gradually propagated upward through the water column.

In addition to these earlier works, many studies were conducted in the past two decades to examine the nature and characteristics of the wind-induced subtidal variability in variety of estuaries, ranging from partially mixed estuaries such as the San Francisco Bay (Walters 1982,1985) and Delaware Bay (Wong and Carvine 1984) to wide and shallow but highly stratified estuaries such as the Mobile Bay (Schroeder and Wiseman 1986; Wiseman 1988). Furthermore, wind forcing has also been shown to be very important to the subtidal variability in coastal lagoons with restricted communication with the ocean (Wong and Wilson 1984; Wong and Dilorenzo 1988; Kjerfve and Knopper 1991; Janzen 1996). Studies in Puget Sound also noted that wind has a significant influence on sub-tidal circulation in the channel (Cannon, 1983; Bretschneider *et al.*, 1985;Matsuura, 1997). Bretschneider *et al.* (1985) used Empirical Orthogonal function (EOF) analysis to point out that wind effects were dominant mode and had strong influence at the surface and weak counter influence at mid-depths on the along-channel currents. The result showed that at subtidal time scales three layers existed in the fjord profile, a near-surface wind-driven shear; the second, a near bottom layer dominated by density currents that propagate up the estuary after generation during neap tidal mixing at the entrance to Puget Sound, and an intermediate layer influenced by partial refluxing of an inflow passage water and modulated at fortnightly periods by nonlinear mixed tides. The first EOF mode is highly correlated with the local winds, with the maximum correlation (r=0.73) occurring when currents lagged winds by less than 6 hours. Matsuura and Cannon (1997), showed that wind affects currents at both surface layer and the mid-depth layer at which the wind effects have opposite directions to the surface response, while when stratification is weak, direct responses of the current to the wind can propagate much deeper. The acceleration of the current indicates that the response of currents to wind events are almost instantaneous, which suggests that the time lag between wind and current is simply caused by the fact that the currents lag behind the accelerations.

Numerical model results have also demonstrated the influence of the wind on the subtidal current. Farmer (Farmer, 1976; Farmer and Osborn, 1976) studied the wind effects in Alberni Inlet (British Columbia, Canada), a highly stratified fjord with a thin surface layer. He used a two-layer model and compared it with actual data for the displacement of the pycnocline. This study suggested that the low frequency current in both layers in the model demonstrated great dependence on the wind, and the influence of the wind was with opposite direction on each layer.

Results from the above mentioned studies reveal that the subtidal variability in estuaries may be induced by winds through a combination of remote and local effects. For the remote effect, winds on the continental shelf adjacent to particular estuary may produce coastal sea level set up or set down at the mouth of the estuary. Furthermore, the effect of remote wind on the continental shelf far away from the estuary in question may produce coastal disturbances which propagate into the coastal areas adjacent to the estuary as free waves (Noble and Butman 1979; Wang 1979). Regardless of the source of the coastal set up or set down, the remote wind effect can produce subtidal variability in the estuary by the impingement of the coastal sea level fluctuations at the mouth of the estuary. On the other hand, the local wind effect is more straightforward, as it represents the effect of local wind stress acting on the surface of the estuary.

The question of whether the remote or the local wind effect should be the dominant mechanism responsible for producing the subtidal variability in estuaries is a long-standing problem. Many studies suggest that the solution may be depending on the particular characteristics of the estuary involved. Garvine (1985), however used an analytical model based on scaling arguments to show that the length of the estuaries relative to the subtidal estuarine wavelength should determine the dominance of the remote effect for both sea level and sectionally averaged current fluctuations in the estuaries.

Bottom topography can also influence the wind-driven circulation in an estuarine channel. Hearn (1987) pointed out that wind-driven circulation in a shallow bay or harbor could be greatly influenced by bottom bathymetry. Some studies in Puget Sound also showed that bottom topography could greatly affect the wind influence to the current in a fjord. Bretschneider and Cannon (1985), showed that topographic effects force most of the seaward compensating flow through an adjacent channel, creating a clockwise circulation around an intervening island in the fjord. Geyer *et al.* (2000) demonstrated that subtidal motions can be modeled without detailed knowledge of the effective eddy viscosity, only requiring an estimate of the bottom drag coefficient, the tidal forcing conditions, and the baroclinic presuure gradient. Topography can also influence the current indirectly by forcing on the wave propagating in the channel. In the absence of waves, topographic variations primarily control the circulation driven by surface wind stress. High flow velocities with strong vertical shear are generated down-wind in the shallower region, whereas the return flow in the deeper water shows lower velocities with reduced vertical shear. In the presence of waves, wave-current interaction has a less important effect on set-up, as there is a tendency for wave effects to cause greater reduction of the bottom currents in shallower water and weaken reduction of currents in deeper water. The magnitude of wind-driver currents in shallow bodies of water is significantly influenced by wave-current interaction (Signell, 1995).

1.3 Research Background in St. John's Harbor

In St. John's harbor (Figure 1.1) the water depth in the Narrows is very shallow, with the deepest point of 28 m, compared with the deep ocean outside the harbor, with the deepest point in the Narrows to be 3-4 times shallower than the depth of Avalon channel outside, so when the flow enters the channel it will be strongly accelerated by this depth difference which can generate some strong jet in the channel, and also this feature makes some shallow water tidal signals very important when doing tidal analysis (deYoung *et al.*, 2000). Preliminary analysis of observations shows that sub-tidal (about 0.5 cpd) energy is significant in the current inside the Narrows (deYoung *et al.*, 2000). Spectral analysis of the current data demonstrates that most energy of the flow in the Narrows focus on the low frequency time scale. Therefore, study the forcing mechanism of this sub-tidal signal is important to explain the circulation in the Narrows. Strong wind is another important feature in this area, with the annual average wind speed above 20 km/h in St. John's city (/www.climate.weatheroffice.ec.gc.ca/climate-normals), so the wind stress can greatly influence the up-layer flow in the Narrows. Furthermore, the local strong wind stress can generate low frequency internal wave in area nearby outside the harbor, which will also affect the circulation in the Narrows when propagating passing the open mouth of the harbor in the east. Therefore, this location also becomes an interesting area to study whether the remote or the local wind effect should be the dominant mechanism for the transport in the channel.

1.4 Research Objectives

The objectives of this thesis are as follows:

- To obtain a clear understanding of the current in the Narrows of the harbor, including the tidal current, subtidal current and the transport.
- To determine the coherence relationship between the current inside and outside the Narrows.
- To determine the forcing terms that regulate the currents, in particular at subtidal frequencies, in the Narrows.

Surprisingly, the circulation in St. John's harbor has never been studied (in published articles) except the two data reports for the observation programs in 1999 and 2000 (deYoung *et al.*, 2000). In this thesis, the first historical measurements and description of the circulation through the Narrows of the Harbor will be presented. With better understanding of the Narrows in the harbor, it is intended that this project will also provide information to aid in designing sewage treatment for the harbor.

1.5 Outline

Following this introductory chapter, Chapter 2 will outline the data to be used in this thesis and provide basic descriptions of the data. In Chapter 3, the methods applied for the data analysis and the result of the analysis will be discussed (Tidal analysis and EOF result). In Chapter 4, a description of a two-layer model will be presented, and comparison between the model result and the observation result is discussed. Then, a brief summary and discussion on the result of this thesis are given in Chapter 5. A complete list of references is presented in Bibliography.

Chapter 2

Observation Program and Data Information

2.1 Observation Program of St. John's Harbor in 1999 and 2000

In order to determine the circulation over the sill and the implications of the transport for the exchange of water into and out of the harbor, during the summer and fall of 1999 an upward-looking Acoustic Doppler Current Profiler(ADCP)was deployed in the center of the harbor mouth at a depth of 17m. In July/August, an additional cross-channel-looking ADCP was deployed on the southern side of the harbor mouth at a depth of 5m, pointed across the channel toward Chain Rock (Figure 2.1).

At the end of July, 2000, three upward-looking Acoustic Doppler Current Profilers(ADCP) and two S4 current meters were deployed in the Narrows. In addition, one ADCP, one S4 and one RCM current meter were deployed outside the harbor mouth, along with thirteen Vemco thermistors (Figures 2.1-2.3. The primary goal was to determine the circulation over the sill and the influence of external forcing, from the Avalon Channel, on the transport into, and out of, the Narrows. Temperature sensors were located on each of instruments.

2.2 Mooring Station Information

Figure 2.1 shows the location of the moorings in this two year observational program. The channel to the ocean of St. John's harbor is very narrow, measuring less than 200m across, so in 1999, a single mooring is deployed in the center of the channel at the mouth of the harbor for two periods, from July 24th to August 27th and from October 12th to November 9th. We expected this mooring to provide reasonable measurements of the average along channel velocity. Given the channel geometry, it was expected that most of the flow would be directed along the axis of the channel. The additional ADCP deployed in August, 1999 in side-looking mode was located on the southern side of the channel, pointed across the channel toward Chain Rock. The data of the two beams of this instrument is analyzed separately. The inward facing (facing the Harbor) beam shows similar result as the upward looking ADCP, while the outward facing beam does not show any clear velocity pattern and the spectral energy between 90 and 100 m even declines at almost all frequencies due to the sidelobe interference (de Young *et al.*, 2000). These data are not used in this thesis. Temperature sensors were located on both ADCP's and a fluorometer was deployed on the ADCP in the center of the channel (see Table 2.1 for details).

In Figure 2.1, the red star points are the locations of the moorings inside the Narrow in 2000. Figure 2.2 shows the bottom positions of N1-N5, and Figure 2.3 shows the

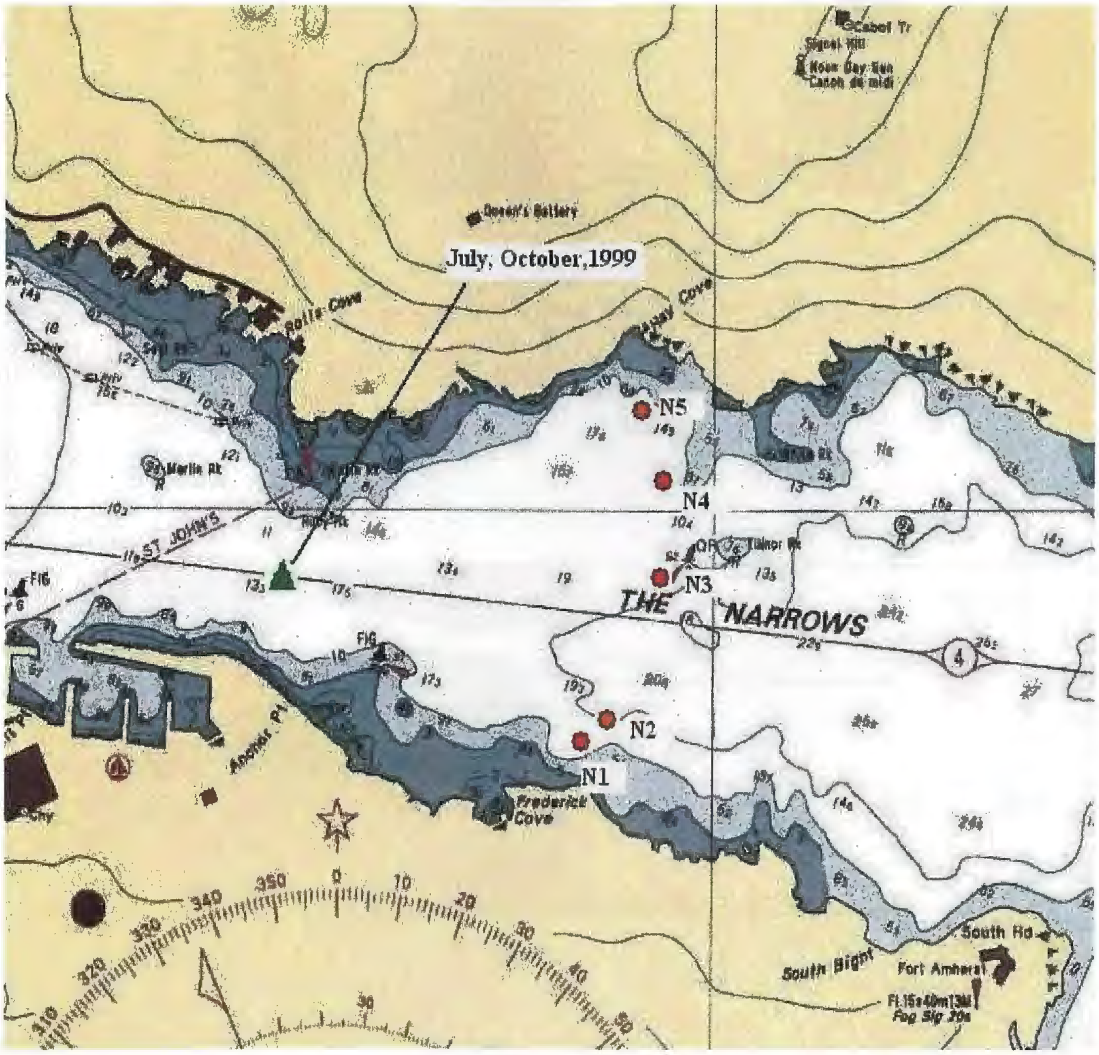

Figure 2.1: Mooring position inside the harbor. The green triangle is the uplooking ADCP mooring in 1999, and the red ones are the moorings in 2000, N1-N5 from bottom to top in turn

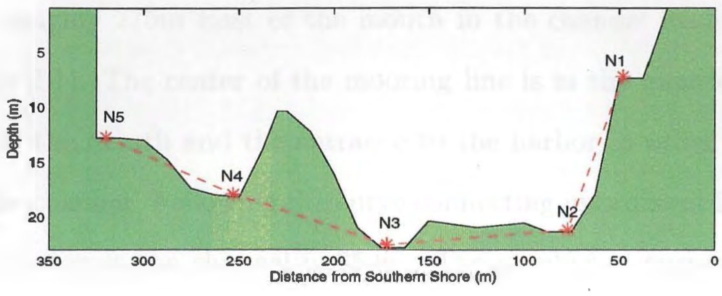

Figure 2.2: Mooring positions at the bottom of the Narrows. The prospective is looking out of the Narrows, with south to the right.

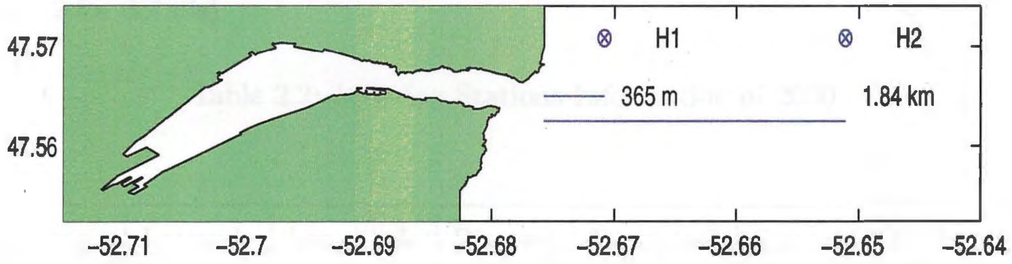

Figure 2.3: Mooring positions outside the harbor in 2000.

Table 2.1: Mooring Station Information of 1999

Mooring	Latitude	Longitude	Bin (m)	Depth(m)	Start(M/D)	Stop(M/D)
J1	47 33.97	52 41.29	1	17	7/24	8/27
O1	47 33.97	52 41.29	1	18	10/12	11/9

locations of the two moorings outside the harbor. The moorings inside the harbor were deployed roughly 275m East of the mouth in the channel leading to the North Atlantic (Figure 2.1). The center of the mooring line is in the middle of the channel, halfway between the mouth and the entrance to the harbor in order to minimize the end-effects of the channel. Following the curve connecting instrument locations (Figure 2.1), the distance across the channel is 350m. The number of current measurements was meant to adequentely sample the region, in order to resolve the tidal flow through the Narrows, which was hypothesized by deYoung *et al.*(2000). In addition, one ADCP, one S4 and one RCM current meter were deployed outside the harbor mouth, along with thirteen Vemco Thermistors in order to determine the influence of the external forcing, from the Avalon Channel, on the transport into and out of the Narrows (see Table 2.2 for details).

Table 2.2: Mooring Stations Information of 2000

Mooring	Latitude	Longitude	Bin (m)	Depth(m)	Start(M/D)	Stop(M/D)
N1(S4)	47 33.9	-52 41.1	N/A	7.2	7/24	9/19
N2(ADCP)	47 33.9	-52 41.1	1	21.2	7/22	9/19
N3(ADCP)	47 33.9	-52 41.0	1	22.5	7/22	9/18
N4(ADCP)	47 34.0	-52 41.0	1	17.9	7/23	9/18
N5(S4)	47 34.0	-52 41.0	N/A	12.7	7/23	9/20
H1(S4)	47 34.15	-52 39.75	N/A	22	7/25	9/24
H1(RCM)	47 34.15	-52 39.75	4	77	7/26	9/25
H2(ADCP)	47 34.15	-52 38.64	N/A	109	7/27	9/24

2.3 Observation Data Information

The current data of each mooring was first clipped to make sure the data of each depth has the same length, and then isolated of bad data points were eliminated using a simple linear interpolation scheme. The along-channel and cross-channel axis is determined through a covariance analysis (Emery, 1998). The angle of the channel-axis to the earth-axis, θ, can be calculated using the two velocity components as,

$$tan(2\theta) = \frac{\overline{2uv}}{\overline{u^2} - \overline{v^2}} \tag{2.1}$$

In Figure 2.4, the preferred value of θ is about 30^o, but its dependence on both depth and location (changing from 25^o to 40^o with different depth and location) prevent a single best angel of rotation to be determined by trial or error. Therefore, a rotation angle of 10 degrees was used here and was determined from the line connecting the planned locations of the instruments. For the data of 1999, the average orientation was 15^o clockwise rotation in July/August and 22^o clockwise rotation in October. The

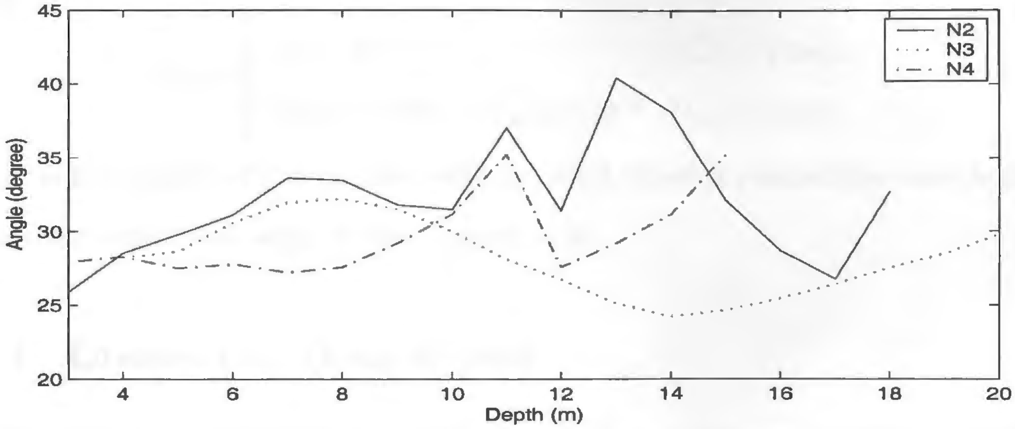

Figure 2.4: Angle determined by the covariance analysis to change to the along-channel axes of observation data in 2000.

mean velocity of the along channel and cross channel direction at each depth during each continuous observation period is computed as the arithmetic mean,

$$\overline{u} = \frac{1}{n}\sum_{i=1}^{n}(u_i) \tag{2.2}$$

Wind speed data used in this thesis for the same period as the mooring observation is from St. John's Airport. The wind stress is computed using the method of Large and Pond (1981) as following,

$$\tau = \rho_a C_D |\vec{U_w}| \vec{U_w}, \tag{2.3}$$

where

$$C_D = \begin{cases} 1.2 \times 10^{-3} & |\vec{U_w}| < 11m/s \\ (0.49 + 0.065 \times |\vec{U_w}|) \times 10^{-3} & \vec{U_w}| \geq 11m/s \end{cases}$$

and ρ_a is the density of the air. Accordingly, wind stress is rotated the same angle as the current velocity to adapt to the channel axis.

2.3.1 Observation Data of 1999

Mooring data in 1999 are tabulated with statistics on the mean, standard deviation, maximum and minimum in each velocity component at each depth (Appendix A). During July/August, 1999, the largest amplitude of the mean inflow velocity appears in the middle layer between 5m and 10m which is about 4 cm/s (Figure 2.5) and the largest amplitude of the mean outflow velocity appears in the bottom layer of more than 5 cm/s. The mean currents show that the mean cross-channel current is only 0.5 cm/s, as expected very small, but there is significant depth dependence to the mean along-channel currents (Figure 2.5). There is a mean outward surface current near the surface, probably forced by the fresh water inflow from the Waterford River and sewage dumping (deYoung, 2000). An interesting feature is that outflow exists not only in surface layer but also in bottom layer. The mean outflow in the bottom layer reaches 5.69 cm/s at 14m depth (Figure 2.5) which is a little strong compared with the inflow in the middle layer. To study the time-change of the vertical structure of the along-channel current, 3-day averaged velocity profile is calculated (Figure 2.6). In Figure 2.6 a, a three-layer structure exists during the whole period from July to August, with the surface layer and bottom layer dominated by outflow and the middle layer dominated by inflow. In Figure 2.6, we can also see that the dapth of the three layers does not keep stable but changes with time.

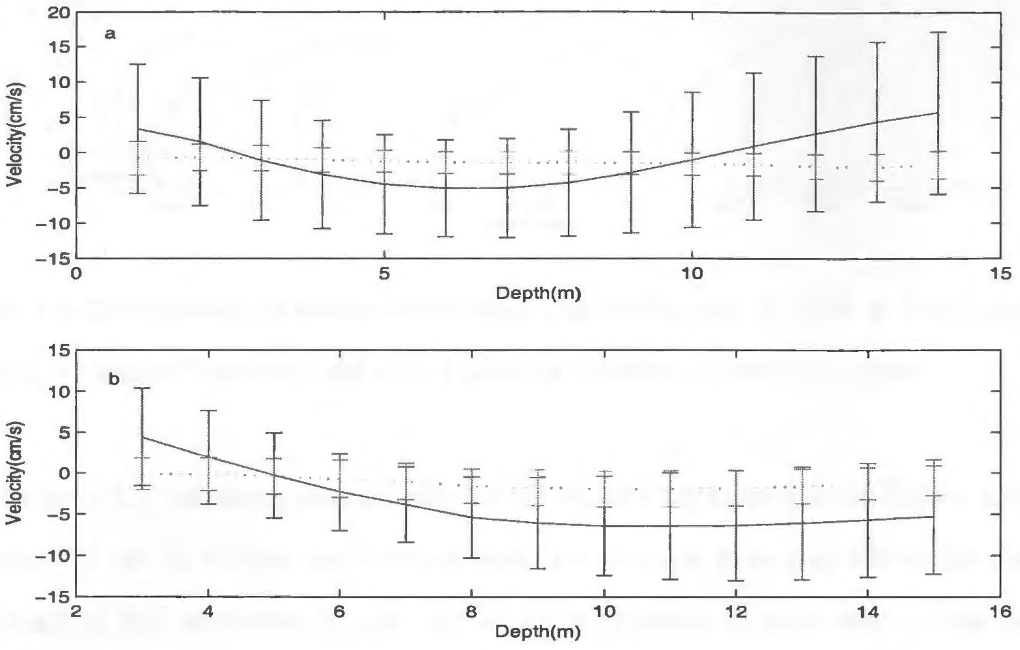

Figure 2.5: The mean along(solid line) and cross(dashed line) channel velocity profiles, the top one is of July-August and the bottom is of October,1999. The error bars are one standard deviation in length. (+) denotes outflow, (-) denotes inflow.

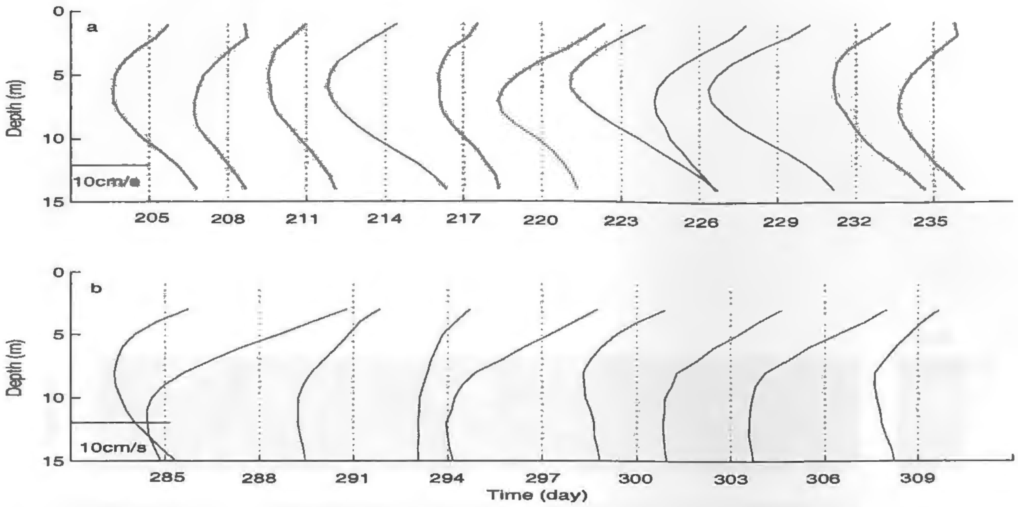

Figure 2.6: 3-day averaged profile of the along channel current in 1999. a: July/August Data, b: October/November data. (+) denotes outflow, (-) denotes inflow.

In Figure 2.7, the along channel velocity shows (the top figure) an oscillation feature of about 0.5 cpd in surface and bottom layer, for example from day 220 to 225, while the phase of the oscillation in the two layers is opposite to each other. The along channel wind stress keeps stable without strong peak during this period (Figure 2.7 b). The correlation coefficient between surface along channel current and wind stress in July/August is only 0.36, which means no apparent correlationship exists. However, the correlation coefficient between bottom temperature and bottom flow reaches 0.64, which means the correlation of the two variables is high, and in Figure 2.7 c and d, the temperature and bottom velocity trough coheres each other in three periods, from day 209 to day 210, from day 222 to day 223, and from day 228 to 229, the temperature decreasing with inflow and increasing with outflow as water outside the harbor is colder compared with the water inside. In Figure 2.8, the along channel current shows a significant oscillation feature that is highly correlated with that of the wind stress with

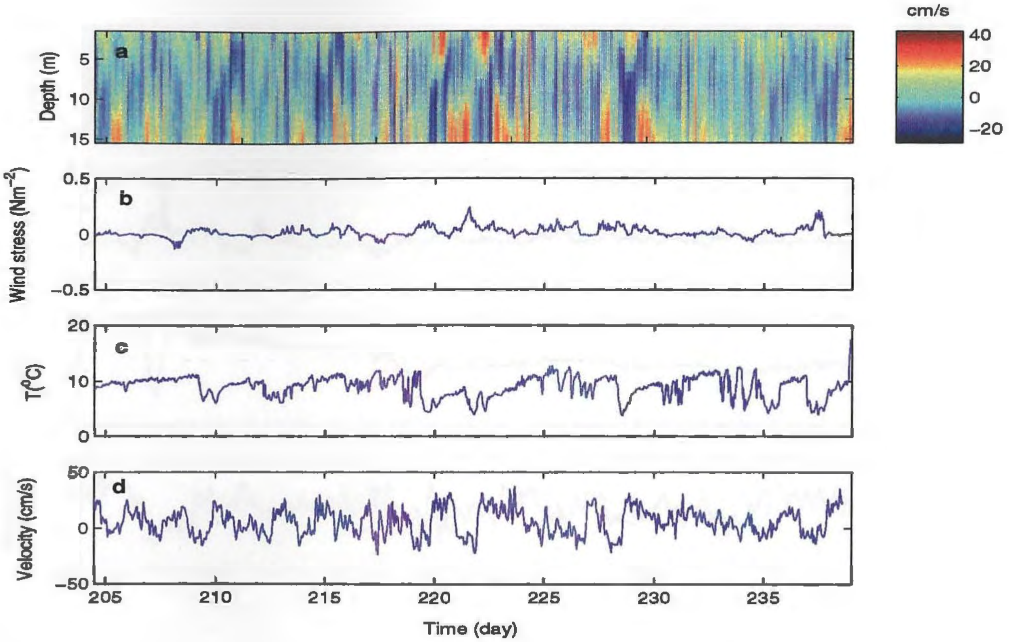

Figure 2.7: Time series data in July-August, 1999, from top to bottom: velocity along the channel, along channel wind stress, bottom temperature and bottom along channel velocity. (+) denotes outflow, (-) denotes inflow.

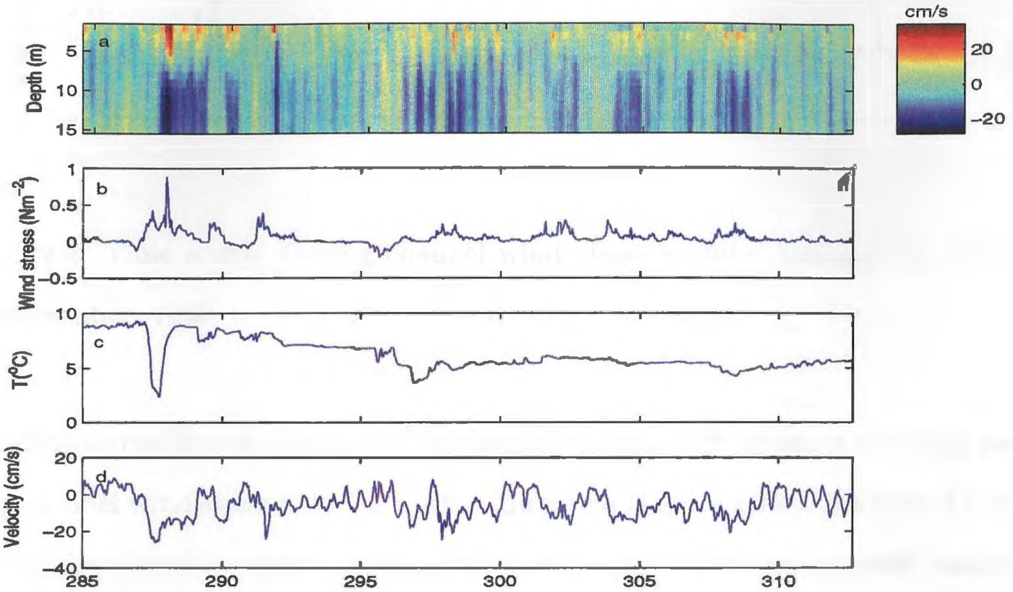

Figure 2.8: Time series data in October, 1999, from top to bottom: velocity along the channel, along channel wind stress, bottom temperature and bottom along channel velocity. (+) denotes outflow, (-) denotes inflow.

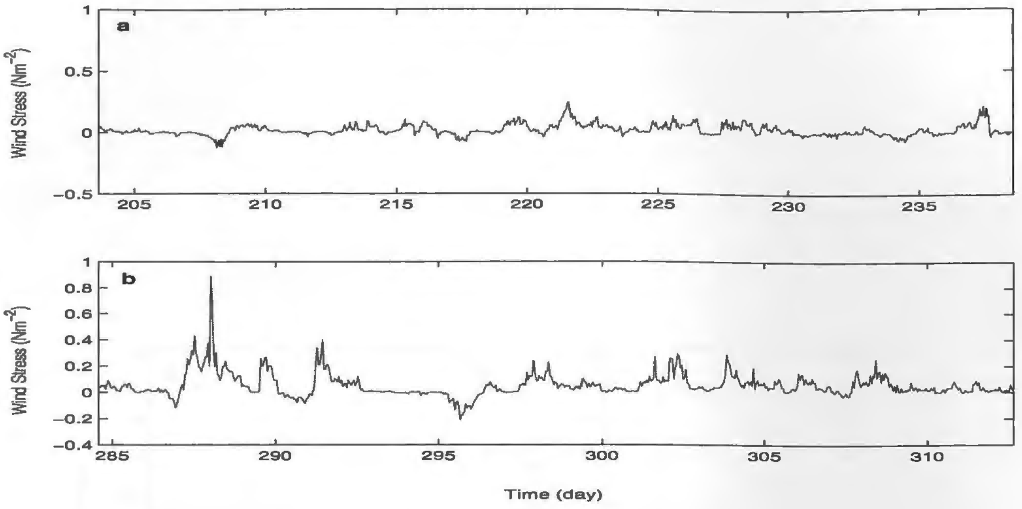

Figure 2.9: Time series of along channel wind stress in July/August(top) and October/November, 1999.

a correlation coefficient of 0.58. From day 286 to day 289, there is a strong peak of along channel wind stress with the outflow direction (Figure 2.9 b), reaching 0.8 Nm^{-2}, while during the same period, the surface outflow also has a strong peak reaching 20 cm/s, and in the lower layer below 5 m depth, the current direction is opposite (inflow) to that in the surface layer and reaches -20 cm/s (Figure 2.8 a and b). In Figure 2.8, more such coherent features between wind stress and along channel current can be seen, for example from day 291 to 292. Figure 2.10 shows more clearly the relationship between wind stress and the other factors. In the figure (Figure 2.10 a and b), the bottom temperature and bottom along channel velocity decreases (inflow) when wind stress increasing (outflow), which means while the wind is blowing water out harbor on the surface layer its effect at bottom layer is opposite with generating inflow to the harbor. Similar phenomenas have been observed in elsewhere, e.g. in Puget Sound (Matsuura, 1997).

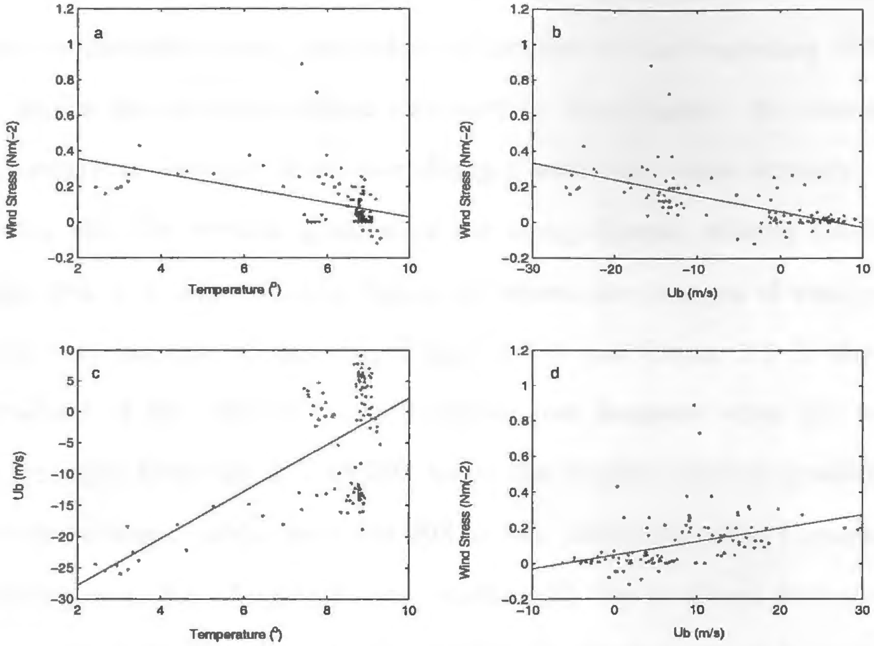

Figure 2.10: Plot of a)T-τ, b)U_b-τ, c)T-U_b, d)U_s-τ. T:bottom temperature, τ:wind stress, U_b:along channel velocity at 15m depth, U_s:along channel velocity at 3 m depth.

Mean along channel velocity profile of observation data in October/November is shown in Figure 2.5 *b*. It proves the expected two-layer circulation of an estuary with an flow out of about 4cm/s at 3m and inflow below 5m depth with a peak flow of over 6cm/s at about 10m depth. Compared with Figure 2.5 *a*, the along channel velocity profile shows a two-layer structure, with outflow in upper layer (above 5 m) and inflow in lower layer. The 3-day averaged velocity profile (Figure 2.6 b) also proves that this two-layer structure dominates from the middle of October to the beginning of November. Moreover, unlike the velocity vertical structure in July/August, the intensity of the vertical structure in October/November changes with time more strongly. In Figure 2.6 b), at day 288, the vertical gradient of the along channel velocity reaches 0.03/s, while at day 294, it is only 0.002/s. Figure 2.9 shows the changes of wind stress with time for the two periods. Comparing Figure 2.6 b and Figure 2.9 b, the strongest vertical gradient of the velocity in the Narrows just happens when the wind stress fluctuates strongly, from day 287 to 289, while the weakest vertical gradient appears when wind stress keeps stable, from day 293 to 295. Also comparing Figures 2.9 a and b, the wind stress in July/August is more stable with the standard deviation of 0.043 Nm^{-2} that is much smaller than that in October/November, which is 0.091 Nm^{-2}.

Comparing the bottom temperature and bottom current velocity of the two observation period (Figure 2.7 c and d, and Figure 2.8 c and d), we can see that except periods with strong oscillating wind stress, the bottom temperature in October/November keeps stable, and the bottom current velocity keeping negative (inflow) most of the time, while in July/August, the bottom flow is more complicated with the temperature and velocity vibrating strongly, the bottom flow changing direction continuously during the whole period (Figure 2.8 d). The possible explanation of this difference between the two observation period will be discussed in next section with the combination of the observation result of 2000.

2.3.2 Observation Data of 2000

Summary statistics for data from 2000, the mean, standard deviation, maximum in each velocity component at some specific depth are tabulated in Appendix A. Figures 2.11-2.13 show the time series of along channel velocity, bottom temperature and wind stress at moorings N2-N3. Comparing plots in Figure 2.11a and 2.13a with 2.12a, currents from N2 and N4 moorings are more variable than that at N3 mooring. The reason of this phenomena can be explained as the effect the bottom topography (Figure 2.2) which is perhaps more complicated at N2 and N4 than that of N3. Moreover, the coastal boundary friction is another influence that can affect the current of N2 and N4 more as they are closer to the shoreline compared with N3. From Figure 2.11-2.13,

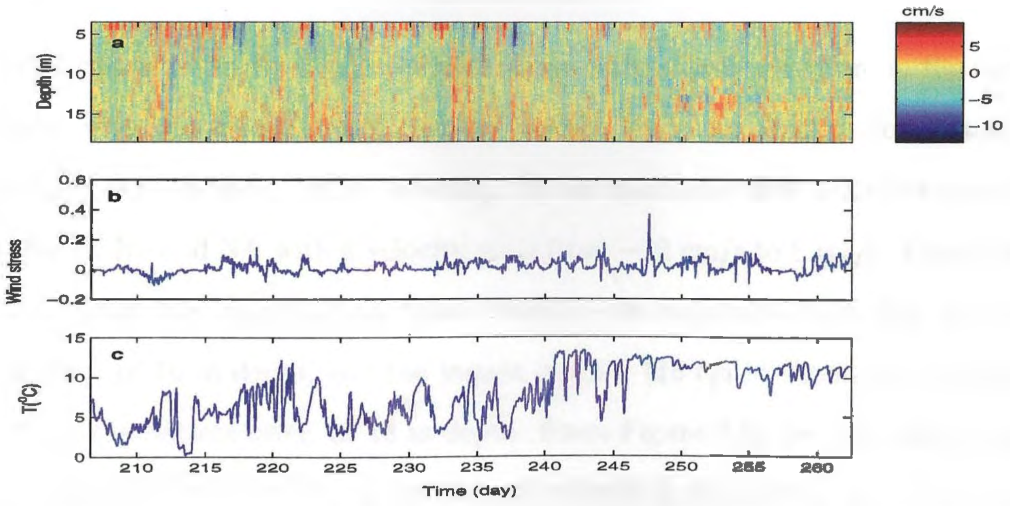

Figure 2.11: Time series data at N2, 2000, from top to bottom: velocity along the channel, along channel wind stress, bottom temperature. (+) denotes outflow, (-) denotes inflow.

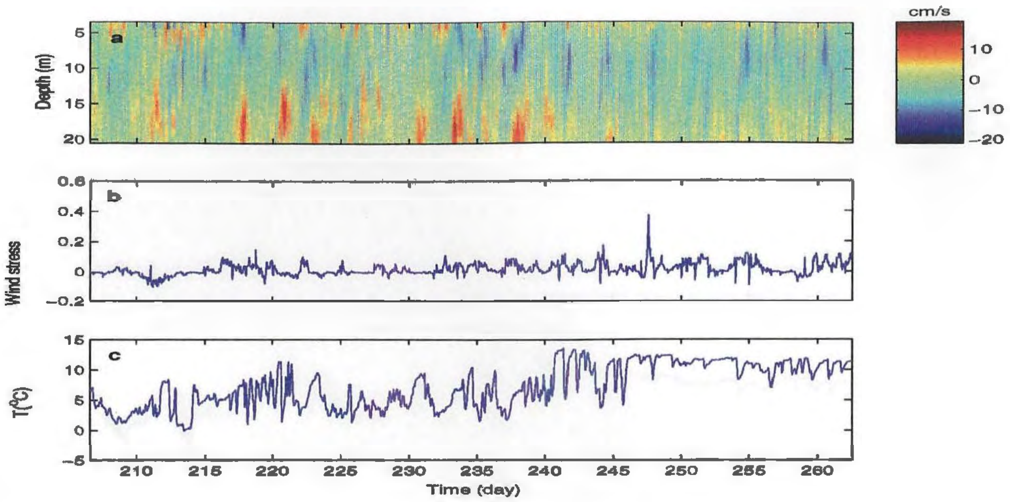

Figure 2.12: Time series data at N3, 2000, from top to bottom: velocity along the channel, along channel wind stress, bottom temperature. (+) denotes outflow, (-) denotes inflow.

the along-channel velocity in the Narrows shows a three-layer structure in the vertical direction, with the inflow focusing on the middle layer and outflow dominating the surface and bottom layer. At N2 mooring, the along-channel flow is weaker compared with that at N3 and N4, with a velocity scale from −12 cm/s to 8 cm/s (Figure 2.11). At N3 mooring, the largest inflow which reaches −20 cm/s appears on day 238 in the middle layer at 10 m depth, and the largest outflow (18 cm in the figure) appears at day 234 in the bottom layer, at 18 m depth. From Figure 2.12 ,we can also see at N3 mooring, from day 215 to 225, along channel velocity in the middle layer and bottom layer during the whole observation period shows an oscillation with a frequency about 0.5 cpd, with the same phase in each layer. The along channel velocity at N4 mooring is not as strong as that at N3. The highlight of in Figure 2.13a is the relative strong outflow, reaching 7 cm/s, around day 212 which almost dominates over the whole water

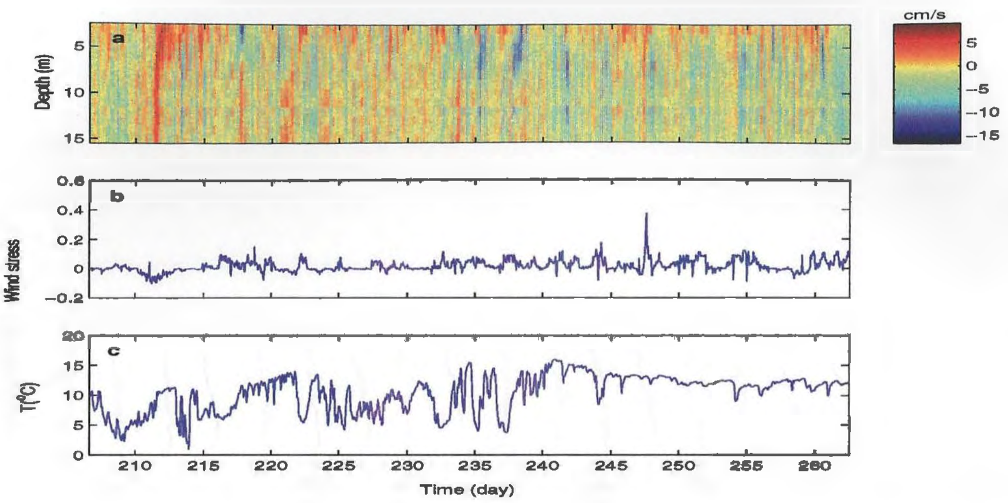

Figure 2.13: Time series data at N4, 2000, from top to bottom: velocity along the channel, along channel wind stress, bottom temperature. (+) denotes outflow, (-) denotes inflow.

column, while at other times, inflow dominates.

Another interesting feature of the observations from 2000 is the strong bottom outflow at N3 moorings clearly declines in the second half observation period (after day 240), and gradually disappears. This phenomena can also be noticed at the same period in the observation result of 1999 (Figure 2.7 and 2.8). The bottom temperature from all three moorings (plot *c* in Figure 2.11-2.13) also illustrates this phenomena as the temperature vibrates sharply when the bottom outflow is strong and becomes stable when the bottom outflow getting weaker (after day 240). Similar phenomena also exist in 1999 (plot *d* of Figure 2.7 and 2.8). Data from both years indicate that the bottom outflow in the Narrows have a seasonal-dependent feature during summer time.

Figure 2.14 shows 3-day averaged along channel current velocity profile of moorings

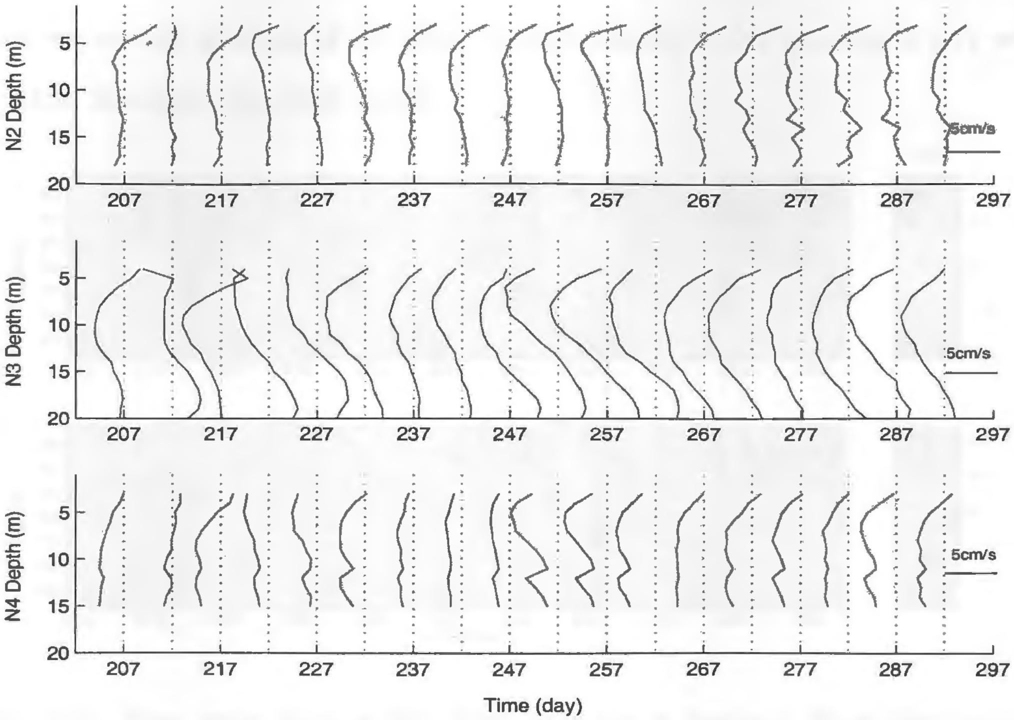

Figure 2.14: 3-day averaged profile of the along channel current in 2000. a: N2 mooring, b: N3 mooring, c: N4 mooring. (+) denotes outflow, (-) denotes inflow.

N2-N4. From Figure 2.14a and b, three-layer vertical structure exists at mooring N2 and N3, with outflow in the surface layer and bottom layer and inflow in the middle layer. The vertical structure at N2 and N3 moorings is strongest between day 252 to 262 with a vertical gradient reaches $-0.025s^{-1}$. In Figure 2.14b, the 3-day averaged inflow in the middle layer reaches the largest, −6 cm/s, at day 257. In Figure 2.14c, we can see vertical gradient of the along channel velocity at N4 mooring is very weak, and inflow dominate the whole depth.

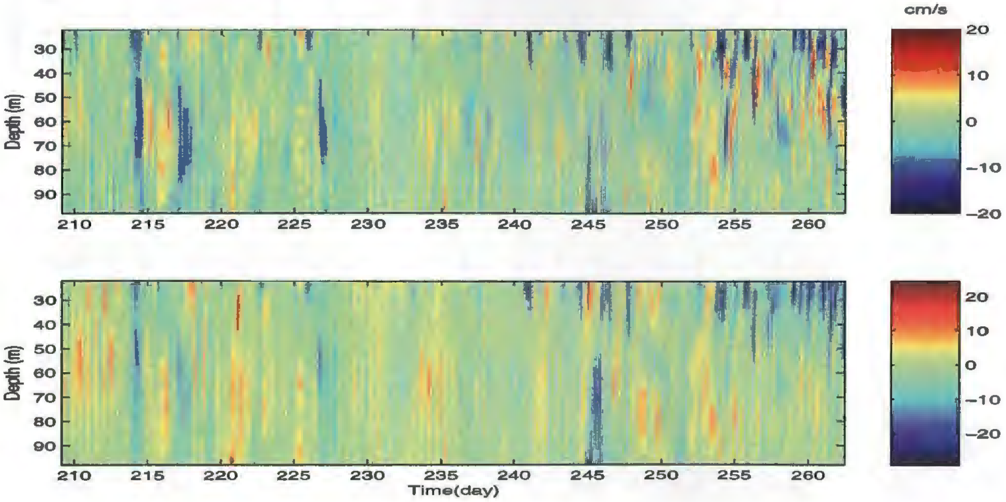

Figure 2.15: Time series data at H2, 2000, from top to bottom: East-West velocity, South-North velocity.

Figure 2.15 shows the velocity time series of H2 mooring outside the harbor. The current velocity at H2 mooring has an oscillation of about 0.5 cpd in both directions, West-East and South-North directions, and the stratification is weak as the vertical gradient of the velocity in both direction is very small (Figure 2.15). Figure 2.16 is the 3-day averaged velocity profile of H2. Plot b (Figure 2.16) shows that the southerly (negative) current dominates the whole depth of H2 mooring as expected. From the

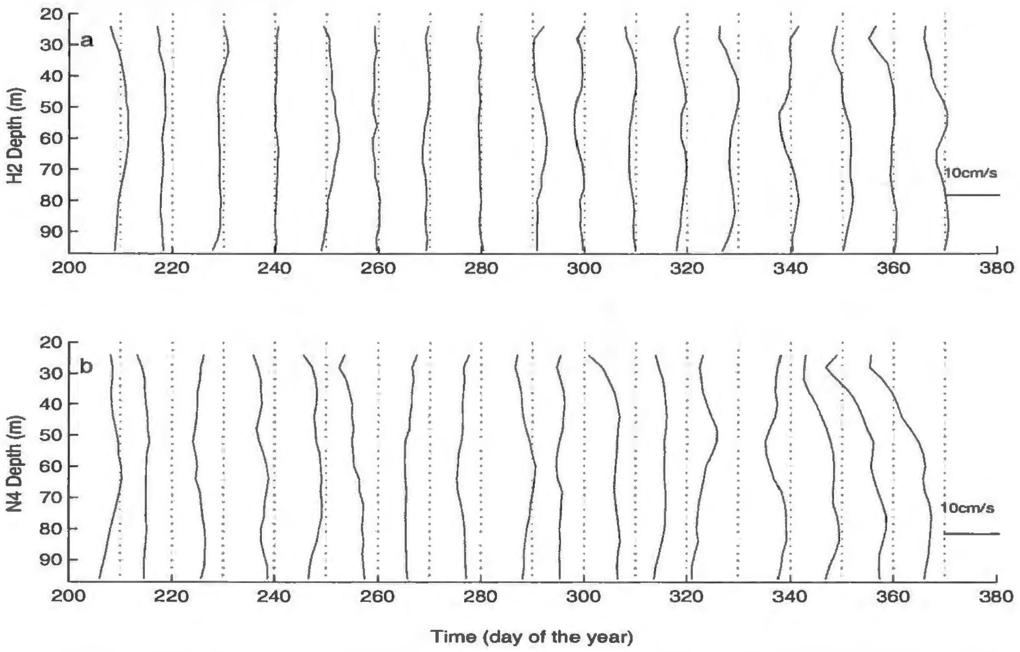

Figure 2.16: 3-day averaged profile of current velocity at H2 mooring. a: East-West direction, b: South-North direction.

raw data, it is difficult to see the relationship between the flow outside the harbor and in the Narrowss. The influence of the external forcing to the flow in the Narrows will be discussed later in the next chapter.

Chapter 3

Data Analysis and Its Result

3.1 Method Used in Analysis

3.1.1 Harmonic Tidal Currents Analysis

The harmonic method, invented by Lord Kelvin in 1876, is the most common method used for predicting tides. As equilibrium tidal theory tells us, the force causing ocean level up and down is the sum of the gravity force of sun, moon and earth. After some mathematical transformation, this tide-producing force can be expressed as a series of constituents with the form of a combination of sine and cosine functions. Therefore, the ocean tides, caused by this force, can be decomposed into a series of tidal constituents each with specified frequency and initial phase. As the tidal energy is very peaky in the observation data, so its amplitude and Greenwich phase lags can be extracted out by just filtering a specific harmonic frequency to the observation data. This approach is called Harmonic Tidal Analysis. If we apply to method to observation current data, it can be called as Harmonic Tidal currents Analysis. In this paper we use

Harmonic Tidal Analysis of the Institute of Ocean Science, developed by M. Foreman in 1979.

The basic theory is best devolved using complex variable analysis. Supposing that the tidal constituents comprised each current component occurrat specific frequencies, σ_j, $j = 1, 2...M$. Then for any current observation signal $U(t)$ can be expressed as, (Godin, 1972)

$$U(t) = u_0(t) + \sum_{j=1}^{M}[u_j cos2\pi(\sigma_j t - \varphi_j) + v_j cos2\pi(\sigma_j t - \theta_j)] \tag{3.1}$$

Here, $u_0(t)$ denotes the inertial term depending only on time t, u_j and v_j denote the components in x and y directions, and φ_j and θ_j denote the initial phase angle. Then, with some trigonometric function transformation, and also letting $cu_j = u_j cos2\pi\varphi_j$, $su_j = u_j sin2\pi\varphi_j$, $cv_j = v_j cos2\pi\theta_j$, $sv_j = v_j sin2\pi\theta_j$,

$$\begin{aligned} U(t) = u_0(t) + &\sum_{j=1}^{M}[(cu_j cos2\pi\sigma_j t + su_j sin2\pi\sigma_j t)] + \\ &\sum_{j=1}^{M}[i(cv_j cos2\pi\sigma_j t + sv_j sin2\pi\sigma_j t)] \end{aligned} \tag{3.2}$$

and after some algebra,

$$\begin{aligned} U(t) = u_0(t) + &\sum_{j=1}^{M}[(cu_j + sv_j) + i(cv_j - su_j]exp(2\pi\sigma_j t) + \\ &\sum_{j=1}^{M}[(cu_j - sv_j) + i(cv_j + su_j)]exp(-2\pi\sigma_j t] \end{aligned} \tag{3.3}$$

Consider a general term, so we can throw off the constituent numbering suffix j in equation (3.3) and define

$$\begin{aligned} a^+ &= [(\frac{cu+sv}{2})^2) + (\frac{cv-su}{2})^2], \\ a^- &= [(\frac{cu-sv}{2})^2) + (\frac{cv+su}{2})^2], \\ \epsilon^+ &= arctan(\frac{cv-su}{cu+sn}), \\ \epsilon^- &= arctan(\frac{cv+su}{cu-sn}), \end{aligned} \tag{3.4}$$

put equation (3.4) into equation (3.3), we get

$$\begin{aligned} Ut(t) &= a^+exp(i\epsilon^+ + 2\pi\sigma t) + a^-exp(i\epsilon^- - 2\pi\sigma t) \\ &= exp[i(\frac{\epsilon^+ + \epsilon^-}{2}][(a^+ + a^-)cos(\frac{\epsilon^+ - \epsilon^-}{2} + 2\pi\sigma t) \\ &+ i(a^+ - a^-)sin(\frac{\epsilon^+ + \epsilon^-}{2} + 2\pi\sigma t)] \end{aligned} \tag{3.5}$$

In equation (3.5), the first expression reveals that the former vector has length a^+, rotates counterclockwise, and the initial phase is at ϵ^+ radians which is counterclockwise from the positive X axis; while the latter has length a^-, rotates clockwise and the initial phase is at ϵ^- radians which is clockwise from the positive X axis. From the second expression, we can see over a time period of $1/\sigma$ hours, the path of the composite vector traces out an ellipse (or a line segment, in the degenerate case when $a^+ = a^-$) whose respective semimajor and semiminor axis lengths are $a^+ + a^-$ and $a^+ - a^-$, and whose angle of inclination from the positive X axis is $(\epsilon^+ + \epsilon^-)/2$ radians.

For real tidal current analysis, considering we have a time-series observation data, at time $i = 1, 2, ...N$. We can break equation (3.1) into X and Y axis, and get 2N equations. In this equation system, σ_j, $u(i)$ and $v(i)$ are known, and $u_0, v_0, u_j, v_j, \varphi_j$ and θ_j are unknown. So we have 2N equations and $4M + 2$ unknown variables. If $2N = 4M + 2$, we can solve the equations perfectly, but usually, in order to get rid of the effect of some noise such as observation error and cutoff error. $2N > 4M + 2$. So the equations is a conflict equation system, we can use least square method to solve it.

3.1.2 Empirical Orthogonal Function Analysis (EOF)

EOF analysis, which is also called Principal Component Analysis, is a technique that is used to identify patterns of simultaneous variation. Invented by Pearson in 1902, EOF analysis was introduced into meteorology by Lorenz (1956). Later, it was applied in oceanography. The goal of EOF analysis is to extract a compact or simplified but "optimal" representation of data with both space and time dependence.

Consider that we have a variable $V_m(t)$ at M stations, which might represent the temperature at M stations as functions of time. The variable is observed at N times, $t_1, t_2, t_3, ...t_N$. Expand $V_m(t)$ as follows:

$$V_m(t_i) = \sum_{k=1}^{M} X_{km} P_k(t_i) \tag{3.6}$$

Here X_{km} are unknown time-independent basis functions, which will be EOFs, and $P_k(t_i)$ are unknown time-dependent coefficients or amplitudes. The total number of X is the same as the total number of stations as the spatial information is also contained in X. Therefore, if the sum in equation (3.6) is taken over all of the X, then we can recover the input field, with no loss of information.

Suppose, however, that we truncate the series:

$$V_m^K(t_i) = \sum_{k=1}^{K} X_{km} P_k(t_i) + E_m^K(t_i) \tag{3.7}$$

Where $K < M$, and $E_m^K(t_i)$ is the error associated with the truncation. We would like to choose X_{km} and $P_k(t_i)$ in such a way that

$$R^K \equiv \sum_{m=1}^{M} (E_m^K)^2 \tag{3.8}$$

is minimized for a given K, which is similar to least square method. Loarenz (1956) shows that R^K is minimized if we choose X_{km} and $P_k(t_i)$ so that

$$\sum_{m=1}^{M} X_{km}X_{jm} = \delta_{kj} \equiv \begin{cases} 1 & if \quad k=j \\ 0 & if \quad k \neq j \end{cases} \tag{3.9}$$

and

$$N\overline{P_k^* P_j^*} = a_k \delta_{kj}, \tag{3.10}$$

where $a_k \geq a_{k+1} \geq 0$. Here $\overline{()}$ denotes a time average, and * denotes a departure from the time average. Equation 3.9 means that the EOFs are orthogonal in space. Equation (3.10) means that the amplitudes of the EOFs are orthogonal in time. This orthogonality in both space and time makes the EOFs an "optimal" representation of the data. The fact that R^k is minimized demonstrates this, but there is another way to see it. Suppose that we have chosen a first or "lowest-order" basis function to represent the spatial structure of our data, and that we now wish to make the best possible choice of second basis function. Clearly, the worst possible choice would be to make the second basis function the same as the first, because in that case the second function would contribute no additional information beyond what was already available in the first. This suggests that the second basis function should be "as different as possible" from the first; more precisely, the second function should be spatially uncorrelated with the first, and this is equivalent to the requirement of spatial orthogonality. Extending this reasoning, it is clear that a set of K basis functions should be chosen so that each is spatially orthogonal to the others. Similarly, the time-dependent amplitudes of the EOFs should be temporally orthogonal, to ensure that each new coefficient (with its EOFs) contribute as much new information as possible (Peixoto and Oort, 1992).

A method to solve for X_{km} and $P_k(t)$ is as follows. First, equation (3.6) can be rewritten as

$$Q = PX, \tag{3.11}$$

and (3.9)) and (3.10) become

$$XX^T = I, \tag{3.12}$$

$$P^{*T}P^* = D. \tag{3.13}$$

Here P, Q, P^*, Q^* are matrices of N rows and M columns, X is a square matrix of order M. $()^T$ denotes the transpose, I is the identity matrix, and D is a matrix whose non diagonal elements is zero and whose diagonal elements are a_k/N. (3.11)-(3.13) are merely the restatements of equations (3.6), (3.9) and (3.10), in matrix notation.

From (3.11), we can get Q as

$$P = QX^T \tag{3.14}$$

Defining

$$B \equiv Q^{*T}Q^* \tag{3.15}$$

so that the elements of B are proportional to the covariances of the Q. From 3.15, we have

$$Q^{*T}Q^* = (P^*X^*)^T(P^*X^*) \tag{3.16}$$

so, using equations (3.12) and (3.13),

$$\begin{aligned} X(Q^{*T}Q^*)X^T &= X[(P^*X^*)^T(P^*X^*)]X^T \\ &= P^{*T}P^* \\ &= D \end{aligned} \tag{3.17}$$

or, using (3.15),

$$XBX^T = D \tag{3.18}$$

From equations (3.12) and (3.18) we can solve for X and D, since B is known from equation (3.15). This is a standard "eigenvalue-eigenvector" problem. Once X is known, we can use (3.14) to find P. X is the eigenvector of the EOFs, and P is the principle component of the data calculated by EOFs.

As we know X is M square metrics, each column of X denotes one EOFs modes with the first to the last from left to right. The first EOF expresses that maximum fraction of the variance of the original data set that is possible with a single functional form. The second explains the maximum amount of the variance remaining with a function that is orthogonal to the first, and so on. So the first EOF is the spatial structure that explains the maximum possible amount of the variance, and its eigenvector is the amount of variance that it explains. Therefore, to be useful, EOF analysis must result in an decomposition of the data in which a big fraction of the variance is explained by the first few EOFs.

3.1.3 Spectral Analysis of Random Process

As the observational data used in this thesis can be considered as random time series data, spectral analysis can be a useful tool to deal with and interpret the meaning of the data. As it is not the main purpose of this thesis, here we only give the definition and some simple explanation of several spectral analysis functions used in this thesis. The functions explained here are: Power Spectral Density (PSD), Cross Spectral Density (CSD), and the Coherence squared.

For a random process $x(t)$, its finite mean power spectrum can be described as

$$\lim_{T\to\infty}\frac{1}{2T}\int_{-T}^{T}|x(t)|^2\,dt \tag{3.19}$$

The distribution of the total power in the frequency domain can be determined by a function G(f),

$$P_{xx}=\lim_{T\to\infty}\frac{1}{2T}\int_{-T}^{T}|x(t)|^2\,dt=\int_{-\infty}^{\infty}G(f)df \tag{3.20}$$

Here G(f) denotes the spectral density, and can be obtained from,

$$G(f)=\lim_{\Delta f\to 0}\frac{P_x(f,\Delta f)}{\Delta f}. \tag{3.21}$$

$P_x(f,\Delta f)$ is the mean-square value of the signal between the frequencies f and $f+\Delta f$, and can be determined by,

$$P_x(f,\Delta f)=\lim_{T\to\infty}\frac{1}{2T}\int_{-T}^{T}x(t,f,\Delta f)^2dt. \tag{3.22}$$

The function $P_{xx}(f)$ is the power density of this random process. With Fourier transform, $P_{xx}(f)$ can be described as,

$$P_{xx}(f)=\int_{-\infty}^{\infty}R_{xx}(t)e^{-i2\pi ft}dt \tag{3.23}$$

Here, R_{xx} denotes the autocovariance of the random process $x(t)$. As the measurements of the random process can be made only for finite intervals of length T. Therefore, the calculated PSD is only an estimate and is not identical with the true power spectrum. There are several methods available to calculate PSD, such as the Blackman-Turkey method (Blackman and Tukey, 1958) and periodogram method (Buttkus, 2000). In this thesis a modified periodogram method, Welch method, is used. In this method the time series data is divided into segments, a modified periodogram of each segment is calculated, and then the PSD estimates of all the segments are averaged.

Considering two random processes, $x(t)$ and $y(t)$, in the frequency domain, crosspower spectral density (CSD) function can also be defined in analogy to the power spectrum,

$$P_{xy}(f) = \int_{-\infty}^{\infty} R_{xy}(t)e^{-i2\pi f_t}dt \tag{3.24}$$

Here R_{xy} denotes the covariance matrix of the two random process.

Another important parameter to evaluate the relationship between two random variables is the coherence estimate (the value falls in (-1,1)). In this thesis coherence square is used and its function is as

$$C_{xy} = \frac{|P_{xy}|^2}{P_{xx}P_{yy}}. \tag{3.25}$$

where P denotes the spectral density.

3.2 Data Analysis Result

3.2.1 Tidal Current in The Narrows

We applied the harmonic tidal analysis of Foreman (1977), which require that the time series be in hourly intervals. To do this, data for the tidal analysis were first filtered using a third order low-pass butterworth filter with a pass band of 3 hours in order to remove high frequency fluctuations in the data. The data were then subsampled at 1-hour intervals as required by the tidal analysis software (Foreman, 1977).

Harmonic analysis of the data was carried out as discussed in Chapter 3.1.1. The length of the record allows for the determination of several additional constituents, but only four constituents which are most energetic in the Narrows are discussed here: Msf, O1, K1 M2 and S2. The reason for choosing the shallow water tidal constituent Msf is that in the coastal area, the interference between different tidal constituents increases as the depth decreases, and as the result of the interference between M2 and S2, the amplitude of Msf also grows larger, in some area even bigger than the amplitude of the main diurnal and semidiurnal tides.

Phase plane plots for the two years of data in the Narrows are presented in Figure 3.1-3.5. The plots show the amplitude and phase of the tidal constituent. The amplitude of the tide is the distance to the origin, and the phase of the tide is the angle from the x axis.

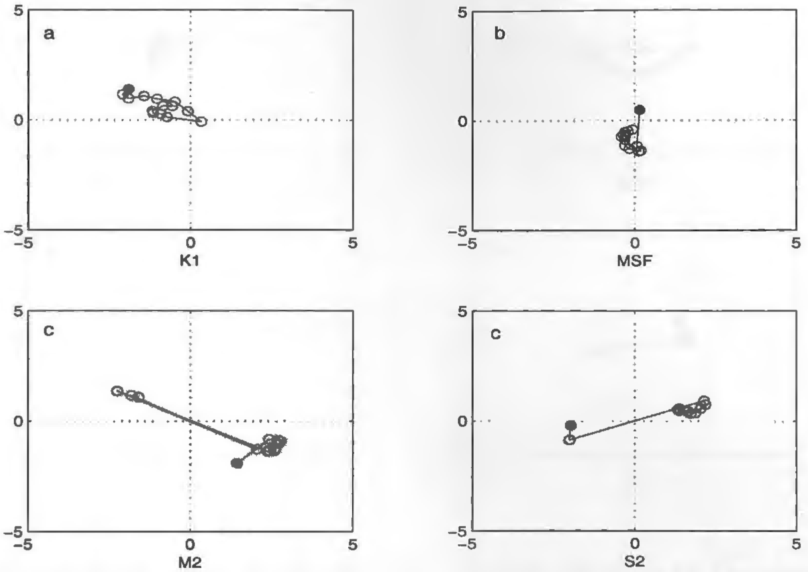

Figure 3.1: Phase plane plots of the K1, O1, M2 and S2 tides in July/August, 1999. The velocity scale is cm/s. The solid marker is at 2m depth.

Figure 3.1 and 3.2 show that the semidiurnal tide, M2 and S2, are the strongest constituents, and the shallow water tide, Msf, is also quite large in October/July. Also from the shape of the line, we can determine if a baroclinic response occurs in the tide. If all the points coalesce to a single point, indicating no variation in amplitude or phase

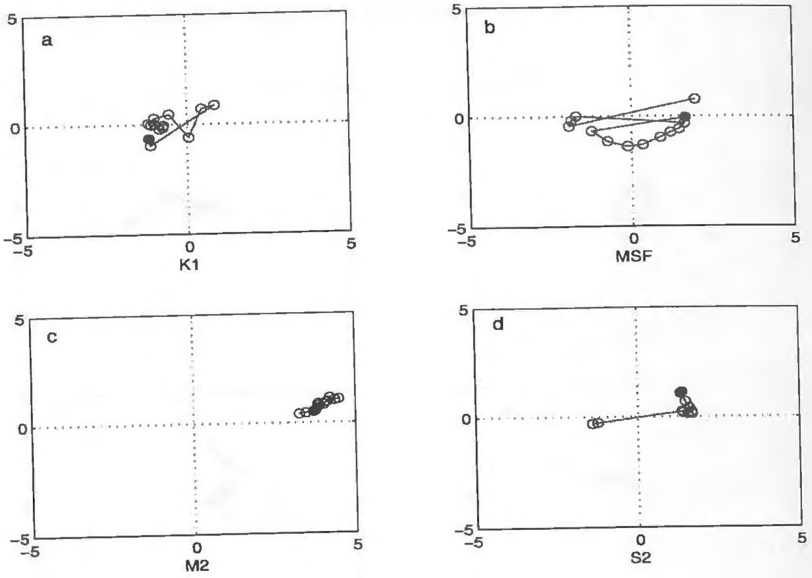

Figure 3.2: Phase plane plots of the K1, O1, M2 and S2 tides in October/November, 1999. The velocity scale is cm/s. The solid marker is at 3m depth.

with depth, then no baroclinic response is present. If a straight line is produced then just a single mode is present; if a curve is produced then more than one mode is present. In Figures 3.1-3.2, we can see plots of M2 and S2 are almost straight lines indicating that only one mode is present, and plots of K1 and Msf is much more complex which indicate more than one modes is present. Another interesting feature is the phase of M2 and S2 tides (plot c and d in Figure 3.1) in July/August changes almost 180^o at some depth which indicates strong internal waves in the flow.

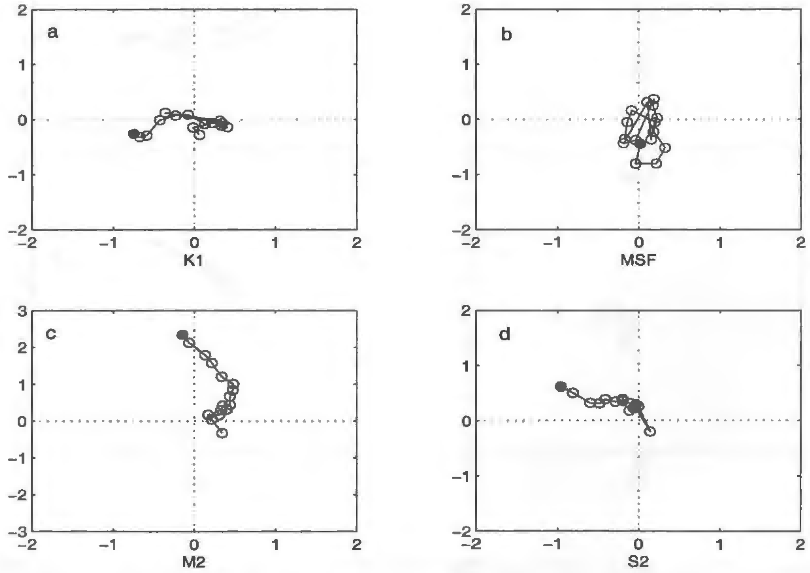

Figure 3.3: Phase plane plots of the K1, O1, M2 and S2 tides at N2 mooring in 2000. The velocity scale is cm/s. The solid marker is at 3m depth.

In Figures 3.3 to 3.5, showing results for 2000, semi-diurnal tides M2 and S2 dominate the tidal current of all the three moorings, with the average amplitude of M2 tide in the surface layer is more than 2 cm/s. The baroclinic response of all the tides is very clear as all the lines has at least one curve which indicated more than one modes

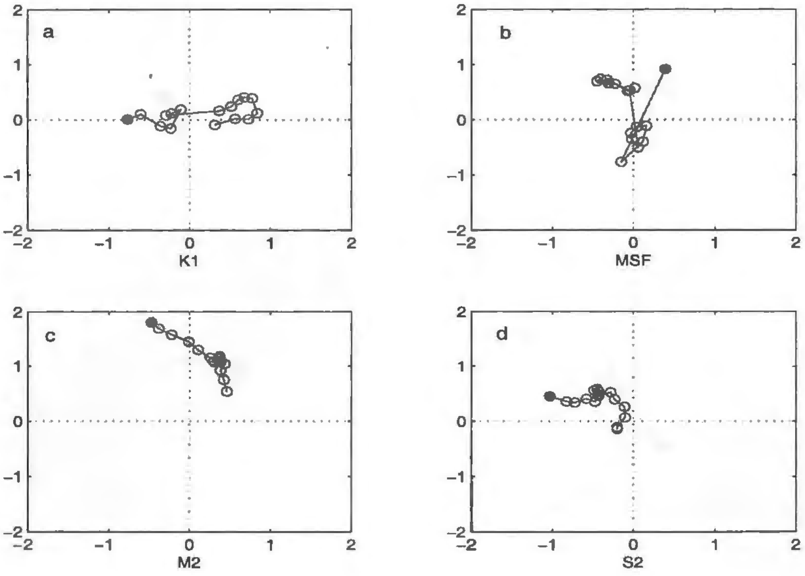

Figure 3.4: Phase plane plots of the K1, O1, M2 and S2 tides at N3 mooring in 2000. The velocity scale is cm/s. The solid marker is at 4m depth.

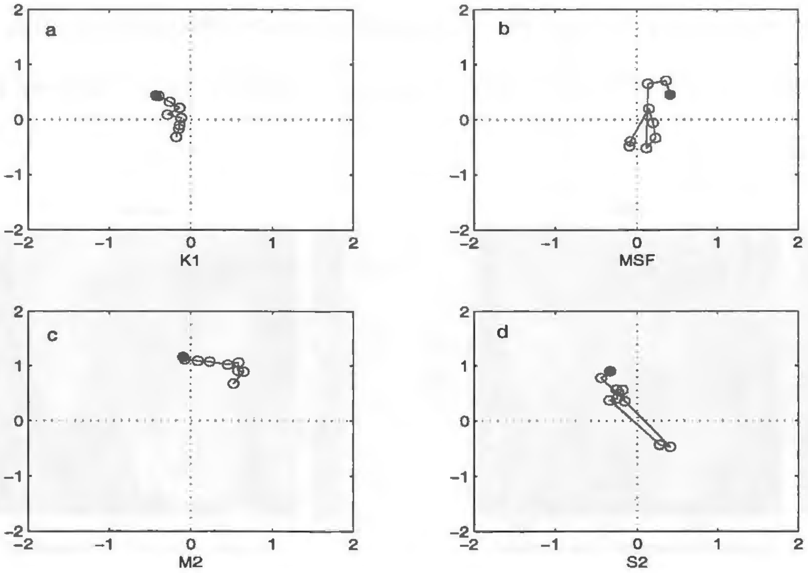

Figure 3.5: Phase plane plots of the K1, O1, M2 and S2 tides at N4 mooring in 2000. The velocity scale is cm/s. The solid marker is at 4m depth.

of internal tides is present. At N2 and N4, the amplitudes of M2 and S2 decrease with depth clearly. Compared with other tides, the shallow water tides Msf is more complex with no clear shape of the line in all three moorings. Combining plots of 1999, we can see that the amplitude of the tides in 2000 is smaller than that in 1999. The reason for this decline could be due to the different mooring locations of the two years. In 1999, the mooring was deployed at the sill between the Narrows and harbor where water depth is much shallower and the current can be greatly accelerated by this depth difference. Therefore, tidal current also grows faster when it flows from the Narrows to the sill.

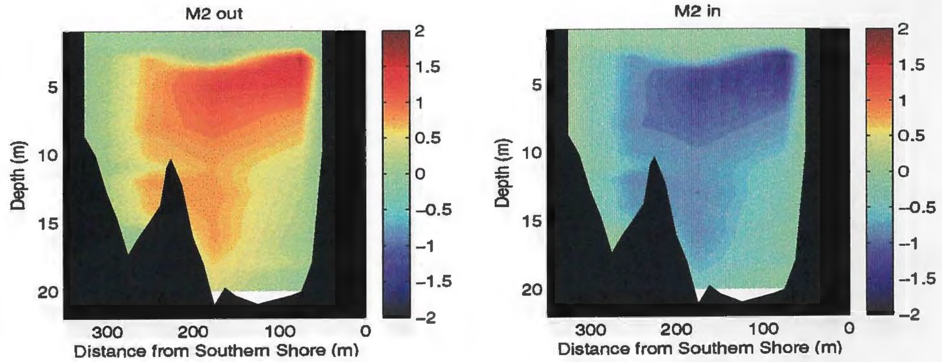

Figure 3.6: Cross channel distribution of the current amplitude of M2 tide

By interpolating the observation data into a grid spacing of 25 m (horizontal) by 1m (vertical), a two dimensional distribution of the speed of the tides is determined. The averaged cross channel inflow and outflow net flux of different tide components can be computed from this interpolated grid. In Table 3.1, we can see the net flux of inflow and outflow keeps balance for all the three main tidal constituents. This indicates that tidal current does not cause water transport to the harbor. Figure 3.6 to 3.8 show the cross channel distribution of mean out-flow and in-flow velocity of different tidal

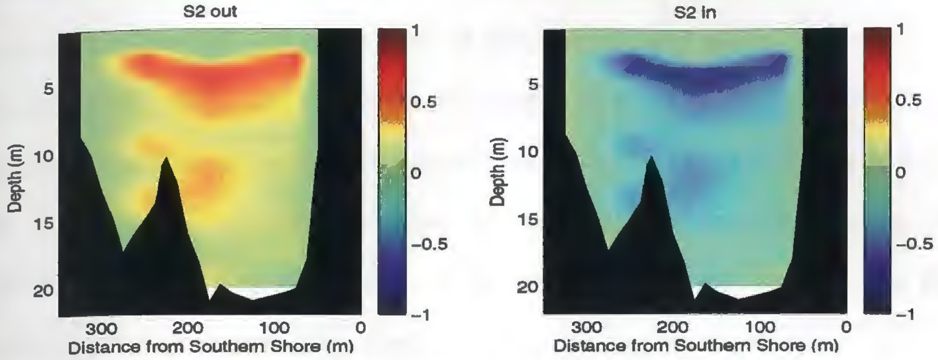

Figure 3.7: Cross channel distribution of the current amplitude of S2 tide

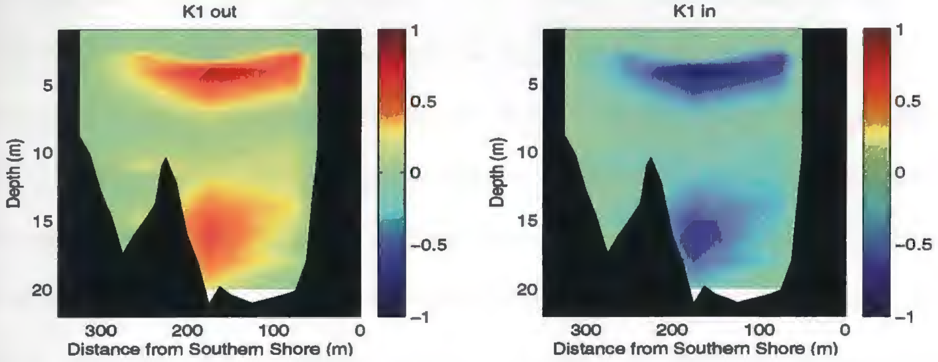

Figure 3.8: Cross channel distribution of the current amplitude of K1 tide

Table 3.1: Inflow and Outflow Net Flux of M2, S2 and K1 tide

Tide	Inflow flux (m^3s^{-1})	Outflow flux (m^3s^{-1})
M2	26.704	26.687
S2	11.052	11.049
K1	10.147	10.151

components, M2, S2 and K1. Apparently, the structures of outflow and inflow are very similar to each other and the amplitude of the outflow and inflow also almost equals. The velocity peak of S2 and K1 is in the center of the channel, between 4m depth and 5m depth, and the peak of M2 appears near the surface on southern side of the channel. Both the two semi-diurnal tides, M2 and S2, have another peak in the lower layer, about 12m depth, in the center of the channel, and the diurnal tide K1 has a peak near the bottom, below 15m depth.

3.2.2 Subtidal Current In The Narrows

Observations from 1999 (deYoung *et al.*, 2000) reveal strong inflow at 0.5 cpd frequency that extends from the bottom to the surface which indicates that low frequency signals could contribute a lot to the flow in the Narrows. But as there is only one ADCP used in 1999, so the representation of the data cross channel structure of the flow weak. In 2000, with more instruments deployed in the channel, we can study the low frequency flow in the Narrows more thoroughly and more reliably.

Usually subtidal current signals can be obtained by applying a low-pass (with a cutoff frequency of 0.8 cpd) filter to the ADCP data, but for the estuarine area, as the fortnightly tidal constituent can be strong compared with other constituents (section 3.2.1), a band-pass filter should be used. From the result of the harmonic tidal analysis in section 3.2.1, we can see the amplitude of Msf tide (with a frequency of 0.067 cpd) is quite strong and should be filtered out here. Power spectral density (PSD) of the raw data is also calculated. Figure 3.9 shows that the peak of power spectrum of the observation data is at low frequency, below 0.8 cpd, which means subtidal current is the most energetic part in the flow. Therefore, in order to filter both the high frequency signals and the fortnight tidal signal and keep the low frequency signal, three steps are

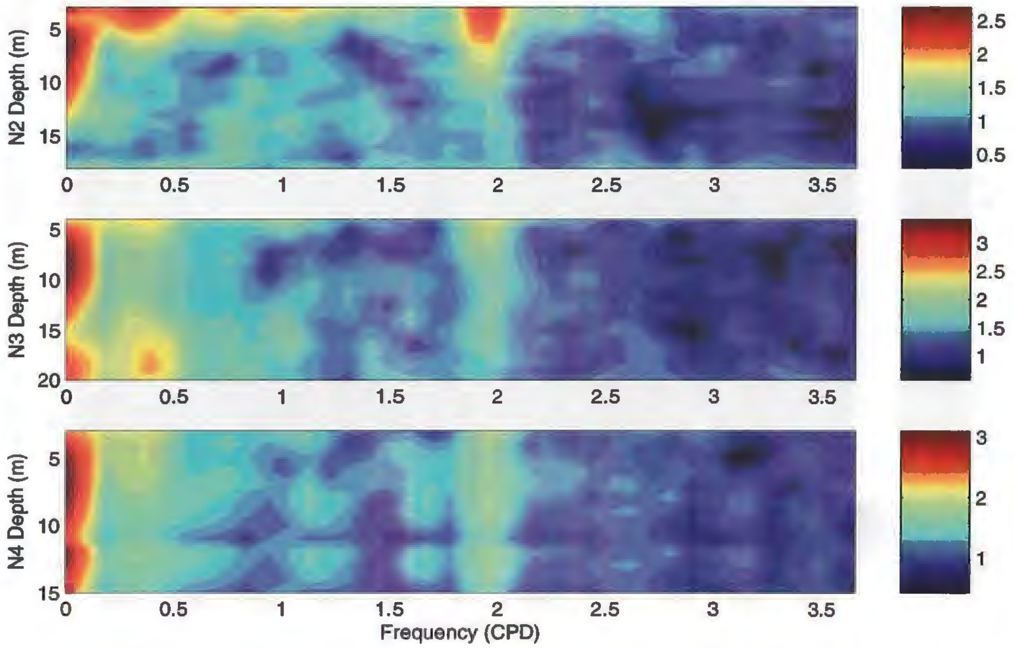

Figure 3.9: Power Spectral Density for the Narrows axial current velocity at N2-N4(from top to bottom)

followed here. Firstly, the inertial motion is eliminated from the raw current data; then, a third order low-pass Butterworth filter with a cut-off frequency of 0.7 cpd is used to filter the high frequency signals; finally, a band-stop filter with a cut-off frequency of 0.065 – 0.069 cpd is applied to filter the fortnight tidal signal. The wind data is filtered using a lowpass Butterworth filter with cur-off frequency of 0.7 cpd.

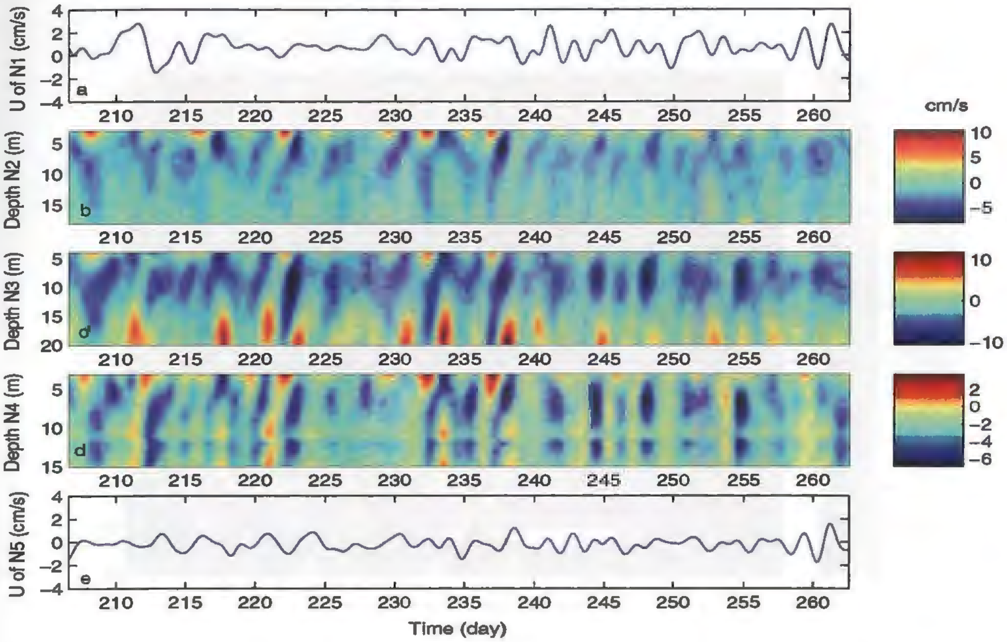

Figure 3.10: Time series of along channel sub-tidal current velocity at N1-N5 moorings. (+) denotes outflow, (-) denotes inflow.

The time series of the subtidal signal are shown in Figure 3.10. In Figure 3.10 (b and c), at N2 and N3 moorings, outflow exists both in the surface layer and bottom layer with an oscillation of 0.5 cpd, while at N4, (Figure 3.10 d) with the water depth shallower than the other two moorings, inflow dominates the whole depth and almost oscillates synchronously with the same phase. In Figure 3.10 b and c, the middle layer

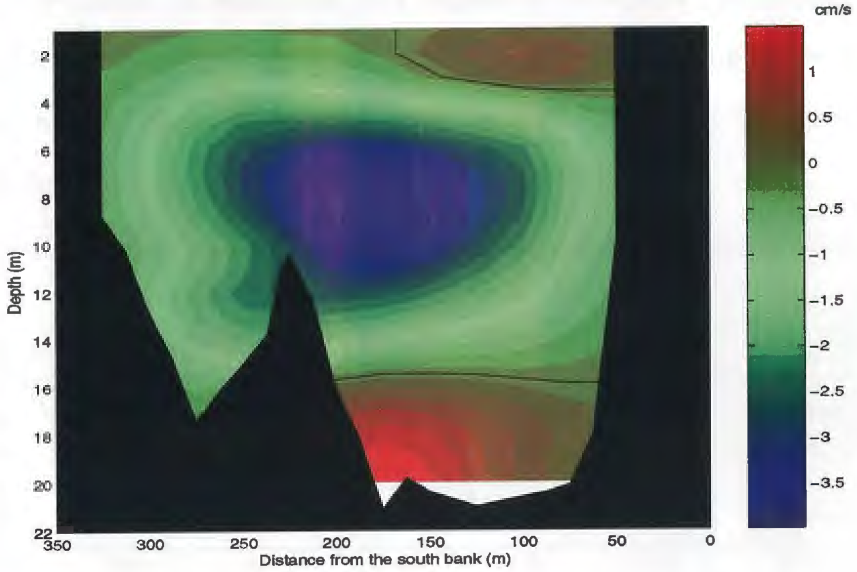

Figure 3.11: Cross channel distribution of the mean sub-tidal current velocity, The black line is 0 value line. (+) denotes outflow, (-) denotes inflow.

of N3 and N2 is dominated by inflow with an amplitude of -10 cm/s. An interesting feature is the strong outflow in the bottom layer at N3 mooring (Figure 3.11 and Figure 3.10, c) which reaches strongest around day 234, and then declines with time to almost zero at day 250. Similar phenomena were observed at the mouth in July/August, 1999 (section 2.3.1). This seasonal oscillation of the bottom outflow may be related to the oscillation of fresh water flux from the land. Water flux of Waterford river in the Harbor reaches lowest in September and highest in November (Environment Canada, www.ec.gc.ca). When the fresh water flux is weaker, the strong inflow drives down the outflow to the bottom layer, and when the fresh water flux becomes stronger, it dominates the upper layer again and the inflow is driven down.

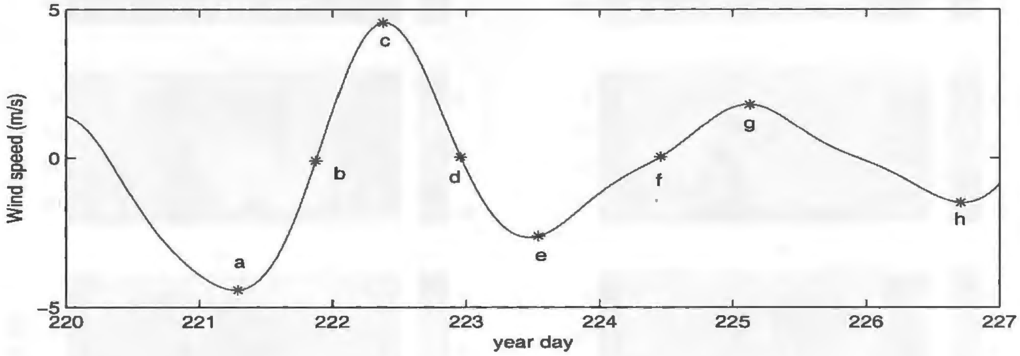

Figure 3.12: Wind speed during day 220-227. The eight asterisk points (a-h) denote the time spots chosen for plots in Figure 3.13.

The spatial structure of the mean subtidal current is shown in Figure 3.11. The peak of the mean inflow in the channel dominates the middle depth of the channel, while mean outflow only occurs in the center of the bottom layer and the southern side of the surface layer (Figure 3.11). In the figure only weak outflow in the surface layer (between 3 m to 5 m depth) is observed unexpectedly, and the reason of this can be due

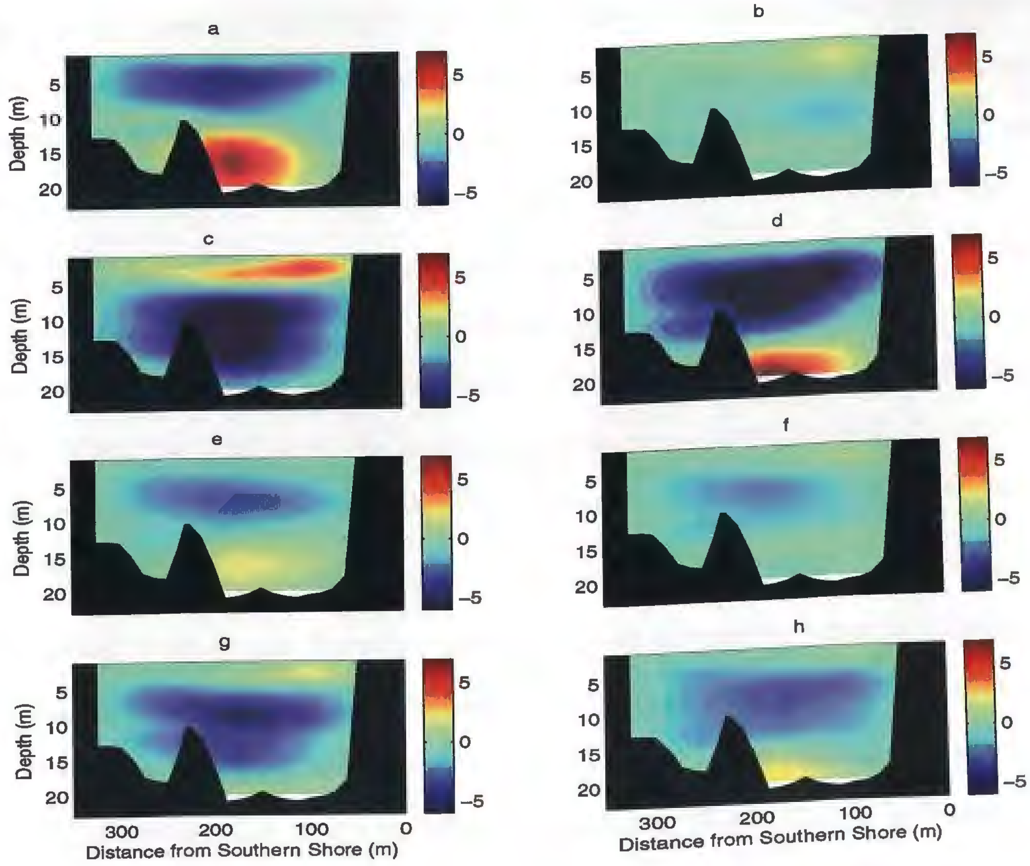

Figure 3.13: Spatial structure of subtidal current at 8 time spots shown in Figure 3.12. (+) denotes outflow, (-) denotes inflow.

to the lack of data above 3 m depth where the flow can be much stronger. Therefore, only consider the flow below 3 m depth as the surface layer will definitely underestimate the surface flow. This under estimate can be seen more clearly in Chapter 3.2.3 when surface transport is calculated. In order to study the time changes of this spatial structure, we choose 8 time points during day 220-227 and plots *a*-*h* in Figure 3.13 show the spatial structure of the subtidal current at different time spots. From the figure we can see the inflow in the middle layer exists all the time, but the center position and the strength of this inflow changes with time. An interesting phenomena in Figure 3.13 is the outflow in the surface layer and bottom layer never occurs at the same time. When the bottom outflow reaches the strongest (plots a), no outflow appears in the surface layer, and the inflow in the middle layer is driven up to 5 m depth. When the outflow in the surface layer is strong enough (plot c), no outflow appears in the bottom layer, and also the inflow in the middle layer is driven down to below 10 m depth.

Empirical Orthogonal Function (EOF) analysis is used to identify simultaneous variations of the sub-tidal data of different moorings. The result shows that about 70% of the total variance contributes to the first two modes, and mode 1 has more than 40% of the variance and is statistically significant (Figure 3.14). In Figure 3.14 a, the cross channel distribution of the eigenvectors of mode 1 has a significant two-layer structure in vertical direction with positive value in upper layer and negative value dominating lower layer, and the boundary of the two layers is at the depth of 7 m. In Figure 3.14 b, on the contrary to mode 1, the negative value dominates the first layer while the positive value only occurs in a thin bottom layer near south shore. Combining Figure 3.14 with Figure 3.13, we can see mode 1 and mode 2 together efficiently explains the main feature of the average cross channel distribution of the sub-tidal current. In

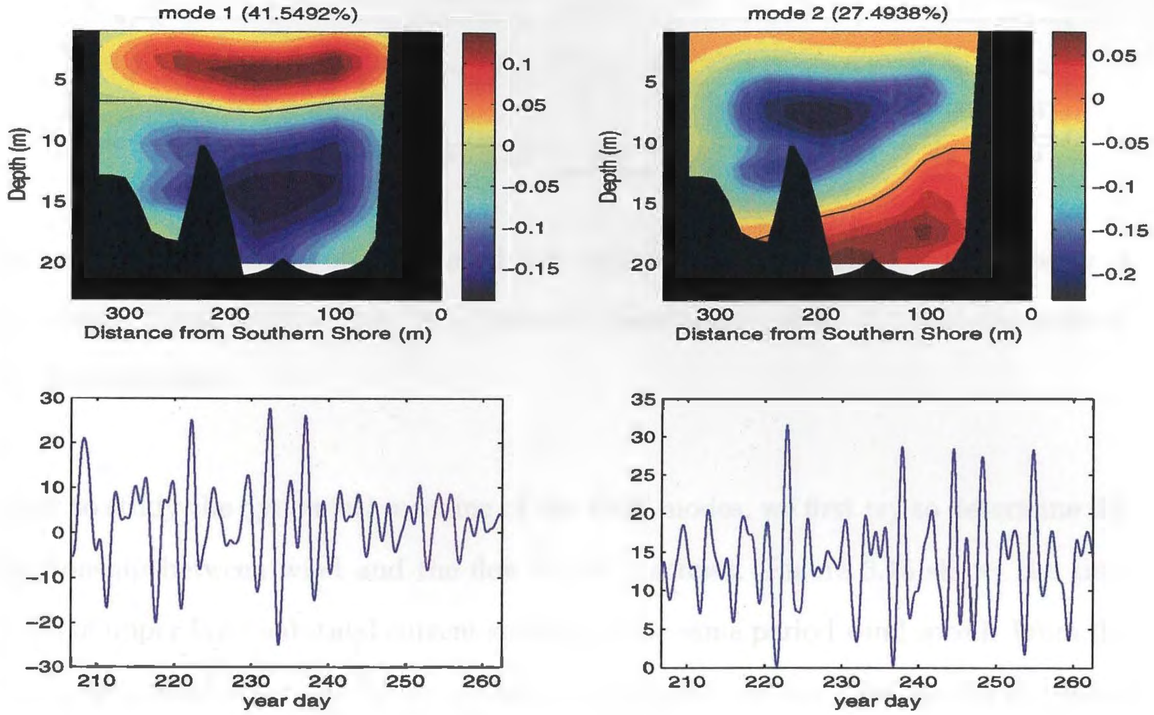

Figure 3.14: Cross channel distribution of eigenvectors of the EOF mode 1 and mode 2, The black line is 0 value line.

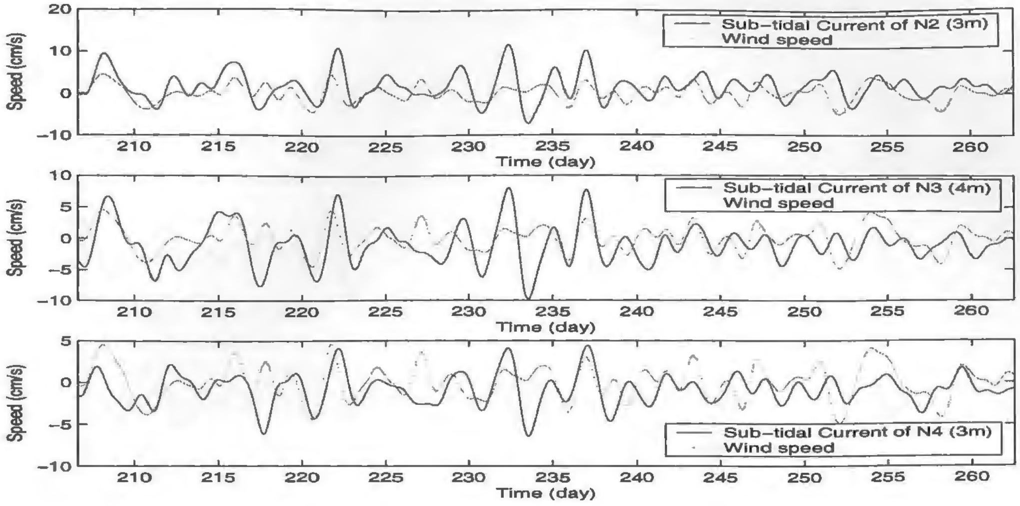

Figure 3.15: Time series of wind speed and up-layer sub-tidal axial current velocity of moorings. Wind velocity unit: m/s, current speed unit: cm/s. (+) denotes outflow, (-) denotes inflow.

order to study the dynamical meaning of the EOF modes, we first try to determine the relationship between wind and the flow in the Narrows. Figure 3.15 shows the time series of upper layer sub-tidal current speed and the same period wind speed. From the figure, we can see wind speed and current speed match each other well during the whole period except a small time lag. Furthermore, in order to study the wind influence to the flow in the lower layer, similar plots with the current speed in the lower layer is also plotted. In Figure 3.16, we can see that after multiplying the wind velocity by a negative constant, the changes of the two time series lines match each other well, which indicates that wind has a counter influence on the flow in the lower layer in the Narrows. Moreover, the coherence squared between of wind and subtidal current at N2-N4 moorings is shown in Figure 3.17. The highest coherence squared occurs at the depths of above 15 m and at the frequencies between 0.2-0.6 psd, at which frequencies

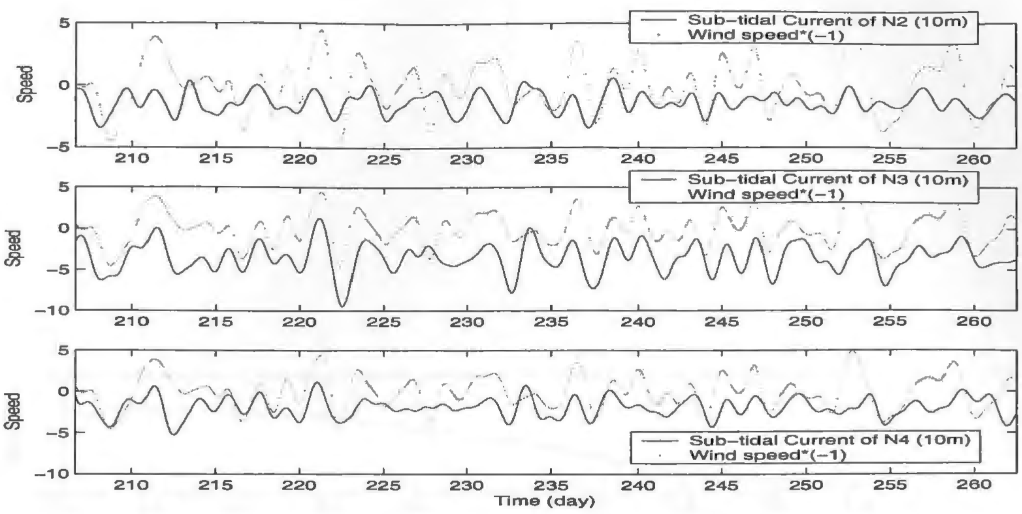

Figure 3.16: Time series of wind and lower-layer subtidal axial current velocity of moorings. Wind velocity unit: m/s, current speed unit: cm/s. (+) denotes outflow, (-) denotes inflow.

the power of the wind also peaks.

The net transport through the channel is also calculated with the method mentioned in section 3.2.1. The correlation coefficient between wind speed and axial sub-tidal transport is -0.74 which means the two variables are high related but with opposite direction. Figures 3.18-3.20 shows the comparison between wind speed and the net transport of upper layer (above 5 m), lower layer and the whole depth. In the Figures, we can see the transport in the upper layer does not match well with the wind speed, and a peak of coherence square occurs at frequency 0.5 cpd. But in the lower layer, the transport matches wind speed very well by timing the wind speed with a negative constant and the coherence square keeps high between frequency 0.4-0.7 cpd. In Figure 3.20, the coherence between transport and wind speed is significantly high after multiplying the wind speed with a negative constant. The reason of this is when calculating

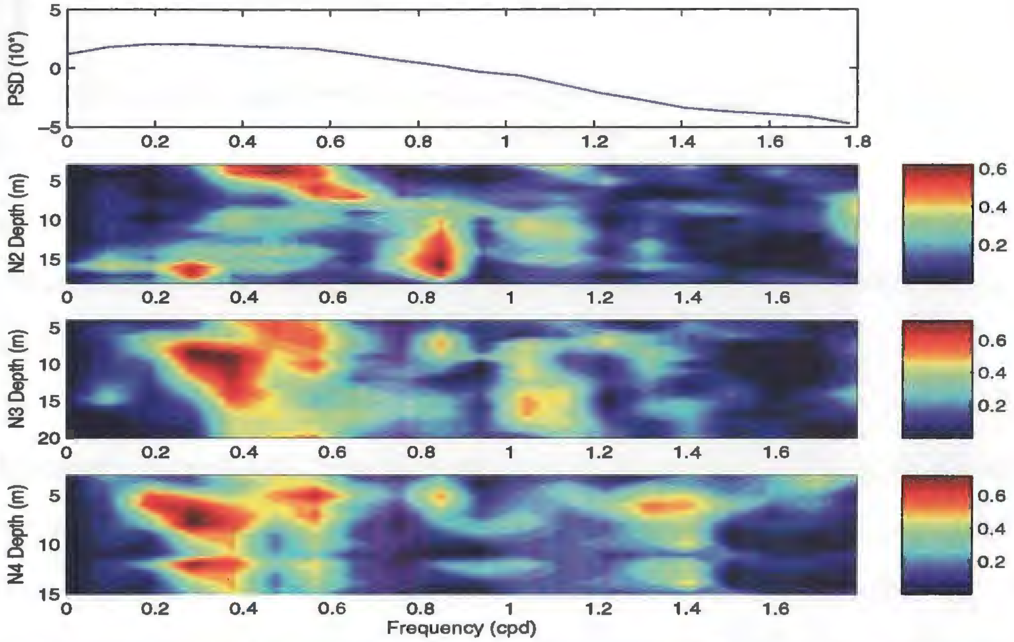

Figure 3.17: From top to bottom is Power spectral density of axial wind, Coherence between sub-tidal axial current from N2-N4 and wind speed

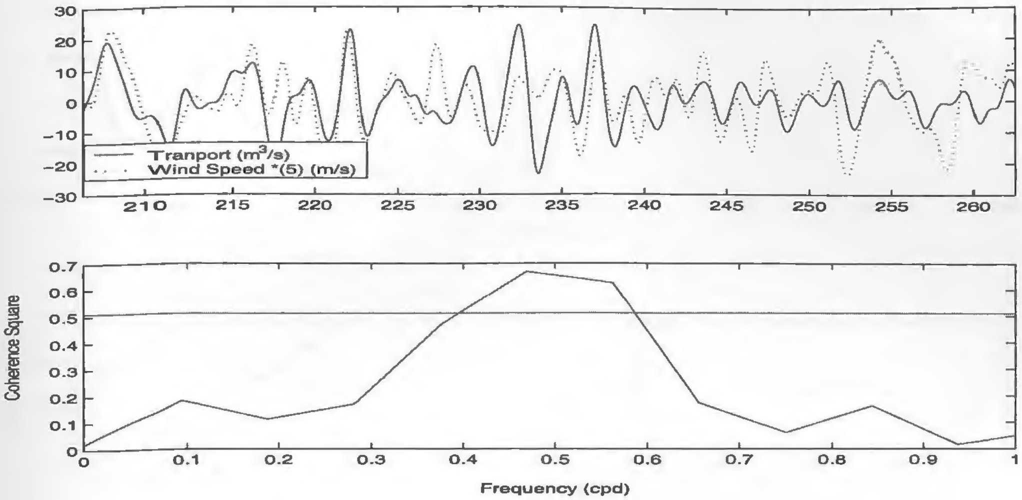

Figure 3.18: Time series of wind speed and axial upper layer sub-tidal transport (top) and coherence between them (bottom). (+) denotes outflow, (-) denotes inflow. The straight line denotes 95% confidence limit.

the transport, current data from the surface layer (above 3m), which is mostly effected by the wind, is not included, so the transport caused by the wind in the upper layer is underestimated in the whole transport and the transport in the lower layer dominates the direction of the calculated transport. Therefore, this also indirectly prove the counter influence of the wind to the lower layer. Combining Figures 3.15-3.20, we can get so that wind has a direct influence on the surface flow in the Narrows and a counter influence on the lower flow. The dynamical reason for this phenomena is that the current in the upper layer is forced by the wind stress, then in order to make up the water loss from the upper layer, water in the lower layer flows to the opposite direction of the upper layer.

Another method to study wind effect is to compare the acceleration of the current in the Narrows with wind stress. In Figure 3.21-3.22, we can see that the surface

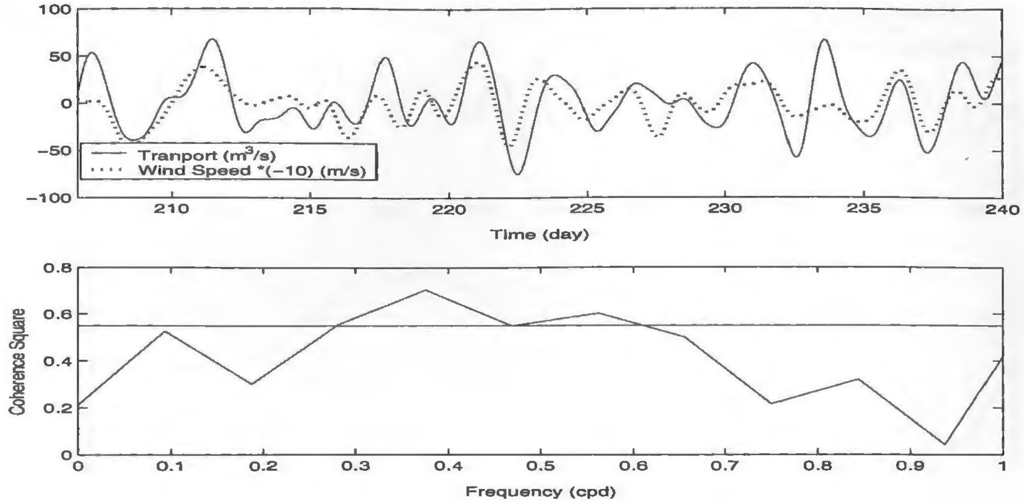

Figure 3.19: Time series of wind speed and axial lower layer sub-tidal transport (top) and coherence between them (bottom). (+) denotes outflow, (-) denotes inflow. The straight line denotes 95% confidence limit.

acceleration of the current in the Narrows in both years matches the wind stress very well. From the figure, the counter influence of wind to the lower layer is also presented clearly as the direction of the acceleration in the two layers is opposite to each other. In Figure 3.22, from day 217 to 220, the acceleration profile has a bottom layer and this feature is clearly not driven by the wind stress. Therefore, besides the along-channel wind, there must be other forces affecting the current in the Narrows, and this will be discussed later in this chapter.

Then, to study the relationship between wind and EOF mode 1, we calculate the correlation coefficient between wind and the principal component of EOF mode 1 which is -0.51, and this indicates that the two variables are highly correlated with each other but with opposite directions. The comparison between the principal components of EOF mode 1 and along channel wind speed is shown in Figure 3.23. In the figure, we

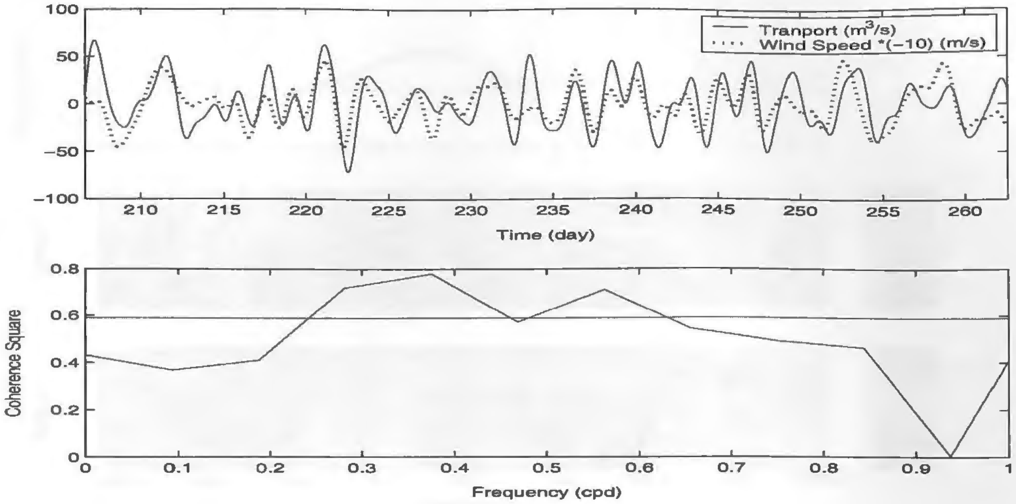

Figure 3.20: Time series of wind speed and axial sub-tidal transport (top) and coherence between them (bottom). (+) denotes outflow, (-) denotes inflow. The straight line denotes 95% confidence limit.

can see the two variables match each other well and the value of coherence squared is above 0.6 between 0.2 and 0.5 cpd. The coherence squared of EOF mode 1 with N-S wind velocity and N-S current velocity at H2 mooring is also calculated to compare with the coherence squared of EOF mode 1 and E-W wind speed. In Figure 3.24, the coherence square of EOF mode 1 with N-S current velocity at H2 mooring is apparently not significant as the value keeps less that 0.4 in the whole frequency scale, and this means that EOF mode 1 has no relation with the external forcing outside the harbor. Comparison with the coherence of EOF mode 1 with along channel wind velocity, the coherence of EOF mode 1 with N-S wind velocity is very small over most frequencies, and the only peak (> 0.5) appears in the low frequency. This shows that N-S wind velocity also contributes little to EOF mode 1. Therefore, combining Figures 3.17, 3.23 and 3.24, we can get a conclusion here that EOF mode 1 represents the contribution

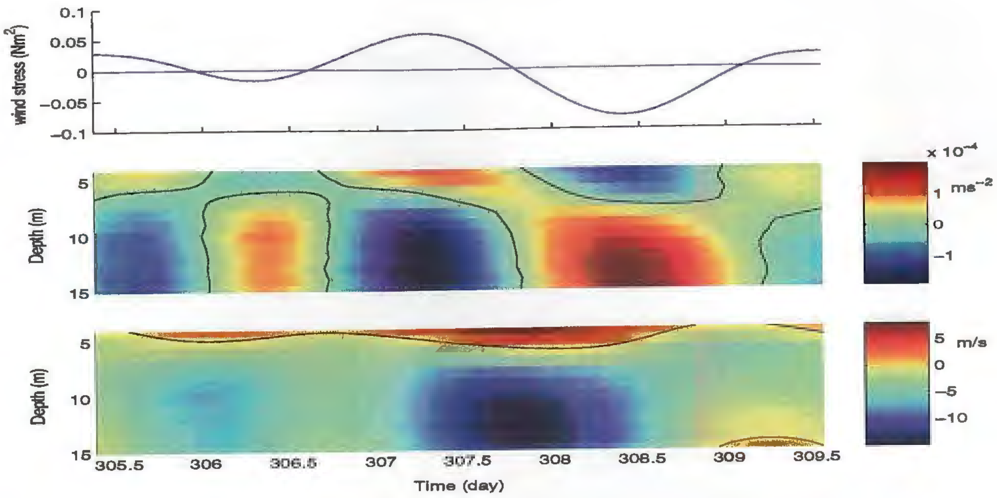

Figure 3.21: Time series of wind stress (top), acceleration of current velocity (middle) and current velocity (bottom) in 1999. (+) denotes outflow, (-) denotes inflow. The solid line denotes 0 isoline.

of the along channel local wind stress in the harbor.

As two moorings (H1 and H2) were also deployed outside the harbor, it provided possibility to study the influence from outside. Current data from H1 and H2 are also filtered with the same filter as data inside the Narrows. Figure 3.25 shows the PSD of observation data at H1 and H2. At 22m depth of Mooring H1 (plot a), there is no significant power spectrum peak within the frequency scale, and PSD decreases with the frequency increasing. At 77 m depth (plot b), the power spectrum peak appears below frequency 0.5 cpd, and it keeps stable with frequency increasing. At H2 (plot c), the power spectrum in the upper layer (above 24m) is much stronger than the lower layer, while PSD peak is also at the lower frequency (below 1 cpd).

Outside St. John's harbor is the wide continental shelf that is much deeper (average depth of more than 80 m) than the Narrows (average depth of about 20 m). The long

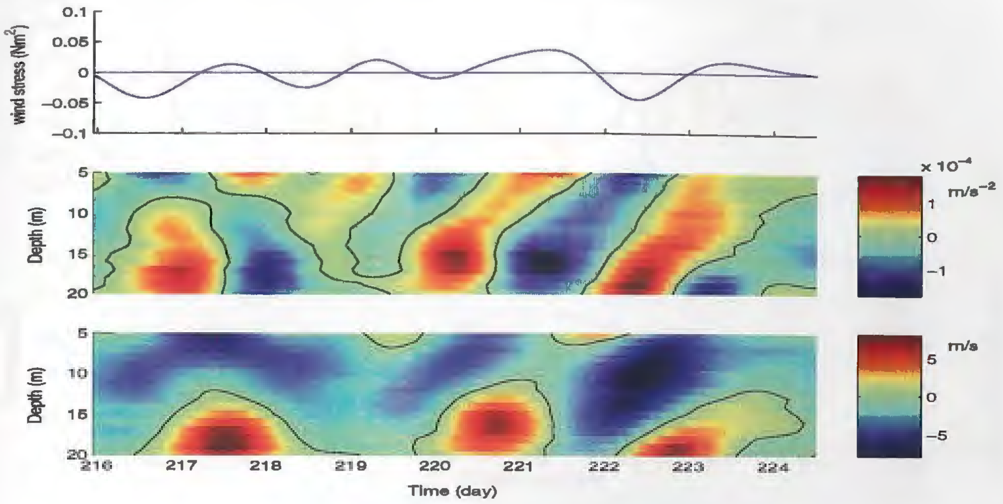

Figure 3.22: Time series of wind stress (top), acceleration of current velocity (middle) and current velocity (bottom) at N3 mooring in 2000. (+) denotes outflow, (-) denotes inflow. The solid line denotes 0 isoline.

term wind force on this area can generate coastal disturbance that may propagate along the west coast of the Island in the forms of free waves (Noble and Butman 1979; Greatbatch and Otterson, 1991), such as Kelvin waves. If the waves propagate past the mouth of the Harbor, it can certainly influence the flow inside the Narrows. This influence can be considered as the remote wind effect (Chapter 1.2). In order to study this remote effect of the wind, we first tried to find out the relationship between the wind and the flow outside the harbor at H2.

EOF analysis is applied to the observation South-North (S-N) current velocity at H2. The result shows that almost 60% of the total variance contributes to the first mode which is statistically significant, Figure 3.26, and the second mode only contributes 20% of the total variance. Due to the lack of data above 20 m depth, plot a in Figure 3.26 shows no strong stratification feature, but from the trend of the line we can still figure

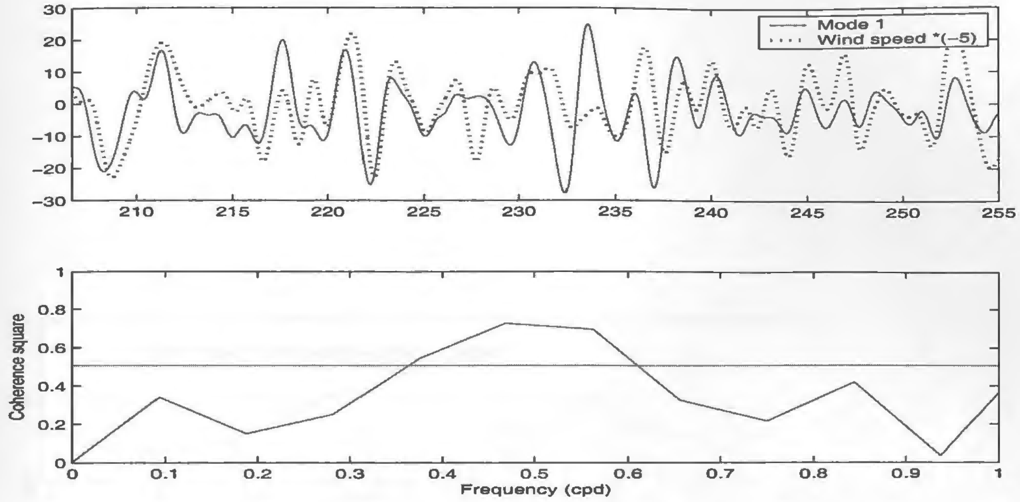

Figure 3.23: Time series of principal components of EOF Mode 1 and wind speed (top), and coherence between them (bottom). (+) denotes outflow, (-) denotes inflow. The straight line denotes 95% confidence limit.

out a two-layer structure in mode 1 with the upper layer above 20 m depth. As wind influence usually focuses on the upper layer in the ocean, so only current data at 20 m depth is chosen here to study its relationship with wind.

Figure 3.27 show the comparison between wind speed and the subtidal current velocity in S-N direction at 20 m depth of H2 mooring. In the figure, we can see the two lines match well, and the value of coherence square keeps above 0.7 between 0.2-0.6 cpd which indicates the two variables significantly cohere with each other. This indicates that the wind forced coastal current dominates the subtidal motions outside the harbor.

Coherence square between current velocity of moorings inside and outside the harbor is calculated. Figure 3.28 shows coherence square between current velocity of N2-N4 and the moorings outside the harbor(H2 at 20 m depth). In the figure, coher-

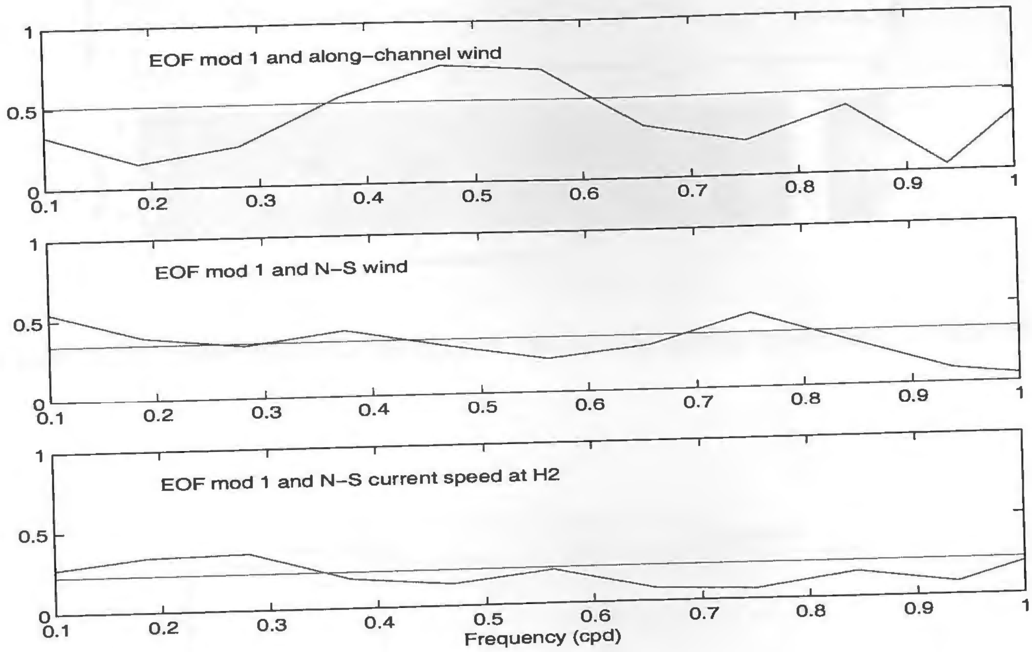

Figure 3.24: Comparison between coherence suqare of EOF mode 1 with along-channel wind speed, N-S wind and N-S current speed at H2 mooring. The straight line denotes 95% confidence limit.

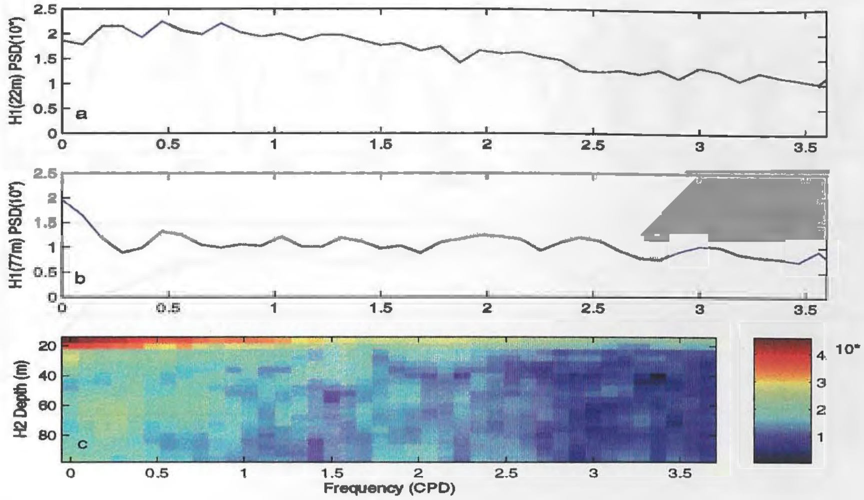

Figure 3.25: Power Spectral Density of the outside harbor moorings, H1 and H2

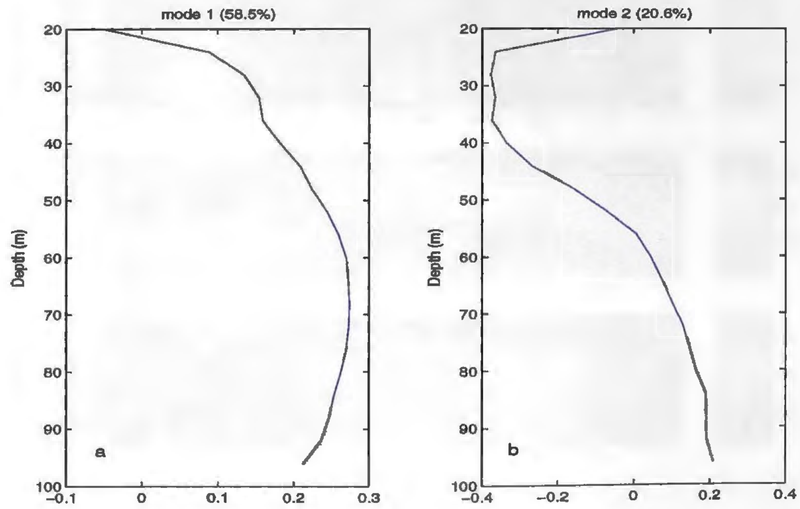

Figure 3.26: EOF result of S-N current velocity at H2 mooring

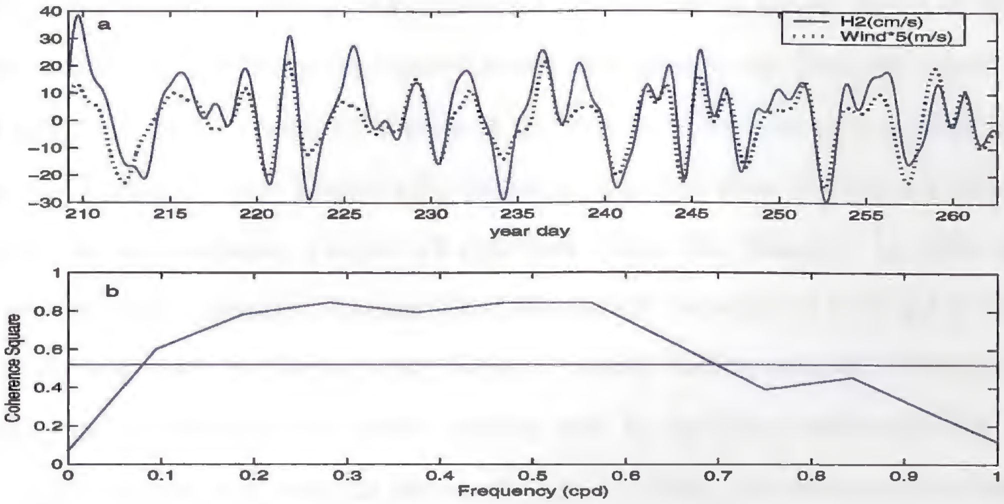

Figure 3.27: Comparison between time series of wind speed and subtidal current velocity at H2 mooring in South-North direction. The straight line denotes 95% confidence limit.

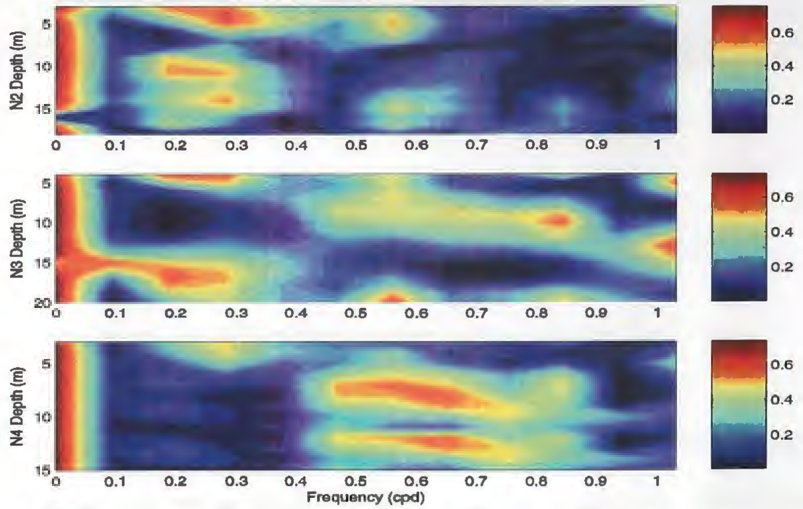

Figure 3.28: Coherence square between moorings inside the harbor and outside the harbor at H2 (20m).

ence square has peak value (> 0.8) below 0.1 cpd almost at all the depth of N2-N4, which means the low frequency signals inside and outside the Narrows cohere with each other very well. As the PSD peak of the current in the Narrows appears at low frequency (below 0.2 cpd, Figure 3.9), therefore, influence from outside is a dominate force to the low frequency (below 0.2 cpd) flow inside the Narrows. In order to see this influence more clearly, a lowpass filter with cutoff frequency of 0.25 cpd is applied to the current data. In Figure 3.29, the zero velocity isoline near the bottom at N3 mooring also matches the N-S current velocity well. In the figure, we can see that when the outside current is flowing to the south (day 235-238), the inflow in the Narrows becomes stronger, the outflow in the bottom layer is damped by the inflow, and this change enhances the outflow in the surface layer.

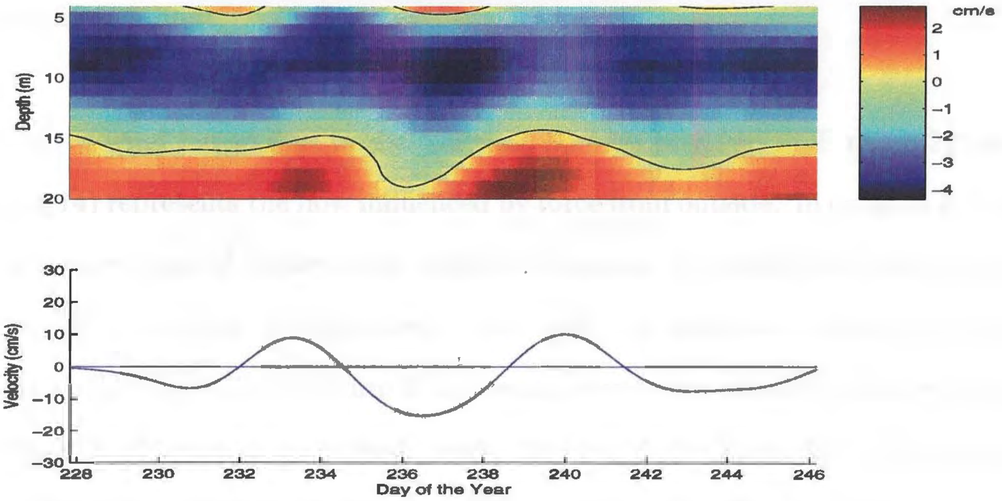

Figure 3.29: Time series of along channel current velocity at N3 mooring (top) and N-S current velocity at 20 m depth at H2 mooring (bottom). The solid line in top graph denotes 0 isoline.

Looking back at Figure 3.14, as we have proved that mode 1 represents the vertical

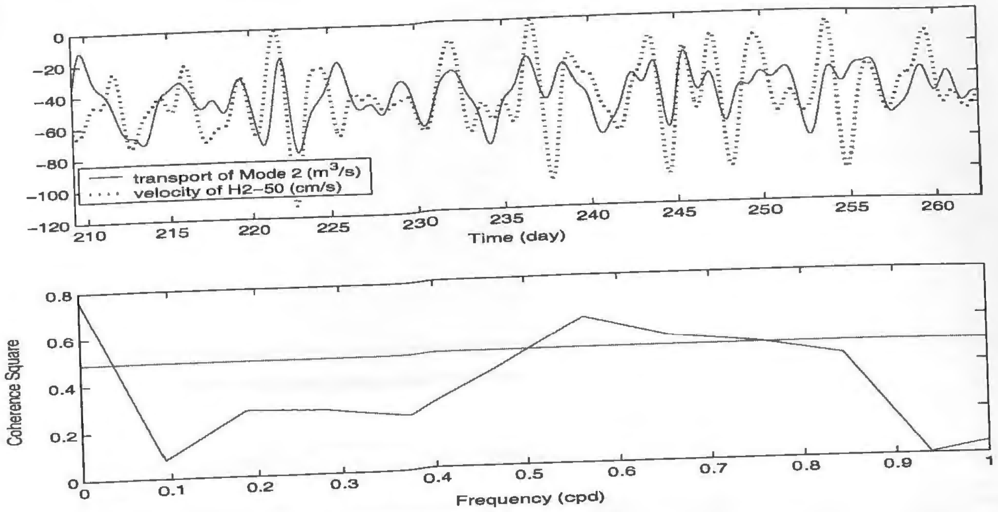

Figure 3.30: Comparison between uplayer transport of EOF mode 2 in the Narrows and the current velocity at H2 (20m depth) outside the Harbor. The straight line is 95% confidence limit.

structure of wind forced flow in the Narrows, here we presume EOF mode 2 (plot b in Figure 3.14) represents the flow influenced by force from outside. In order to prove this, the coherence squared between the estimate transport of mode 2 and current velocity of N2 in S-N direction is calculated. Here only the transport above 12m depth is computed. The reason is in Figure 3.14, the negative value, which dominates the whole the structure of mode 2, is centered above 12m depth. In Figure 3.30, by subtracting a constant value, the current velocity of H2 matches the estimate transport of mode 2 matches very well, and the coherence square between them has a peak between 0.5 and 0.6 cpd which also correlates with the result of coherence square between current velocity at H2 and in the Narrows (Figure 3.28).

In order to study the relationship between EOF mode 2 with other forces, the coherence squares of EOF mode 2 with along channel and N-S wind are also calculated.

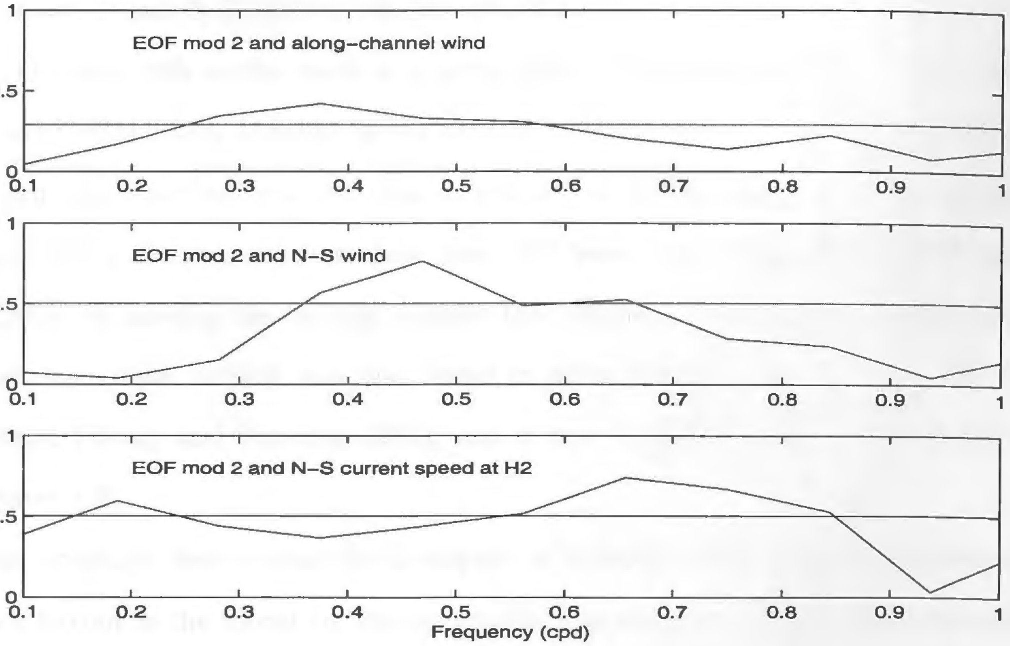

Figure 3.31: Coherence between the principle component of EOF mode 2 and along channel wind velocity, N-S wind velocity and N-S current velocity at H2 mooring. The straight line denotes 95% confidence limit.

In Figure 3.31, the result shows that coherence between EOF mode 2 and along channel wind velocity is very weak, mostly below 0.5, and this indicates that the two variables has almost no relations between each other, which also means that local along channel wind stress in the harbor almost has no contribution to mode 2. The coherence between EOF mode 2 and N-S wind has a peak at around 0.5 cpd, while the coherence between EOF mode 2 and N-S current velocity at H2 mooring also has a peak at around 0.5 cpd. The high cliffs on the north and south sides of the Narrows (Figure 2.1) blocks the N-S wind stress from influencing the current in the Narrows. Therefore, considering the high coherence between N-S current velocity at H2 mooring and N-S wind velocity (Figure 3.27), we can conclude here that N-S wind contributes to the EOF mode 2 indirectly by driving the current outside the Narrows. This indirect wind effect on estuarine subtidal current was also found in other estuarine areas, such as Delaware estuarine (Wong and Garvine, 1984), and it can be defined as a remote wind effect (Chapter 1.3).

We conclude here is that the transport of subtidal current in the Narrows of St. John's harbor is the forced by the combination of local wind stress and external flow flux,

$$T \cong T_{mod1} + T_{mod2} = \sum T_{Wind} + \sum T_{External flux}, \tag{3.26}$$

where, T denotes the transport.

3.2.3 Mean Flow and Estuarine Circulation in the Narrows

As the previous section (3.2.2) shows, the current in the Narrows has a two-layer structure with the water in the surface layer flowing out of the harbor and in the lower layer flowing inside. In order to study the vertical structure of the mean velocity in the channel, horizontal averaged along channel current velocity in each depth of the Narrows is calculated from the observation data for 2000. There are three layers in Figure 3.32. Outflow exists not only in the surface layer but also in the bottom layer, and inflow dominates the middle layer. From the figure, the largest mean inflow appears at the middle depth, around 8 m depth, and the largest mean outflow should appear at the surface, but due to the lack of surface current data (above 3 m depth), it is hard to estimate its value.

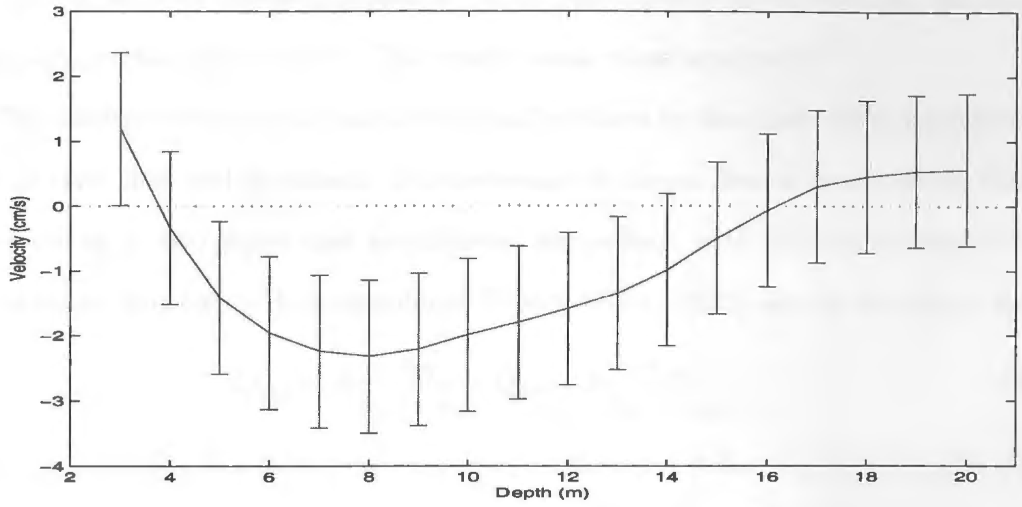

Figure 3.32: Horizontal averaged along channel current velocity at each depth in the Narrows. The size of the vertical bars is equal to one standard deviation in the mean velocity field.

With the same interpolation method used in Chapter 3.2.1, the mean transport of outflow and inflow in the Narrows can be calculated from the observation data in 2000. In Table 3.2, the transport of inflow is about twice of that of outflow, which means every second the volume of water in the harbor will increase about $20m^3$. It is clear that the outflow transport is greatly underestimated due to the lack of surface

Table 3.2: Mean Velocity and Transport of Inflow and Outflow

Title	Velocity (cm/s)	Tranport (m^3s^{-1})
Inflow	-1.31	-47.51
Outflow	1.21	21.05

current data. In order to correct this, we use a simple linear extrapolation to estimate the current velocity above 3 m depth. After this correction calculation, the outflow transport reaches 47.51 m^3s^{-1}. This result seems more acceptable.

The outflow in estuarine channels is usually driven by the fresh water from the land such as river flow and snowmelt. If considering the mean flow in an estuarine channel as occurring in two layers and no diffusion happening, with the conservation of salt and volume, Knudsen's Hydrographical Theory (Dyer, 1973) can be developed as:

$$Q_{out} = R\frac{s_{in}}{s_{in} - s_{out}}, Q_{in} = R\frac{s_{out}}{s_{in} - s_{out}}. \tag{3.27}$$

Here, Q_{out} and Q_{in} denote the transports of outflow and inflow, s_{in} and s_{out} denote the salinity in the two layers, and R is the river discharge. Therefore, if the river flux and salinity are known, we can estimate the transport of outflow and inflow using Equation 3.27. Although the vertical structure of the mean flow in the Narrows does not show a two-layer system, Knudsen's theory can still be applied here if we ignore the bottom outflow here since it is very weak compared with the interpolated outflow in the surface layer.

The monthly data of river flow of Waterford River in St. John's harbor in year 2000 was obtained from Environment Canada (www.ec.gc.ca), and the sewage water flux from St. John's city is neglected here because of the lack of data. To simplify the comparison process, only observations from August are used here. Due to the lack of salinity data in 2000, salinity data in November of year 1999 is used to replace it. The salinity profile in the estuary area is mainly generated by the surface fresh water flux from the land. So before using the salinity data in 1999, comparison between river flux in the two months of different years is done firstly. The result shows no significant difference, so we expect this replacement of salinity data could be reliable.

Firstly, mean velocity of inflow and outflow in August of 2000 is calculated from the observation current data by adding the estimate current data above 3 m depth. Then using Equation 3.27, with $R = 0.913m^3s^{-1}$, $S_{in} = 30.80$ psu and $S_{out} = 29.4$ psu, we can get an estimation of transport of inflow and outflow. From the transport estimation, mean velocity of inflow and outflow in the Narrows can also be calculated. In Table 3.3, we can see the mean velocity calculated from Knudsen's theory matches the observation data well despite the uncertainties in the assumptions and calculations. This result shows that although not exactly two-layer flow occurs in the Narrows, Knudsen's hydrographical theory can still be applied here. And also this result proves that outflow flux in the Narrows can be explained by the freshwater flux from the land no mater it in the surface layer or the bottom layer.

Table 3.3: Comparison between Mean Velocity from Observation data and from Knuden's Theory

Title	Outflow (cm/s)	Inflow (cm/s)
Observation	2.23	-1.2
Knudsen's Theory	2.47	-1.26

3.3 Summary

From the analysis of the observation data in 1999 and 2000 above, we can get the conclusions as:

- Semi-diurnal tidal components, M2 and S2, dominating the tidal current in the harbor, and in the Narrows the tides having a barolinic feature, with amplitude peak occurring in the center of upper layer (above 5m) and lower layer (at roughly 12m).

- Power spectral density of the observation data showing that the most energetic section focus on the low frequency (< 0.5 cpd).

- Comparison between subtidal current and wind speed showing that wind stress influences the surface current and has counter influence on the current in the lower layer, the computation of the transport in the Narrows also proving this feature.

- EOF analysis of the subtidal current in the Narrows showing more than 70% of the total variance contributes to the first two modes, with both modes showing a two-layer vertical structure.

- Comparison between EOF modes, wind stress and observation current inside and outside the harbor indicating EOF mode 1 representing the wind influence in the Narrows and mode 2 representing the influence of external force from outside the harbor.

- Mean velocity of outflow and inflow calculated from Knudsen's Hydrographical Theory matches well with the observation data and this indicating fresh water from the land dominates the water flux in the Narrows of the harbor.

Chapter 4

Numerical Model and Its Result

As the data analysis in 3 has demonstrated, the vertical structure of the current inside the Narrows can be described as a typical two-layer circulation system, with the water in the first layer flowing out of the harbor, and in the second layer flowing inside the harbor. Therefore, a two-layer ocean model is used here to simulate the circulation system inside the Narrows.

In this Chapter, a two-layer model is introduced in the first section; then the boundary conditions and step scheme are described in the second part; the result of the model and comparison with the observation data is discussed in the third part.

4.1 Introduction of a 2D Two Layer Ocean Model

4.1.1 The General Multi-Layer Model

O'Brien and Hurlburt (1972) set up a general coastal multi-layer model to study the coastal upwelling problem. In their model, only west-east variations are considered and there is no bottom topography. In this thesis, this model is extended by adding north-south variations and bottom topography.

Consider a stably stratified incompressible fluid on a coastal area with constant depth, suppose the fluid consists of incompressible layers which have initial thickness h_j and densities ρ_j, j denoting the number of the layer, $j = 1$ at the surface. In order to simplify the problem, diffusion is omitted as $\frac{\partial^2(u,v)}{\partial(x,y)^2}$ is very small as will be explained in the non-dimensional analysis later. The appropriate coordinate system is the vertical Cartesian coordinated system with x increasing eastward and z upward. The rigid lid assumption and Boussinesq approximation is applied. Here, we are particularly interested in the vertically averaged velocity within each layer. If the pertinent hydrodynamic equations of motion are integrated vertically over the depth of each layer and the vertically averaged horizontal velocity components u_j, v_j are assumed independent of depth within each layer (O'Brien and Hurlburt, 1972), the normal mode of the multi-layer ocean model can be obtained as,

$$\frac{\partial u_j}{\partial t} + u_j\frac{\partial u_j}{\partial x} + v_j\frac{\partial u_j}{\partial y} + P_j = fv_j + [(\tau_j^{Tx} - \tau_j^{Bx})/(\rho h_j)], \tag{4.1}$$

$$\frac{\partial v_j}{\partial t} + u_j\frac{\partial v_j}{\partial x} + v_j\frac{\partial v_j}{\partial y} + P_j = -fu_j + [(\tau_j^{Ty} - \tau_j^{By})/(\rho h_j)], \tag{4.2}$$

$$\frac{\partial h_j}{\partial t} + \frac{\partial h_j u_j}{\partial x} + \frac{\partial h_j v_j}{\partial y} = 0, \tag{4.3}$$

where τ_j^T and τ_j^B are the stresses at the top and bottom of each layer. When $j = 1$, τ_1^T is wind stresses at the sea surface; when $j > 1$, τ_j^T is the interfacial stress between the layers. They will be specified as function of x, y and t. The vertical velocity is implicit in (4.3) and can be obtained from the h_j, u_j and v_j posteriorly. Both barotropic and baroclinic modes have been retained here as both modes have been proved important in the former chapters.

P_j in euqations (4.2) and (4.2) is the horizontal gradient of the pressure integral on z for the layer. Here we use the x direction as a example for calculate P_j, and the term of y direction can be found similarly. From the hydrostatic assumption, the pressure p_j at any point inside a layer j can be given by (O'Brien and Hurlburt, 1972)

$$\begin{aligned}
p_1 &= P_a + \rho_1 g[\sum_{i=0}^{m-1} h_{m-i} + D(x) - z], \\
p_2 &= P_a + \rho_1 g h_1 + \rho_2 g[\sum_{i=0}^{m-2} h_{m-i} + D(x) - z], \\
&\vdots \\
p_j &= P_a + \sum_{i=1}^{j-1} \rho_i g h_i + \rho_j g[\sum_{i=0}^{m-j} h_{m-i} + D(x) - z],
\end{aligned} \tag{4.4}$$

where m is the number of discrete layers, P_a is the pressure of the atmosphere, and Dx is the elevation of the bottom above the reference level $z = 0$. Then integrating these over the appropriate layer, P_j can be found as

$$\begin{aligned}
P_j &= \frac{1}{h_j \rho_j} \frac{\partial}{\partial x} \int_B^T p_k dz \\
&= \frac{1}{\rho_j} \sum_{i=1}^{j-1} \rho_i g \frac{\partial h_i}{\partial x} + g[\sum_{i=0}^{m-j} \frac{\partial h_{m-i}}{\partial x} + \frac{\partial D}{\partial x}] + \frac{g}{\rho_k h_k} \frac{\partial}{\partial x} \int_B^T zdz.
\end{aligned} \tag{4.5}$$

In eq. 4.5, if the bottom topography has horizontal variance, which means $\partial h/(\partial(x, y)) \neq 0$, the vertical integrating term, $(\partial/(\partial x)) \int_B^T zdz$ can not be neglected.

Thus, for an appropriate specification of the wind stress, a functional form of the interior stresses, and valid initial and boundary conditions, the formal eqs. 4.1-4.3 will be solved.

4.1.2 The Two-Layer Model

Applying the multi-layer model (4.1-4.3) to a two-layer ocean system and replacing the friction force with a linear term, a two-layer model can be set up as,

$$\frac{\partial u_1}{\partial t}+u_1\frac{\partial u_1}{\partial x}+v_1\frac{\partial u_1}{\partial y} = -g\frac{\partial(h_1+h_2+D)}{\partial x}+fv_1+\frac{\tau_1^{Sx}}{\rho h_1}-F_1^{Ix}, \tag{4.6}$$

$$\frac{\partial v_1}{\partial t}+u_1\frac{\partial v_1}{\partial x}+v_1\frac{\partial v_1}{\partial y} = -g\frac{\partial(h_1+h_2+D)}{\partial y}-fu_1+\frac{\tau_1^{Sy}}{\rho h_1}-F_1^{Iy}, \tag{4.7}$$

$$\frac{\partial h_1}{\partial t}+\frac{\partial h_1 u_1}{\partial x}+\frac{\partial h_1 v_1}{\partial y} = 0, \tag{4.8}$$

$$\begin{aligned}\frac{\partial u_2}{\partial t}+u_2\frac{\partial u_2}{\partial x}+v_2\frac{\partial u_2}{\partial y} &= -g\frac{\partial(h_1+h_2+D)}{\partial x}+g'\frac{\partial h_1}{\partial x}+fv_2\\ &+ F_2^{Ix}-F_2^{Bx},\end{aligned} \tag{4.9}$$

$$\begin{aligned}\frac{\partial v_2}{\partial t}+u_2\frac{\partial v_2}{\partial x}+v_2\frac{\partial v_2}{\partial y} &= -g\frac{\partial(h_1+h_2+D)}{\partial y}+g'\frac{\partial h_1}{\partial y}-fu_2\\ &+ F_2^{Iy}-F_2^{By},\end{aligned} \tag{4.10}$$

$$\frac{\partial h_2}{\partial t}+\frac{\partial h_2 u_2}{\partial x}+\frac{\partial h_2 v_2}{\partial y} = 0. \tag{4.11}$$

The geometry of the model is indicated in Figure 4.1. The velocity u_i and v_i denote the depth-averaged velocity for each layer. The subscript 1 refers to the upper layer and 2 to the lower layer. In eq. 4.6-4.11, we can see the two layers are dynamically coupled through pressure gradient and interfacial stress. Here g' is the reduced gravity acceleration as

$$g' = g(\rho_2-\rho_1)/\rho_2 \tag{4.12}$$

τ^S is the wind stress, calculated from the observation data using the method of Large and Pond (1981) as following,

$$\tau = \rho_a C_D|\vec{U_w}|\vec{U_w}, \tag{4.13}$$

where

$$C_D = \begin{cases} 1.2\times10^{-3} & |\vec{U_w}|<11m/s\\ (0.49+0.065\times|\vec{U_w}|)\times10^{-3} & |\vec{U_w}|\geq 11m/s\end{cases}$$

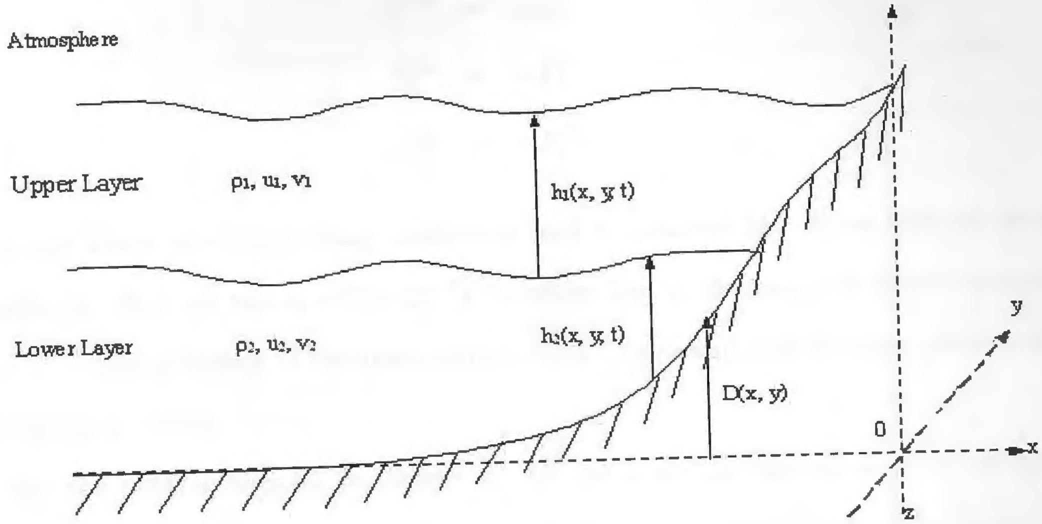

Figure 4.1: Typical geometry for a two-layer model with a free surface and one interface. The bottom topography is $D(x)$, and h_1 and h_2 are the thicknesses of each layer of density ρ_1 and ρ_2. The velocity are depth-averaged.

F^I adn F^B is assumed to depend on the horizontal relative current velocity linearly,

$$\begin{aligned} F_1^{Ix} &= c_1(u_1 - u_2) \\ F_1^{Iy} &= c_1(v_1 - v_2) \\ F^{Bx} &= c_2 u_2 \\ F^{By} &= c_2 v_2 \\ F_2^{Ix} &= -F_1^{Ix} \\ F_2^{Iy} &= -F_1^{Iy} \end{aligned} \tag{4.14}$$

c_1 is the linear interfacial drag coefficient and c_2 denotes the linear bottom friction coefficient. Here we use $c_1 = 2 \times 10^{-6} s^{-1}$, which lies in the range of values commonly used in ocean modeling of the near-surface layer (Neumann and Pierson, 1966; Rubino and Hessner, 2002).

For the bottom friction coefficient c_2, we use a simple case of decaying of inertia current under the effect of friction to estimate it's value in the Narrows (Neumann and Pierson, 1966). Considering the linearized shallow water equation,

$$\frac{du}{dt} = fv - \frac{1}{\rho}\frac{\partial p}{\partial x} - \frac{c_2}{h}u, \tag{4.15}$$

$$\frac{dv}{dt} = -fu - \frac{1}{\rho}\frac{\partial p}{\partial y} - \frac{c_2}{h}v. \tag{4.16}$$

Here h is the depth of the ocean. Multiply euqation (4.14) with u and euqation (4.15) with v, add the two equations and we get

$$u\frac{du}{dt} + v\frac{dv}{dt} = -\frac{1}{\rho}(u\frac{\partial p}{\partial x} + v\frac{\partial p}{\partial y}) - \frac{c_2}{h}(u^2 + v^2). \tag{4.17}$$

If we define $U = u^2 + v^2$, euqation (4.16) can be written in the form

$$\frac{1}{2}\frac{dU^2}{dt} = -\frac{1}{\rho}(u\frac{\partial p}{\partial x} + v\frac{\partial p}{\partial y}) - \frac{c_2}{h}U^2 \tag{4.18}$$

Assume the horizontal pressure gradient suddenly disappears for some reason, then, euqation (4.17) becomes

$$\frac{1}{U}\frac{dU}{dt} = -\frac{c_2}{h} \tag{4.19}$$

The solution of eq. 4.18 with the initial condition that $U = U_0$ at $t = 0$ is

$$U = U_0 e^{-(c_2/h)t} \tag{4.20}$$

From euqation (4.19), it is seen that the inertia velocity decreases exponentially with time, and the rate of decrease depends on the value of c_2/h. Therefore, if the initial velocity U_0 and damped velocity U are known, the amplitude of c_2 can be estimated with euqation (4.19) approximately,

$$c_2 = -\frac{h}{t} ln(U/U_0) \tag{4.21}$$

Inertia current velocity can be computed from the bottom observation velocity of the three moorings (N1-N5 moorings) in the Narrows. Then by setting the depth $h = 20$ m, from euqation (4.20), the averaged calculation values of bottom friction coefficient c_2 in the Narrows equals approximately $1 \times 2^{-4} ms^{-1}$. This value falls in the value range of bottom friction coefficient commonly used in ocean modeling (Neumann and Pierson, 1966). In order to compare the result of model with the observations, the model domain keeps consistent with the observation area (Figure 1.2). But in the model, linear bottom friction parameter is used (equation (4.14)), the depth $h = 20$ m should be divided by this value. Therefore, we can get the parameters of the model domain. Table 4.1 shows the parameters used in the model.

4.1.3 Non-dimensional Model

As we know, ocean motion is very complicated and affected by many factors, such as salinity, temperature, viscosity and outer forces, but for a particular areas, there can be

Table 4.1: Parameters Used in the Model

f (Coriolis parameter)	$10^{-4}s^{-1}$
g (gravity acceleration)	$9.81ms^{-2}$
g'(reduced gravity acceleration)	$6 \times 10^{-3}ms^{-2}$
ρ (water density)	$1028Kgm^{-3}$
c_1 (interfacial drag coefficient)	$2 \times 10^{-6}s^{-1}$
c_2 (bottom drag coefficient)	$1 \times 10^{-5}s^{-1}$

some predominant forces to dominate main water motions there. Therefore, when using models to study the ocean dynamics of a specified location, it is important to decide the important factors there, as this can not only simplify the model by neglecting the 'minor' terms but also explain the dynamics of the motions more accurately. Usually, non-dimensional analysis, also called scaling analysis, is used.

For the model set up with euqations (4.6) - (4.11), considering the continuity equations and some variables having the same scale, the scaling parameters can be defined as,

$$\begin{aligned}
(u_i, v_i) &= Ui(u_i', v_i') \\
(x, y) &= L(x', y') \\
t &= Tt' = \frac{L}{U}t' \\
h_i &= H_i h_i' \\
\frac{\partial h_1}{\partial(x,y)} &= \frac{\eta_1}{L}\frac{\partial h_1'}{\partial(x',y')} \\
\frac{\partial(h_1+h_2+D)}{\partial(x,y)} &= \frac{\eta}{L}\frac{\partial(h_1'+h_2')}{\partial(x',y')} \\
(\tau^{Sx}, \tau^{Sy}) &= \tau(\tau^{Sx'}, \tau^{Sy'})
\end{aligned} \tag{4.22}$$

In order to simplify the deducing process, flat bottom topography is assumed here. The scaling parameters of the horizontal velocity (u_i, v_i) are supposed to be the same, U. η denotes the mean departure of the free surface from the rest height, and η_1 denotes the mean departure of the interfacial surface from the rest height.

Replacing variables in euqations (4.60 - (4.11) with euqation (4.23), the scaled momentum equations for the two-layer model are

$$\begin{aligned}
\frac{U_1^2}{L}\frac{\partial u_1'}{\partial t'} + \frac{U_1^2}{L}u_1'\frac{\partial u_1'}{\partial x'} + \frac{U_1^2}{L}v_1'\frac{\partial u_1'}{\partial y'} &= -g\frac{\eta}{L}\frac{\partial(h_1'+h_2')}{\partial x'} + fU_1v_1' + \frac{\tau}{\rho H_1}\frac{\tau^{x'}}{\rho h_1'}, && (4.23)\\
\frac{U_1^2}{L}\frac{\partial v_1'}{\partial t'} + \frac{U_1^2}{L}u_1'\frac{\partial v_1'}{\partial x'} + \frac{U_1^2}{L}v_1'\frac{\partial v_1'}{\partial y'} &= -g\frac{\eta}{L}\frac{\partial(h_1'+h_2')}{\partial y'} - fU_1u_1' + \frac{\tau}{\rho H_1}\frac{\tau^{y'}}{\rho h_1'}, && (4.24)\\
\frac{U_2^2}{L}\frac{\partial v_2'}{\partial t'} + \frac{U_2^2}{L}u_2'\frac{\partial u_2'}{\partial x'} + \frac{U_2^2}{L}v_2'\frac{\partial u_2'}{\partial y'} &= -g\frac{\eta}{L}\frac{\partial(h_1'+h_2')}{\partial x'} \\
&+ g'\frac{\eta_1}{L}\frac{\partial h_1'}{\partial x'} + fU_2v_2', && (4.25)\\
\frac{U_2^2}{L}\frac{\partial v_2'}{\partial t'} + \frac{U_2^2}{L}u_2'\frac{\partial v_2'}{\partial x'} + \frac{U_2^2}{L}v_2'\frac{\partial v_2'}{\partial y'} &= -g\frac{\eta}{L}\frac{\partial(h_1'+h_2')}{\partial y'} \\
&+ g'\frac{\eta_1}{L}\frac{\partial h_1'}{\partial y'} - fU_2u_2'. && (4.26)
\end{aligned}$$

Here, the interior and bottom stress terms are omitted as they are quite small, $O(10^{-4})$ or less. Then divide fU on both sides of euqation (4.26), the non-scale equations become

$$\begin{aligned}
R_1(\frac{\partial u_1'}{\partial t'} + u_1'\frac{\partial u_1'}{\partial x'} + v_1'\frac{\partial u_1'}{\partial y'}) &= -\frac{R_1}{Fr_{E1}}\frac{\partial(h_1'+h_2')}{\partial x'} + v_1' + Ed\frac{\tau^{x'}}{\rho h_1'}, && (4.27)\\
R_1(\frac{\partial v_1'}{\partial t'} + u_1'\frac{\partial v_1'}{\partial x'} + v_1'\frac{\partial v_1'}{\partial y'}) &= -\frac{R_1}{Fr_{E1}}\frac{\partial(h_1'+h_2')}{\partial y'} - u_1' + Ed\frac{\tau^{y'}}{\rho h_1'}, && (4.28)\\
R_2(\frac{\partial v_2'}{\partial t'} + u_2'\frac{\partial u_2'}{\partial x'} + v_2'\frac{\partial u_2'}{\partial y'}) &= -\frac{R_2}{Fr_{E2}}\frac{\partial(h_1'+h_2')}{\partial x'} + \frac{R_2}{Fr_{I1}}\frac{\partial h_1'}{\partial x'} + v_2', && (4.29)\\
R_2(\frac{\partial v_2'}{\partial t'} + u_2'\frac{\partial v_2'}{\partial x'} + v_2'\frac{\partial v_2'}{\partial y'}) &= -\frac{R_2}{Fr_{E2}}\frac{\partial(h_1'+h_2')}{\partial y'} + \frac{R_2}{Fr_{I1}}\frac{\partial h_1'}{\partial y'} - u_2'. && (4.30)
\end{aligned}$$

Here, R_i denotes Rossby number, Fr_{Ei} and Fr_{Ii} are external and internal Froude number, Ed is Ekman drift. The definition of the non-dimensional numbers are as following,

$$\begin{aligned} R_i &= Ui/(fL) \quad \textit{Rossby number} \\ Fr_{Ei} &= Ui^2/(g\eta) \quad \textit{external Froude number} \\ Fr_{Ii} &= Ui^2/(g'\eta_i) \quad \textit{internal Froude number} \\ Ed &= \tau/(\rho f U H_1) \quad \textit{Ekman drift} \end{aligned}$$

As the model domain is defined by the harbor area, the horizontal scale L is order 10 km, and from the observation results, we set the horizontal velocities in both layers are order 10 cm/sec. Then, we can get Rossby number, $R_1 \leq 1$, while in the Narrows where as $L < 1$ km, $R_1 = 1$, which means the horizontal non-linear terms are important and cannot be omitted here. Observation result decides that inside the Narrows some parameters has the order as, $H_1 = 5$ m, $H_2 = 15$ m, $\tau = 10^{-2}$. Keeping the balance on both sides of euqation (4.30), the relationship of the none dimensional numbers can be obtained as,

$$R_1 + R_1/Fr_{E1} = 1 + Ed \tag{4.31}$$

$$R_2 + R_2/Fr_{E2} - R_2/Fr_{I1} = 1. \tag{4.32}$$

Putting the order of H_1, H_2 and τ into euqation (4.32), we can get the order of η as 10^{-2} m and the order of η_1 as 2×10^{-3} m. Considering the area outside the Narrows, as the Rossby number $R_i << 1$, the horizontal non-linear terms can be omitted. This yields the geostrophic balance,

$$R_1/Fr_{E1} = 1 \tag{4.33}$$

$$R_2/Fr_{E2} - R_2/Fr_{I1} = 1. \tag{4.34}$$

We obtain the order of η_1 as 10^{-2} m and the order of η as 2×10^{-2} m. Also, the time scale of the model, $T = L/U$, is order roughly 1 day.

4.2 Step Scheme and Boundary Conditions Of the Model

4.2.1 Spatial and Time Step Scheme

As the model is two-dimensional and horizontal, a traditional, second-order finite-difference approximation is adopted. Therefore, the well known staggered grid, Arakawa "C" grid, is used here as it better represents the phase speed and group velocity of the waves, Fig. 4.2.

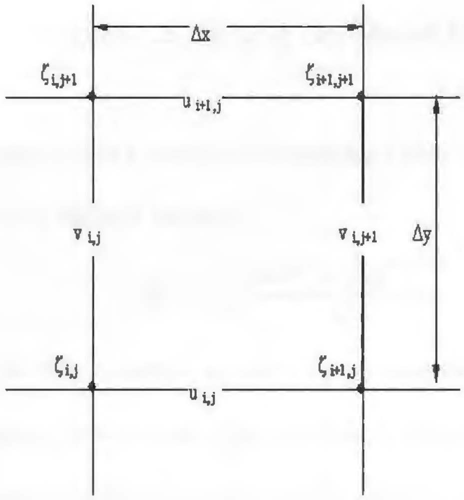

Figure 4.2: Placement of variables on an Arakawa C grid.

As the object of the model is to study the dynamical features in the harbor and to compare that with the observation result, it is convenient to set the resolution of the model the same as that of the observation inside the Narrows. Therefore, the spatial step in both directions (latitude and longitude) of the model is set 0.0005^o, $\Delta x = 37.5$

m and $\Delta y = 55.5$ m, which provides 5 grid points inside the Narrowss, the same as the observations. Figure 4.3 shows the grid of the model domain. Considering the spatial grid used here, to satisfy the Courant-Friedrichs-Levy (CFL) computational stability condition, the time step should satisfy,

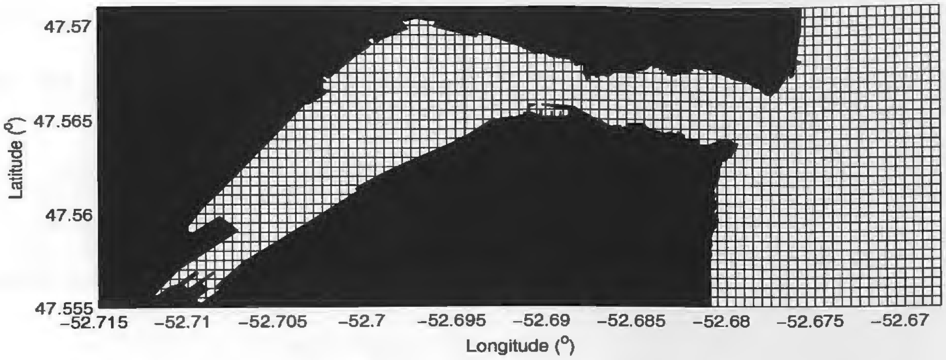

Figure 4.3: Grid of the Model Domain.

$$\Delta t \leq \frac{1}{2}\frac{(\Delta x^2 + \Delta y^2)^{1/2}}{C}. \tag{4.35}$$

Here, $C = (gH)^{1/2}$. As the external gravity (g) waves exists in the model solution, and also with the fine spatial resolution (Δx and Δy) and $H = O(10\text{ m})$, the timestep to satisfy CFL conditions is limited to very small, $\Delta t \leq 1.5$ s. After trying several values, Δt is set 0.9 s.

According to the spatial grid used in the model, the forward spatial differencing is applied here,

$$\begin{aligned}\frac{\partial \phi^j_{m,n}}{\partial x} &= \frac{\phi^j_{m+1,n} - \phi^j_{m,n}}{\Delta x},\\ \frac{\partial \phi^j_{m,n}}{\partial y} &= \frac{\phi^j_{m,n+1} - \phi^j_{m,n}}{\Delta y}.\end{aligned}$$

Here ϕ denotes the differencing variable, j is the number of time step, and (m, n) is the number of spatial step.

Leapfrog-trapezoidal (LT) scheme is used for the numerical timestepping. Here, we only use euqation (4.6) to show the process of LT scheme. To simplify the deriving process, move all the non-time terms on the left side of euqation (4.6) to the right, and consider the whole right side as a function, $\Phi(t)$. Then euqation (4.6) becomes,

$$\frac{\partial u}{\partial t} = \Phi(t).$$

The leapfrog timestep is,

$$\frac{u(t+\Delta t) - u(t-\Delta t)}{2\Delta t} = \Phi(t). \tag{4.36}$$

This timestep has a second accurate order, but it is unconditionally unstable with respect to diffusion. Also, the even and odd timesteps tend to diverge in a computational mode. In order to damp this computational mode, a correction step is taken here. First, introduce u' here,

$$u'(t+\Delta t) = u(t-\Delta t) + 2\Delta t\Phi(t). \tag{4.37}$$

Then an initial guess of $\Phi(t+\Delta t)$ can be got from u', $\Phi'(t+\Delta t) = \Phi(u')$. The correction step, trapezoidal step, is,

$$u(t+\Delta t) = u(t) + \frac{1}{2}\Delta t\Phi^*(t), \tag{4.38}$$

here,

$$\Phi^*(t) = \frac{1}{2}[\Phi(t) + \Phi'(t+\Delta t) \tag{4.39}$$

This leapfrog-trapezoidal timestep is stable with respect to diffusion and it strongly damps the computational mode, but this is obtained with the expense of more computation as the right-hand-side terms are computed twice every timestep.

4.2.2 Boundary Conditions

As the model domain shows, Figure 4.3, the main object of the model is to study the circulation inside the Narrows, which can be affected by the coastal Kelvin waves propagating from the north of the harbor. If the wave propagates into the Narrows, it will propagate one way in the harbor. Therefore, an appropriate open boundary in this case should allow the waves to propagate into the model domain from the "upstream" boundary (here referring to the north boundary) without generating alot spurious effects to contaminate the solution, and it should also allow the waves exit the model domain from the "downstream" boundary (here referring to the south boundary) with as little reflection as possible back into the domain. Here, a modified radiation condition set up by Greatbatch and Otterson (1991) is used in this thesis. This condition is based on Miller and Thorpe's (1981) radiation condition,

$$\eta_b^{n+1} = \eta_b^n - (\frac{\tilde{c}\Delta t}{\Delta n})(\eta_b^n - \eta_{b-1}^n). \tag{4.40}$$

Here, $\tilde{c}$ is propagation speed normal to the boundary, Δn denoted the spatial step, superscript n denotes time level, b is the boundary grid point, $(b-1)$ is one grid point in from the boundary. $\tilde{c}$ is determined by

$$\hat{c} = \frac{\tilde{c}\Delta t}{\Delta n} = -\frac{\eta_{b-1}^n - \eta_{b-1}^{n-1}}{\eta_{b-1}^{n-1} - \eta_{b-2}^{n-1}}, \tag{4.41}$$

where $(b-2)$ denotes two grid points in from the boundary. If $\hat{c} \leq 0$, indicating wave propagating into the model domain, then $\tilde{c}$ in eq. 4.40 is set equal to zero. Otherwise, when $\hat{c} > 0$, indicating wave propagating outside the model domain, then we set $\tilde{c} = \hat{c}\Delta n/\Delta t$, with the limitation that if $\hat{c} > 1$, then $\tilde{c} = \Delta n/\Delta t$. This boundary condition is applied firstly to a simple shallow water model with the same model domain as Figure 4.3. The result shows that it works reasonably well.

For the coastal boundary conditions, the simple no-slip conditions is used here,

$$U_{//} = 0. \tag{4.42}$$

$U_{//}$ denotes the velocity parallel to the coastal boundary.

4.3 Result

The initial conditions of the model are $u = v = \eta = 0$ everywhere. As presented in chapter 3, wind is the main force to drive the subtidal current inside the model domain, wether local or remote. Therefore, we drive this model with the observed wind data. In this section, the result of wind forcing model is shown firstly, then model result is compared with the observation result.

4.3.1 Result of Model

The analysis results of the observation data in chapter 3 show that the strong wind in the channel not only contributes a lot to the subtidal current in the surface layer but also affects the current in the lower layer. Therefore, in order to study the effect of the wind, the model is forced by observation wind. Wind stress was calculated from observation wind speed using the method of Large and Pond (1981). The model is run with the sudden onset of uniform wind at $t = 0$, and wind stress only changes with time, $\tau = \tau(t)$. The initial conditions are $u = v = \eta = 0$ everywhere.ed from observation wind speed using the method of Large and Pond (1981) as shown in chapter 2.3. The model is running with a sudden turn-on uniform wind at $t = 0$, and wind stress only changes with time, $\tau = \tau(t)$. The initial conditions are $u = v = \eta = 0$ everywhere.

The model is first run for 100 hours. Figure 4.5 shows time series of u in both layers

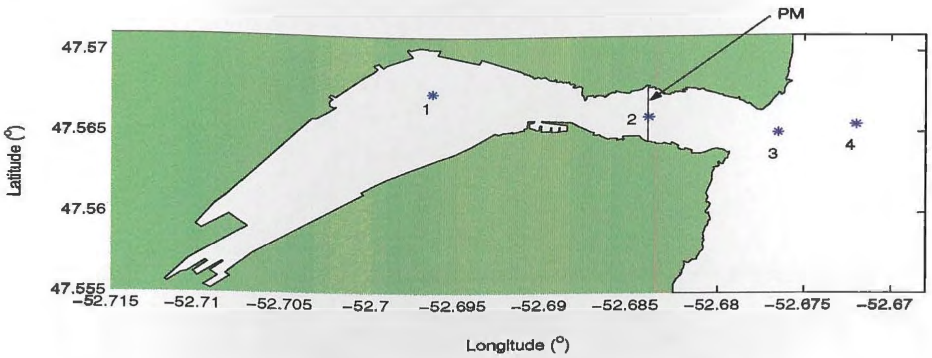

Figure 4.4: 4 monitored grid points in the model domain.

at each of the grid points numbered in Figure 4.4. As the length of model domain is much smaller compared with the external Rossby deformation radius (>170 km here), in Figure 4.5, we can see all the points almost response to the wind force simultaneously and no phase delay can be seen among different grid points. As expected, the model results show that the amplitude of the wind driven flow in the harbor (point 1 and 2 in Figure 4.4) is much smaller than the flow outside the harbor (points 3 and 4 in Figure 4.4), as the non-slip coastal boundary conditions and frictional force suppress the flow more inside the Narrowss considering the shallower depth there. In Figure 4.5, at grid points inside the channel, point 1 and 2, it is clear the along channel velocity of the two layers has opposite phase. And at points at the mouth of the channel and outside the channel, point 3 and 4, the along channel velocity of the two layers has the same phase, the shape of the two time series lines almost being superposed. The reason of this is to keep the mass constant in the harbor, the flow of the lower layer in the channel has to make up the effect of the flow in the upper layer, which means the direction of the current of the two layers tends to be opposite. The amplitude of the flow also proves this. As the lower layer is about twice thick as the upper layer in the channel (points

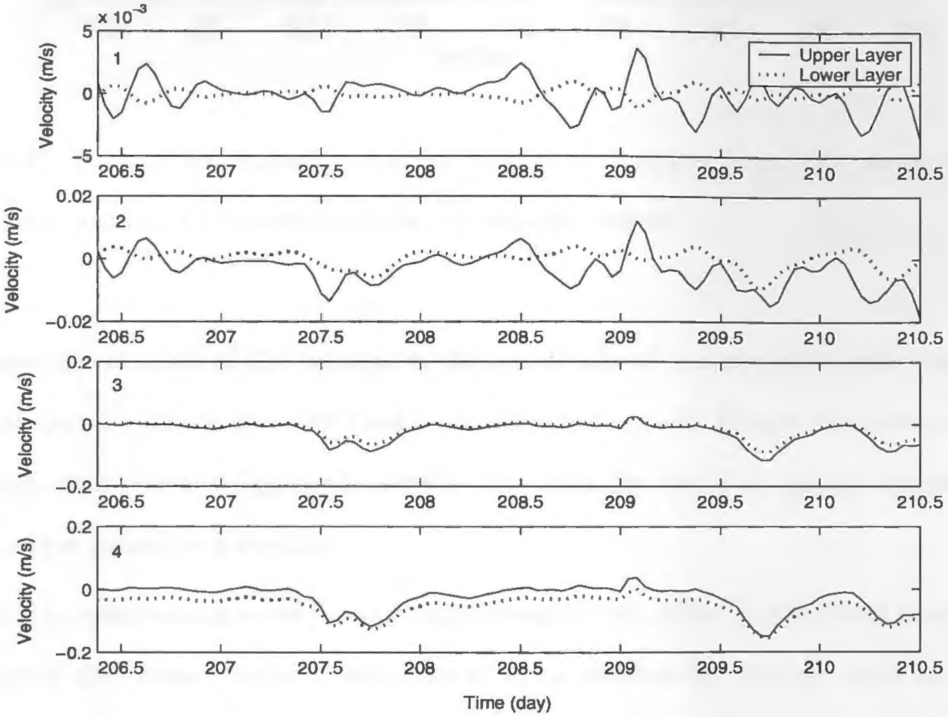

Figure 4.5: Time series of u (along channel velocity) at grid points 1-4 of Figure 4.4 following the sudden application at t=0 of a uniform wind. (+) denotes outflow, (-) denotes inflow.

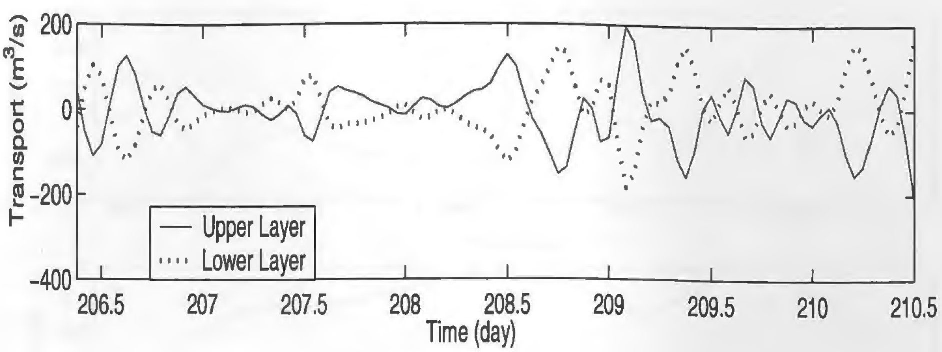

Figure 4.6: Time series of along channel transport in upper layer and lower layer of wind driven model.(+) denotes outflow, (-) denotes inflow.

2), to keep the balance of the transport, the amplitude of the along channel velocity in the upper layer is about twice of that in the upper layer. In Figure 4.6, time series of the transport in the two layers also testify this with the two lines mostly symmetrical to each other from the zero-line.

As the model domain is very small, only about 3.5×1.8 km, so it is hard to simulate the effect of the surface wind driven coastal waves outside the harbor, such as surface Kelvin waves along the west coast of the Island. The reason is the surface wave speed is 22 m/s (for bottom depth of 50 m) and this value gives only 80 seconds for the surface set up time which is too short compared with the observation result. But for internal waves, with a speed of only 0.07 m/s (for $g' = 1 \times 10^{-4} m/s^2$), the interface set up time can be 6 hours which is comparable to the observation result. Therefore, the influence from outside the harbor can be seen by comparing the model velocity in the lower layer at points inside and outside the harbor. In Figure 4.7, as expected, velocity along the coast in the lower layer outside the harbor matches the along channel velocity in the lower layer in the Narrows well and the coherence square between the two variables

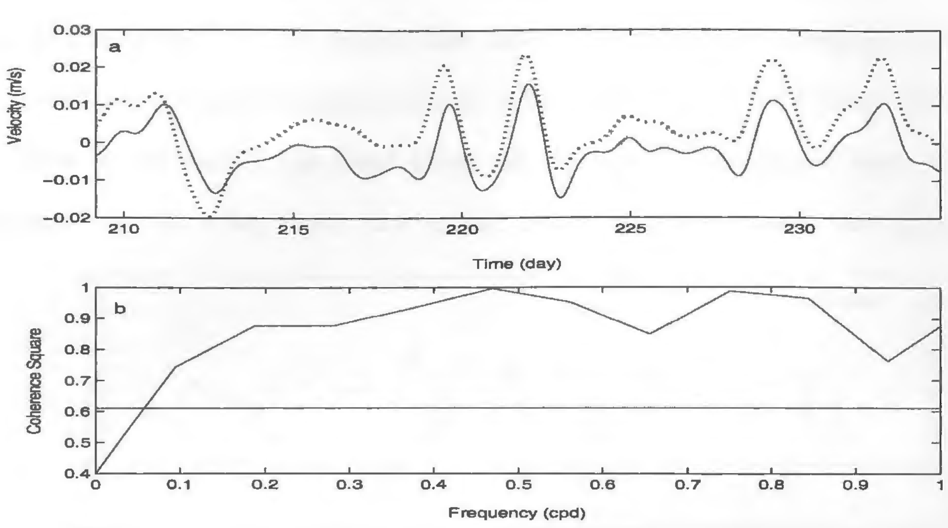

Figure 4.7: Time series of W-E velocity in lower layer of point 4 and S-N velocity in lower layer of point 2 (Figure 4.4). (+) denotes outflow, (-) denotes inflow.

keeps above 0.8 in most frequency scales.

4.3.2 Comparison Between Model Result and Observation Data

To compare the model results with the observation data, the model was run for about 25 days. The same filter, mentioned in chapter 3.2.2, is applied to the model result. Figure 4.8 shows time series of the transport of observation data and the result of model. The transport of the model is calculated from the flow through section PM in Figure 4.4, which is very close to the positions of the moorings inside the Narrows. The reason to choose section PM is to make the conditions of the two data sets as closer as possible. In the upper layer, the model result matches the observation well, except that the observation data is about 8 hours lag from the model result. The reason of this time delay is due to that the upper layer observation transport is calculated only from 5 m depth to 3 m depth without surface flow data, which means the response of the flow in this layer to the wind is slower, usually with a time lag of 6-12 hours (Matsuura, 1997), while in the model the wind effect on the flow in the upper layer is almost synchronous. In the lower layer, the model result does not match the observations well. The model apparently underestimated the transport in the lower layer compared with the observation result. The reason is the flow in the lower layer is not only driven by the wind stress but also influence by other forces, such as bottom water intrusion from outside the harbor (chapter 3.2.2).

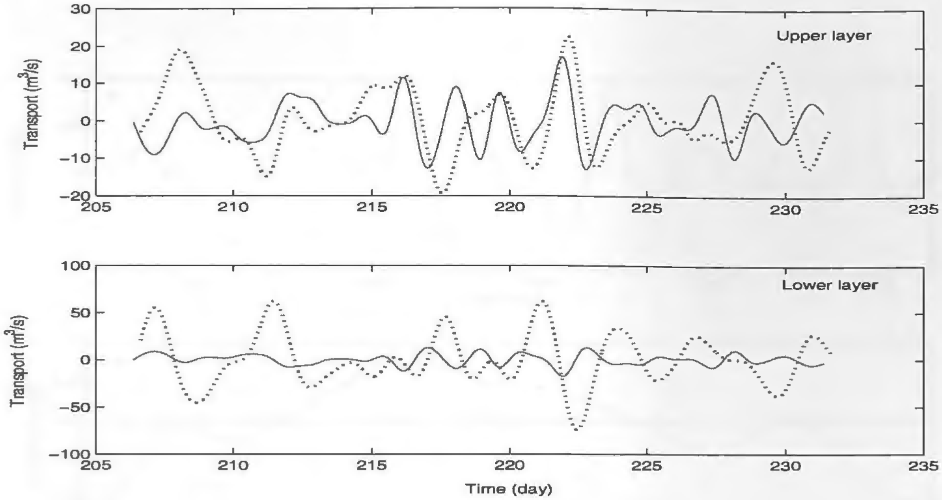

Figure 4.8: Time series of along channel transport in upper layer and lower layer of wind driven model and observation data. (+) denotes outflow, (-) denotes inflow.

As presented in chapter 3.2.2, EOF mode 1 of the observation data represents the wind driven flow in the channel. Therefore, another method to compare results of the model with observations is to apply EOF analysis to the model result also. To compute the EOF of model result, model grid points on section line PM (Figure 4.4) is picker out, then EOF is calculated from the time series of velocity at these points. EOF

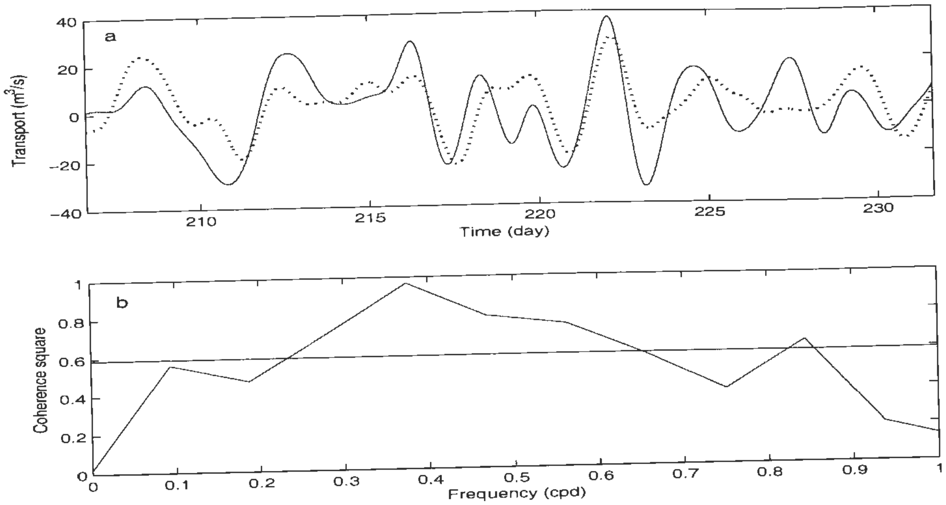

Figure 4.9: a) Time series of EOF mode 1 of along channel transport in upper layer from observation data and the transport in the upper layer computed by the model (solid line). b) Coherence square between along channel transport in the upper layer from observation and that computed by the model. (+) denotes outflow, (-) denotes inflow. The straight line denotes 95% confidence limit.

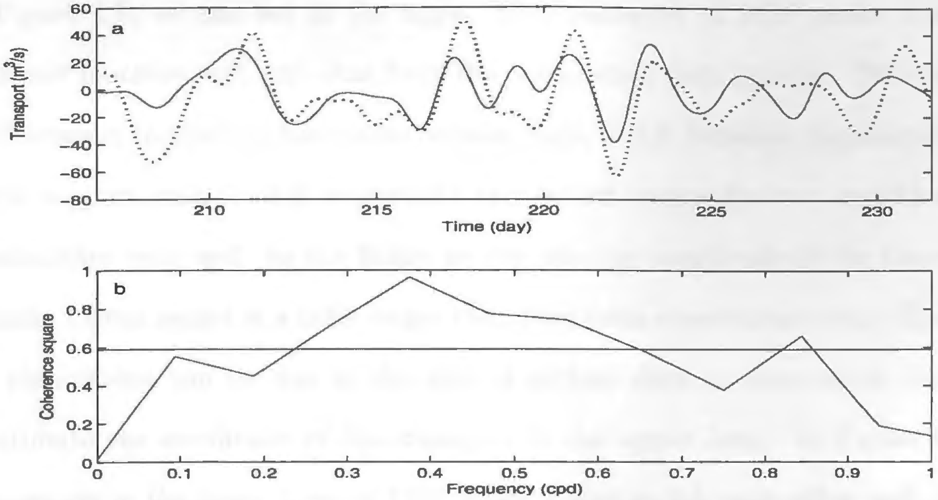

Figure 4.10: a) Time series of EOF mode 1 of along channel transport in lower layer from observation data and the transport in lower layer computed by the model (solid line). b) Coherence square between along channel transport in lower layer from observation and that computed by the model. (+) denotes outflow, (-) denotes inflow. The straight line denotes 95% confidence limit.

analysis of model result shows that more than 90% of the total variance contributes to mode 1. By multiplying the eigenvector with pincipal components, the estimated velocity of EOF mode 1 at model grid points can be obtained. Figures 4.9 and 4.10 present time series of EOF mode 1 of along channel transport in the two individual layers calculated from observation data and model result.

In Figure 4.9, we can see in the upper layer transport of EOF mode 1 from the model result matches well with that from the observation data (plot a). The coherence squared between the two variables also remains high, > 0.6, between frequency $0.3 - 0.6$ cpd, with a great peak (> 0.9) around 0.4 cpd, which means the two variables cohere with each other very well. In the figure we can also see amplitude of the transport of EOF mode 1 from model is a little larger than that from observation data. The reason of this phenomena can be due to the lack of surface data in observation which will underestimate the amplitude of the transport in the upper layer. In Figure 4.10 the two transports in the lower layer of EOF mode 1 also match each other well, and the coherence square shows that the two variables greatly cohere with each other between frequency $0.4 - 0.6$ cpd. Therefore, combining Figure 4.9 and 4.10, EOF mode 1 of the model result explains the wind driven flow in the Narrows well.

The observation velocity at moorings outside the harbor is also compared with model results. As the velocity scale of model result outside the harbor (point 4 in Figure 4.4) is much smaller than that of the observation data at mooring H2, in order to show the comparison clear, we multiplied the model velocity with a constant value to zoom in its scale. In Figure 4.11, the time series of S-N current velocity at 20 m depth of H2 matches well with the model velocity at point 4, and coherence square keeps high, > 0.7, when frequency is below 0.5 cpd. Therefore, the model simulates the trend of the flow outside the harbor well although its scale does not match the

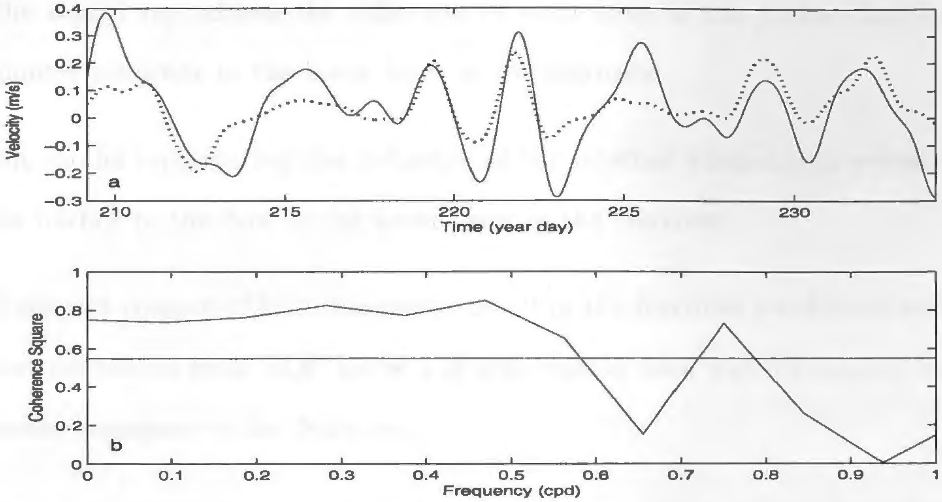

Figure 4.11: a) Time series of current velocity in S-N direction at 20 m depth of mooring H2 (solid line) and model velocity ×5 in S-N direction at point 4 (Figure 4.4). b) Coherence square between the two variables in the above plot. The straight line denotes 95% confidence limit.

observation result, with a 10 order difference.

4.3.3 Summary

From the result of the model and the comparison between model result and observation result, we can get the conclusions:

- The model reproduces the influence of wind force in the surface layer and the counter influence in the lower layer in the Narrows.
- The model reproducing the influence of the internal wind-driven waves out side the harbor to the flow in the lower layer in the Narrows.
- Transport computed from the model result in the Narrows is coherent with transport calculated from EOF mode 1 of observation data which indicates the wind-driven transport in the Narrows.
- Comparison between modeled velocity and observation velocity outside the harbor showing the trend of the two variables matching each other well although the scale of them has a order difference.

Chapter 5

Summary and Conclusions

The goal of this research is to clarify the circulation and its regulating force in the Narrows of the St. John's harbor. This thesis was begun with the analysis of the current observations from the summer and fall of 1999 and 2000. Harmonic tidal analysis and EOF were used to analyze the observation data. Then a two-layer numberical model driven by wind stress was used to study the forces influencing the flow in the Narrows and the model result was compared with the observation result.

Observations in both years shows the current in the Narrows has a two-layer vertical structure during most of the time with the upper layer above 5 m depth which is apparently influenced by strong wind in this area. A strong bottom outflow was found in the center of the Narrows during August in both years. This bottom flow has a seasonal feature in both years, keeping strongest in August, declining in September, and vanished in November.

Tidal analysis result of the observation data shows that the semi-diurnal tidal components, M2 and S2, dominates the tidal current in the Narrows, and also due to these strong, semi-diurnal tides the shallow water tidal current, Msf, is pretty large here. The phase plane plot and the vertical distribution of mean in-flow and out-flow velocity of different tidal components show a barolinic feature of the tides in the Narrows, with velocity amplitude peak occuring in the center of the upper layer (about 5 m depth) and lower layer (about 12 m depth).

Power spectral density of the observation data shows that the most energetic section focus on the low frequency (< 0.5 cpd), which indicates the subtidal signal dominating the current in the Narrows. Comparison between the subtidal current and wind speed shows that wind stress dominates surface current and has counter effect on the current in the lower layer.

EOF analysis was applied to the subtidal current. The result shows that mode 1 contributes more than 40% of the total variance, and mode 2 contributes about 27% of the total variance. The high coherence squared between wind stress and EOF mode 1 indicates mode 1 representing the wind driven motions in the Narrows. EOF mode 2 is compared with the obsrevation data outside the harbor. The result shows EOF mode 2 highly coheres with the observation current at 20 m depth of H2 mooring. Comparison between observation current at H2 and wind stress shows the they are highly correlated. Therefore, we can concluded that EOF mode 2 respresents the influence of external current that is driven by the wind stress outside the harbor.

A two-layer ocean model is used to reproduce the influence of wind stress on the current in the Narrows. The model result also shows that current of the lower layer in the Narrows is highly cohered with the flow in the lower layer outside the harbor. Transport calculated from the model result in the Narrows coheres well with transport calculated from EOF mode 1 of the observation data. Comparison between model velocity and observation velocity outside the harbor showing the trend of the two variables matching each other well although the magnitude of the them has an order difference.

Bibliography

[1] Allen, S.E., Topographically generated subnertial flows within a finite length canyon, *J. Phys. Oceanogr.*, 1996, 26, 1646-1654.

[2] Bretschneider, D.E., G. A. Cannon, et al., Variability of subtidal current structure in a fjord estuary: Puget Sound, Washington, *J. Geophys. Res.*, 1985, 90, 11949-11958.

[3] Bubino M., Hessner K., Decay of Stable Warm-Core Eddies in a Layered Frontal Model, *J. Phys. Oceanogr.*, 2002, 32, 188-201.

[4] Buttkus B., *Spectral Analysis and Filter Theory in Applied Geophysics*, 2000, 667pp.

[5] Carmack, E., and Y. Kulikov, Wind-forced upwelling and internal Kelvin waves in Mackenzie Canyon, Beaufort Sea, *J. Geophys. Res.*, 1998, 103, 18,447-18,458.

[6] Chen, X., and S.E. Allen, Influence of Canyons on shelf currents - a theoretical study, *J. Geophys. Res.*, 1996, 101, 18,043-18,059.

[7] Clarke, A.J., Observational and numerical evidence for wind-forced coastal trapped long wave, *J. Geophys. Res.*, 1977, 7, 231-247.

[8] Crawford, W.R., J.Y. Cherniawsky, P.F. Cummins, and M.G.G. Foreman, Variability of tidal currents in wide strait: A comparison between drifter observations and numerical simulations, *J. Geophys. Res.*, 1998, 103, 12,743-12,759.

[9] Crawford, W.R., M.J. Woodward., M.G.G. Foreman, and R.E. Thomson, Oceanographic features of Hecate Strait and Queen Charlotte Sound in summer, *Atmos.-Ocean.*, 1995, 33, 639-681. Csandady, G.T., Wind-induced barotropic motion in long lakes, *J. Phys. Oceanogr.*, 1973, 3, 429-438.

[10] de Young B., The Circulation and Internal Tide of Indian Arm, B.C., *Ph.D. Thesis*, 1986, 175 pp.

[11] de Young B. and S. Pond, The Deepwater Exchange Cycle in Indian Arm, British Columbia, *Estuarine, Coastal and Shelf Science*, 1988, 26, 285-308.

[12] de Young B., and Pond, S., A Partition of the Energy Loss from the Barotropic Tide in Fjords. *J. Phys. Oceanogr.*, 1989, 19, 246-252.

[13] de Young B., D. J. Schillinger, L. Zedel and J. Foley, Circulation Through the Narrows of St. John's Harbor: Summer and Fall 1999, *Physics and Physical Oceanography Technical Report 2000-1*, 2000, 54 pp.

[14] de Young B., D. J. Schillinger and J. Foley, Circulation Through the Narrows of St. John's Harbor: Summer 2000, *Physics and Physical Oceanography Technical Report 2000-2*, 2000, 61 pp.

[15] Dyer, K.R., *Estuaries: A Physical Introduction*, John Wiley, Chichester, 1973.

[16] Emery,W.J. and R.E. Thomson, *Data analysis method in physical oceanography*, 1 ed, Elsevier Science Ltd, 1997.

[17] Foreman, M.G.G., Manual for Tidal Heights Analysis and Prediction, *Pacific Marine Science Report 78-6*, Institute of Ocean Sciences, Patricia Bay, Victoria B.C., 1977.

[18] Foreman, M.G.G., R.A. Walters, R.F. Henry, C.P. Keller, and A.G. Dolling, A tidal model for eastern Juan de Fuca Strait and the southen Strait of Georgia., *J. Geophys. Res.*, 1995, 100, 721-740.

[19] Friedrichs, C.T., and J.M. Hamrick, Effects of channel geometry on cross sectional variations in along channel velocity in partially stratified estuaries, *Buoyancy Effects on Coastal and Estuarine Dynamics, Coastal and Estuarine Studies*, 53, 283-300.

[20] Geyer, W.R. and G.A.Cannon, Sill processes related to deep water renewal in a fjord, *J. Geophys. Res.*, 1982, 87, 7985-7996.

[21] Geyer, W.R., J.H. Trowbridge and M.M. Bowen, The Dynamics of a Partially Mixed Estuary, *J. Phys. Oceanogr.*, 2000, 30, 2035-2048.

[22] Gill, A.E., and E.H., Schumann, The generation of long shelf waves by the wind, *J. Phys. Oceanogr.*, 1974, 4,83-90.

[23] Glorioso, P.D., and A.M. Davies, The influence of eddy viscosity formulation, bottom topography, and wind wave effects upon the circulation of a shallow bay, *J. Phys. Oceanogr.*, 1995, 25, 1243-1264.

[24] Greatbatch, R.J. and T. Otterson, On the Formulation of Open Boundary Conditions at the Mouth of a Bay, *J. Geophys. Res.*, 1991, 96, 18,431-18,445.

[25] Hearn, C. J., J.R. Hunter, and M.L. Heron, The effects of a deep channel on the wind-induced flushing of a shallow bay or harbor, *J. Geophys. Res.*, 1987, 92, 3913-3924.

[26] Hunter, J. R., and C.J. Hearn, Lateral and vertical variations in the wind-driven circulation in long, shallow lakes, *J. Geophys. Res.*, 1987, 92, 13,106-13,114.

[27] Ianniello,J.P., Tidally induced residual currents in estuaries of constant breadth and depth, *J. Marine Res.*, 1979, 35, 755-785.

[28] Inall M., Cottier F., et al., Sill dynamics and energy transformation in a jet fjord, *Ocean Dynamics*, 2004, 54, 307-314.

[29] Janzen, C.D., Forcing of Subtidal Currents and Salinity in a Coastal Lagoon, M.S. thesis, 1996, 127 pp., Univ. of Del. Newark.

[30] K. Pearson, On limes and playes of closest fit to systems of points in space. *Phil. Mag.*, 1902, 2:559-572.

[31] Kjerfve, B., and B.A. Knoppers, Tidal Choking in a Coastal Lagoon, in *Tidal Hydrodynamics*, Edited by B. Parker, 1991, pp. 169-181, John Wiley, New York.

[32] Kjerfve, B., J. E. Greer, and R.L. Crout, Low-frequency Response of Estuarine Sea Level to Non-local Forcing, in *Estuarine Interactions*, edited by M. L. Wiley, pp 497-513, Academic, San Diego, Calif, 1978.

[33] Lorenz, E.N., Empirical orthogonal functions and statistical weather prediction. *Sci. Rep. No. 1, Statistical Forecasting Project*, 1956, M.I.T., Cambridge, MA, 48 pp.

[34] Masson, D., A case study of wave-current interaction in a strong tidal current, *J. Phys. Oceanogr.*, 1996, 26, 359-372.

[35] Matsuura, H., An Application of a Two-layer Model to Wind Driven Sub-Tidal Currents in Puget Sound, *Journal of Oceanography*, 1995, 51, 571-584.

[36] Matsuura, H. and G. A. Cannon, Wind Effects on Sub-tidal Currents in Puget Sound, *Journal of Oceanography*, 1997, 53, 53-66.

[37] Middleton, J.F., and D.G., Wright, Coastal-trapped waves on the Labrador shelf, *J. Geophys. Res.*, 1991, 2,599-609.

[38] Middleton, J.F., and F. Viera, The forcing of low frequency motions within Bass Strait, *J. Phys. Oceanogr.*, 1991, 21,695-708.

[39] Miller, M.J., and A. J. Thorpe, Raidation Conditions For the Lateral Boundaries of Limited-are Numberical Models, *Q. J. R. Meteorol. Soc.*, 1981, 107, 615-628.

[40] Neumann G., Pierson W.J., *Principles of Physical Oceanography*, 1966, 545 pp.

[41] Nobel, M., and B. Butman, Low-frequency, Wind-induced Sea Level Oscillations Along The East Coast of North America, *J. Geophys. Res.*, 1979, 84, 3227-3236.

[42] O'Brien, J.J. and H.E. Hurlburt, A Numerical Model of Coastal Upwelling, *J. Phys. Oceanogr.*, 1972, 2, 14-26.

[43] Ott, M., and C. Garrett, Frictional estuarine circulation in Juan de Fuca Strait, with implications for secondary circulation, *J. Geophys. Res.*, 1998,

[44] Pawlowicz, R., B. Beardsley, and S. Lentz, Classical tidal harmonic analysis including error estimates in MATLAB using T-TIDE, *Computers and Geosciences*, 2002, V28, 929-937.

[45] Peixoto, J.P. and A.H. Oort, Physics of Climate, 1991, Americal Institute of Physics, 520 pp.

[46] Robina, A. and K. Hessener, Decay of Stable Warm-Core Eddies in a Layered Frontal Model, *J. Phys. Oceanogr.*, 2002, 32, 188-201.

[47] Schroeder, W. W., and W. J. Wiseman, Low-frequency Shelf-estuarine Exchange Process in Mobile Bay and Other Estuarine Systems on The Norther Gulf of Mexico, in *Estuarine Variability*, edited by D. A. Wolfe, 1986, pp. 355-367, Academic, San Diego, Clif.

[48] Signell, R.P., R.C. Beardsley, H.C. Grabor, and A. Capotondi, Effect of wave-current interaction on wind-driven circulation in narrow, shallow embayments, *J. Geophys. Res.*, 1990, 95, 9671-9678.

[49] Smith, N. P., Meteorological and Tidal Exchange Between Corpus Christi Bay, Texas, and the Northwestern Gulf of Mexico, *Estuarine Coastal Mar. Sci.*, 1977, 5, 511-520.

[50] Stacey, M.W., s. Pond and Z.P. Nowak, A numerical model of the circulation in Knight Inlet, British Columbia, Canada, *J. Phys. Oceanogr.*, 1995, 25, 1037-1062.

[51] Stigebrandt A, Evidence for baroclinic wave drag in fjords. In: Muller P, Henderson D(eds) Dynamics of oceanic internal gravity waves II. SOEST Special Production 1999, pp 73-82.

[52] Svenden, H. and R.O.R.U. Thompson, Wind-driven circulation in a fjord, *J. Phys. Oceanogr.*, 1978, 14, 904-921.

[53] Thompson, K.R. and J. Sheng, Subtidal circulation on the Scotian Shelf: Assessing the hindcast skill of a linear, barotropic model, *J. Geophys. Res.*, 1997, 102, 24,987-25,004.

[54] Thompson, R.O.R.Y., Low-pass filters to suppress inertial and tidal frequencies, *J. Phys. Oceanogr.*, 1983, 13,1077-1083.

[55] Valle-Levinson,A. and L. Atkinson, Spatial gradients in the flow over an estuarine channel, *Estuaries*, 1999, 22(2A), 179-193.

[56] Valle-Levinson,A., K. Wong, and K. Bosley, Observations of the wind-induced exchange at the entrance to Chesapeake Bay, *J. Mar. Res.*, 2001a, 59(3), 391-416.

[57] Valle-Levison, A., L.P. Atkinson, D. Figueroa, and L.Castro, Flow induced by upwelling winds in an equatorward facing bay: Gulf of Arauco, Chile, *J. Geophys. Res.*, 2003b, 108(C2), 3054.

[58] Walter, R. a., Low-frequency Variations in Sea Level and Currents In South San Francisco Bay, *J. Phys. Oceanogr.*, 1982, 12, 658-668.

[59] Walters, R.A., and J. W. Gartner, Subtidal Sea Level and Current Variations in The Northern Reach of San Francisco Bay, *Estuarine Coastal Shelf Sci.*, 1985, 21, 17-32.

[60] Wang, D.-P, and A. J. Elliott, Non-tidal Variability in The Chesapeake Bay and Potomac River: Evidence for Non-local Forcing, *J. Phys. Oceanogr.*, 1978, 8, 225-232.

[61] Wang, D.-P., Low Frequency Variability on the Middle Atlantic Bight, *J. Mar. Res.*, 1979, 37, 683-697.

[62] Wang, D.-P., Subtidal Sea Level Variations in The Chesapeake Bay and Relations to Atmospheric Forcing, *J. Phys. Oceanogr.*, 1979a, 9, 413-421.

[63] Weisberg, R. H., The Nontidal Flow in The Providence River of Narragansett Bay: A Stochastic Approach to Estuarine Circulation, *J. Phys. Oceanogr.*, 1976, 6, 721-734.

[64] Weisberg, R. H., and W. Sturges, Velocity Observations in The West Passage of Narragansett Bay: A Partially Mixed Estuary, *J. Phys. Oceanogr.*, 1976, 6, 345-354.

[65] Wiseman, W. J., W. W. Schroeder, and S. P. Dinnel, Shelf-estuarine Water Exchanges Between the Gulf of Mexico and Mobile Bay, Alabama, *Am. Fish. Soc. Symp.*, 1988, 3, 1-8.

[66] Wong, K.-C., and J. DiLorenzo, The Response of Delaware's Inland Bays to Ocean Forcing, *J. Geophys. Res.*, 1988, 93, 12,525-12,535.

[67] Wong, K.-C., and R. E. Wilson, Observations of Low-frequency Variability in Great South Bay and relations to Atmospheric Forcing, *J. Phys. Oceanogr.*, 1984, 14, 1893-1900.

[68] Wong, K.-C., and R. W. Garvine, Observations of Wind-induced Subtidal Variability in The Delaware Estuary, *J. Geophys. Res.*, 1984, 89, 10,589-10,597.

[69] Wong, K-G. and J. E. Moses-Hall, On the relative importance of the remote and local wind effects to the subtidal variability in a coastal plain estuary, *J. Geophys. Res.*, 1998, 103, 18,393-18,404.

[70] Wright, D.G., D.A. Greenberg, and F.G. Majaess, The influence of bays on adjusted sea level over adjacent shelves with application to the Labrador shelf, *J. Geophys. Res.*, 1987, 92(C13), 14,610-620.

Appendix A

Table A.1: Summary Statistics of ADCP current velocity in July/August, 1999

Depth(m)	Component	Max(cm/s)	Min(cm/s)	Mean(cm/s)	Std(cm/s)
1	v	11.76	0.01	-0.81	2.39
	u	35.21	0.00	3.34	9.15
2	v	9.31	0.00	-0.69	1.87
	u	32.94	0.00	1.53	9.01
3	v	6.87	0.01	-0.83	1.80
	u	33.10	0.00	-1.11	8.505
4	v	8.13	0.00	-1.06	1.74
	u	31.69	0.03	-3.11	7.65
5	v	7.80	0.01	-1.23	1.55
	u	35.01	0.01	-4.48	7.04
6	v	7.13	0.01	-1.41	1.55
	u	34.93	0.01	-5.06	6.86
8	v	8.11	0.00	-1.41	1.64
	u	37.35	0.00	-4.27	7.58
9	v	7.84	0.00	-1.48	1.59
	u	40.37	0.02	-2.82	8.56
10	v	6.97	0.00	-1.63	1.58
	u	41.86	0.01	-1.03	9.58
12	v	8.15	0.01	-1.96	1.75
	u	41.55	0.02	2.74	11.02
14	v	10.00	0.00	-1.76	1.96
	u	37.54	0.02	5.69	11.55

Table A.2: Summary Statistics of ADCP current velocity in October/November, 1999

Depth(m)	Component	Max(cm/s)	Min(cm/s)	Mean(cm/s)	Std(cm/s)
3	v	17.74	0.00	-0.11	1.93
	u	30.91	0.02	4.42	5.93
4	v	19.34	0.01	-0.15	1.93
	u	27.26	0.00	1.93	5.73
6	v	22.03	0.00	-0.73	2.29
	u	21.39	0.01	-2.28	4.71
8	v	23.50	0.00	-1.62	2.06
	u	21.50	0.01	-5.41	4.90
9	v	22.42	0.01	-1.77	2.16
	u	24.33	0.01	-6.08	5.52
10	v	23.57	0.00	-1.94	2.18
	u	27.00	0.00	-6.43	6.01
11	v	24.27	0.00	-1.91	2.18
	u	28.42	0.03	-6.42	6.43
12	v	22.90	0.00	-1.80	2.18
	u	28.41	0.11	-6.37	6.68
14	v	21.74	0.00	-1.30	1.94
	u	26.32	0.03	-5.71	6.92

Table A.3: Summary Statistics of ADCP current velocity at N2 in 2000

Depth(m)	Component	Mean(cm/s)	Std(cm/s)	Max(cm/s)
3	u	1.79	5.08	18.07
	v	0.44	2.60	13.04
4	u	-0.29	4.05	16.60
	v	0.29	2.41	13.88
6	u	-1.75	2.98	15.59
	v	0.83	1.98	10.40
8	u	-1.61	2.36	11.35
	v	0.91	1.68	7.92
9	u	-1.51	2.27	9.06
	v	0.68	1.51	6.29
10	u	-1.30	2.24	9.21
	v	0.57	1.46	6.64
11	u	-0.98	2.17	8.36
	v	0.54	1.72	7.33
12	u	-0.72	2.14	9.47
	v	0.38	1.37	5.55
14	u	-0.26	2.24	7.81
	v	0.52	1.82	8.43
16	u	0.03	2.28	8.25
	v	-0.01	1.31	6.53
18	u	0.25	3.02	11.79
	v	-0.85	2.00	10.72

Table A.4: Summary Statistics of ADCP current velocity at N3 in 2000

Depth(m)	Component	Mean(cm/s)	Std(cm/s)	Max(cm/s)
4	u	-0.98	5.08	27.01
	v	0.72	2.83	18.20
6	u	-3.38	3.83	13.80
	v	1.12	2.29	10.95
8	u	-4.53	3.55	16.64
	v	1.08	2.30	10.47
9	u	-4.60	3.50	17.79
	v	0.96	2.20	11.03
10	u	-4.21	3.53	17.67
	v	0.79	2.04	9.71
12	u	-2.89	3.50	13.16
	v	0.21	1.82	9.10
14	u	-1.30	4.05	15.75
	v	-0.34	1.91	9.67
15	u	-0.48	4.28	18.17
	v	-0.55	2.08	10.15
17	u	1.08	4.55	18.59
	v	-1.01	2.46	10.77
18	u	1.60	4.60	22.49
	v	-1.08	2.64	11.22
20	u	2.06	4.56	18.42
	v	-1.37	2.96	11.35

Table A.5: Summary Statistics of ADCP current velocity at N4 in 2000

Depth(m)	Component	Mean(cm/s)	Std(cm/s)	Max(cm/s)
3	u	-0.47	3.60	15.00
	v	0.33	1.91	9.67
4	u	-1.79	3.47	15.00
	v	0.56	1.85	8.91
5	u	-2.53	3.48	18.30
	v	0.58	1.79	8.48
6	u	-2.93	3.46	15.00
	v	0.61	1.83	7.96
7	u	-3.05	3.43	16.10
	v	0.56	1.76	8.35
8	u	-2.85	3.26	13.50
	v	0.48	1.73	7.84
9	u	-2.55	3.11	12.60
	v	0.29	1.78	8.43
10	u	-2.10	2.87	12.20
	v	-0.02	1.80	7.03
11	u	-1.71	2.55	10.00
	v	-0.27	1.81	7.63